Long Range Surface Plasmon Waveguides for Electrochemical Detection

by

Zohreh Hirbodvash

A thesis submitted
in partial fulfillment of the requirements for the degree
of Doctor of Philosophy in Physics

Department of Physics
Faculty of Science
University of Ottawa

Abstract

An electrochemical detection method based on long range surface plasmon waveguides is proposed and demonstrated in this integrated article thesis. This dissertation uses CYTOP gold (Au) waveguides supporting long range surface plasmon polaritons (LRSPPs) in conjunction with grating couplers as well as Au waveguides embedded on a one-dimensional photonic crystal (1DPC) supporting Bloch LRSPPs integrated grating couplers.

Grating couplers for Au stripe waveguides embedded in Cytop are demonstrated and analyzed. Grating couplers are used in a broadside coupling scheme where a laser beam incident on a stripe of Au on Cytop. The use of gratings for excitation of LRSPPs simplifies optical alignment and does not require high-quality input and output edge facets. Over a broad operating wavelength range, optical experiments are performed to demonstrate coupling loss and determine the efficiency of grating coupling using both a cleaved bow-tie PM fiber and a lensed PM fiber. The coupling loss and grating coupling efficiency of both types of fibers are also calculated numerically.

Fluoropolymers with refractive indices close to water, such as CYTOP, are widely used to make waveguide biosensors today. Due to its low glass transition temperature, CYTOP presents limitations to fabrication processes. A truncated 1D photonic crystal may replace a low-index polymer cladding such as CYTOP to support Bloch LRSPPs within the bandgap of the 1DPC over limited wavenumbers and wavelength range.

As a result of the high sensitivity of Au stripe Bloch LRSPP waveguide biosensors and their compatibility with high levels of integration, microelectrode systems that can be

integrated with such optical biosensors are examined. A chip bearing a Au LRSPP waveguide that can also function as a working electrode (WE), a Pt counter electrode (CE), and Pt/Cu electrical contact pads, is used to demonstrate the electrochemical performance of LRSPPs waveguides. The cyclic voltammetry measurements were performed at different scan rates and concentrations of potassium ferricyanide as the redox species on Au LRSPPs waveguides. By fitting our experimental data to the Randles-Sevcik equation, we find the diffusion coefficient of potassium ferricyanide. The results from CV measurements obtained from chips are compared with commercial macroscopic electrodes. The CV measurements are also compared with theoretical results computed using the Butler-Volmer equation to determine the rate constant of the redox species at zero potential.

A waveguide containing a stripe of Au that propagates infrared surface plasmon polaritons (SPPs), acting simultaneously as an electrode in a three-electrode electrochemical cell is also examined. Under SPP excitation, cyclic voltammetry was measured as a function of incident optical power and wavelength (1350 nm). In oxidation and reduction reactions, energetic electrons are separated from energetic holes. Under SPP excitation, redox current densities increase by 10×. With the SPP power, the oxidation, reduction, and equilibrium potentials drop by as much as 2× and separate in correlation with the photon energy. According to electrochemical impedance spectroscopy, charge transfer resistance dropped by almost 2× under SPP excitation. During SPP excitation, the temperature of the working electrode is monitored in situ and independent control experiments are performed to isolate thermal effects. Measurements of chronoamperometry with SPPs modulated at 600 Hz yield a rapid current response modulated at the same frequency, ruling out thermally

enhanced mass transport. The observation is attributed to the opening of optically controlled non-equilibrium redox channels associated with the energetic carrier transfer to the redox species. During CV and chronoamperometry measurements, convolutional voltammetry is performed by monitoring the SPP output power versus the applied voltage. Using both experimental and theoretical methods, we demonstrate that the SPP output power is proportional to the electrochemical current convolution. A SPP voltammogram confirms that signal changes are mainly caused by differences in refractive index between reduced and oxidized forms of redox species. In addition, we demonstrate that energetic carriers resulted from SPP absorption significantly improved electrochemical sensitivity.

As a complementary electrochemical technique, convolutional voltammetry is useful since the signal is related directly to the concentration of electroactive species on the working electrode (WE) and independent of the scan rate. As a probe of electrochemistry taking place in waveguides, surface plasmon polaritons (SPPs) propagating along one are sensitive. In such a waveguide, the optical output power is proportional to the time convolution of the electrochemical current density, eliminating the need to calculate the latter a posteriori via numerical integration. It is demonstrated that a waveguide WE provide an optical response that can be experimentally validated by chronoamperometry and cyclic voltammetry measurements under SPP excitation for a few potassium ferricyanide (redox species) concentrations in potassium nitrate (electrolyte) and various scan rates. Cyclic voltammetry measurements taken under increasing SPP power produce a regime where SPPs no longer act solely as the probe, but also act as a pump, producing energetic electrons and holes via their absorption in the WE. The energetic carriers enhance

(10×) redox current densities as well as the convolution signal measured directly as the optical output power over time.

This dissertation is dedicated to my husband, Payman

for his endless love, support, and encouragement

Acknowledgements

Firstly, I would like to thank Prof. Pierre Berini for all the encouragement, guidance, and support he has given me. Being a member of his research team gave me invaluable experience, and I felt supported throughout my studies. It would not have been possible for me to progress in my research without his constructive comments, insightful feedback, and endless support.

I had the honor of working with Prof. Elena Baranova. I am thankful to her for her outstanding support and guidance. I really appreciate working with her and learned extensively from her.

I like to acknowledge the members and staff of the Center for Research in Photonics at the University of Ottawa for their continuous assistance and support during my study. Specifically, I like to express my sincere thanks to the lab managers from the Berini Group at the University of Ottawa: Ewa Lisicka-Skrzek, Anthony Olivieri, and Howard Northfield. I have always appreciated your patience and willingness to help without reservation.

I would especially like to acknowledge my friends and colleagues with whom I interacted the most at uOttawa: Alex Krupin, Maryam Khodami, Mohamed Seif Eddine Houache, Saba Siadat, Sabaa Rashid, Akram Hajebifard, Wei Ru Wong, Maryam Sadat Amiri Naeini, Emilie Laffont, Luis Mayoral Astorga, Jaspreet Walia, Maude Amyot-Bourgeois, Maryam Al-Shehab, Muhammad Asif, Shayan Saeidi, and Liam Kelly.

Last, and by no means least, I am endlessly grateful to my family: my beloved husband, Payman, for his countless sacrifices and support who stood by me through all my travail; my parents, Akram and Ebrahim, and my sister Fatemeh for their love, and encouragement.

Table of Contents

List of publications

Papers accepted and published in refereed journals (included in the thesis):

Z. Hirbodvash, M. Khodami, N. R. Fong, E. Lisicka-Skrzek, A. Olivieri, H. Northfield, R. N. Tait, P. Berini, "Grating couplers fabricated by e-beam lithography for long range surface plasmon waveguides embedded in a fluoropolymer" Applied Optics, 2994-3002 (58), 2019.

Z. Hirbodvash, M. S. E. Houache, O. Krupin, M. Khodami, H. Northfield, A. Olivieri, E. A. Baranova, P. Berini, "Electrochemical Performance of Lithographically-Defined Micro-Electrodes for Integration and Device Applications" Chemosensors, 277 (9), 2021.

Z. Hirbodvash, O. Krupin, H. Northfield, A. Olivieri, E. A. Baranova, P. Berini, "Infrared surface plasmons on a Au waveguide electrode open new redox channels associated with the transfer of energetic carriers" Science Advances, eabm9303 (8), 2022.

Z. Hirbodvash, E. A. Baranova, P. Berini, "Real-time convolutional voltammetry enhanced by energetic (hot) electrons and holes on a surface plasmon waveguide electrode" Analytical Chemistry, 13145–13152 (94), 2022.

Collaborative Papers accepted and published in refereed journals and conferences (not included in thesis):

Z. Hirbodvash, J. Walia, S. Rashid, G. Killaire, E.A. Baranova, A. Weck, P. Berini, "Plasmonic hot carrier and their applications", 2022 Photonics North (PN), 2022.

M. Asif, O. Krupin, W. R. Wong, **Z. Hirbodvash**, E. Lisicka-Skrzek, C. Hahn, R. N. Tait, P. Berini, “Wafer-bonded surface plasmon waveguide sensors with in-plane microfluidic interfaces”, Journal of Micromechanics and Microengineering, 095004 (30), 2020.

M. Khodami, **Z. Hirbodvash**, O. Krupin, P. Berini, “Bloch long range surface plasmons on waveguide arrays as multichannel biosensors”, SPIE Photonics West: Plasmonics in Biology and Medicine XVII, 58-64 (11257) , 2020.

M. Khodami, **Z. Hirbodvash**, O. Krupin, E. Lisicka-Skrzek, H. Northfield, A. Olivieri, P. Berini, “Fabrication of Bloch long range surface plasmons biosensors”, SPIE Photonics West: Integrated Optics: Devices, Materials, and Technologies XXIV 11283, 139-144 (11283), 2020.

M. Khodami, **Z. Hirbodvash**, O. Krupin, W. R. Wong, E. Lisicka-Skrzek, H. Northfield, C. Hahn, P. Berini, “Fabrication of Bloch Long Range Surface Plasmon Waveguides Integrating Counter Electrodes and Microfluidic Channels for Multimodal Biosensing” IEEE Journal of Microelectromechanical Systems, 686-695 (30), 2021.

List of Figures

List of Acronyms

ATR	Attenuated total reflection
AFM	Atomic force microscopy
Gly	Glycerol
IPA	Isopropanol Alcohol
IR	Infrared
LRSPP	Long range surface plasmon polariton
MPA	Mode power attenuation
MZI	Mach-Zender interferometers
PC	Photonics crystal
PMMA	Poly (methyl methacrylate)
PM	Polarization maintaining
SPP	Surface plasmon polariton
SPR	Surface plasmon resonance
SEM	Scanning electron microscopy
SMF	Single mode fiber
TE	Transverse electric
TM	Transverse magnetic
CV	Cyclic voltammetry

EC-SPR	Electrochemical surface plasmon resonance

Glossary

ω	Angular frequency
ω_p	Plasma frequency
γ	Collision frequency
τ	Relaxation time of the electrons
n_e	Electron density
e	Electron charge
m^*	Effective electronic mass
ε_0	Permittivity of free space
ε	Relative permittivity
ε_∞	Material specific polarization correction factor
c	Speed of light in free space
n	Refractive index
K_{spp}	Propagation constant of SPP
ω_{SP}	Surface plasma frequency
k	Propagation constants of the input light
n_{eff}	Average effective index of the LRSPP mode propagating along the waveguide
λ_0	Free-space operating wavelength
α	Attenuation constant

i_p	Peak oxidative current
D	Diffusion coefficient
R	Gas constant
T	Temperature
F	Faraday constant
C	Concentration of the redox species
E	Potential of an electrochemical cell
E°	Standard potential of a species
B	Sensitivity of the SPR angle to a change in the bulk index of refraction

Chapter 1.

Introduction

1.1 Biosensing and Biosensors

Analyzing biomolecules is required in many fields ranging from food safety inspection to medical diagnostics [1,2,3]. Many labelled detection methods have been used to detect biomolecules. These labeled detections techniques include enzyme-linked immunosorbent assay (ELISA) [4,5], colorimetric and fluorescence detection [6,7,8], polymerase chain reaction (PCR) [9,10], radioactive isotopes (radio-immunoassays) [11], vibrational spectroscopy (*e.g.*, infrared and Raman spectroscopy) [12] and some other techniques [13,14]. All these labelled techniques create liabilities due to the use of labels. An example of a liability created by labelling is interference of the fluorophore with binding kinetics, and changes in fluorescence dynamics depending on specific dye–protein interactions after being exposed to analytes [15]. Such liabilities can be eliminated by using label-free methods, as have been employed to detect biomolecules using mass spectrometry (MS) [16], quartz crystal microbalance (QCM) [17], surface plasmon resonance (SPR) [18], localized surface plasmon resonance (LSPR) [19], long-range surface plasmon polaritons (LRSPPs) [20], and anomalous reflection of gold [21].

A biosensor is a device that is used to measure biological or chemical reactions by generating signals (electrical, thermal, optical) proportional to the concentration of an analyte [2,22]. A biosensor has a recognition element (*e.g.*, enzymes, nucleic acids, cells, and micro-organisms or antibodies) to capture the analyte of interest in the sample selectively. In addition, a transducer converts the biorecognition event to a quantitative signal [23]. Depending on the underlying transducer technology, one can identify four different types of biosensors: electrochemical [24,25], piezoelectric [26,27], thermal [28], and optical [29,30].

The most common type of biosensor is electrochemical [30]. Electrodes have an essential role as solid support for the immobilization of biomolecules and electron transfer to/from the redox species. As the result of certain electroactive species undergoing a redox reaction in the system, a voltage or a current is generated. One of the critical aspects of the electrochemical biosensor is using enzymes as predominant recognition elements due to their specific binding capabilities and biocatalytic activity [31,32]. In this sensing method, different electrochemical detection techniques such as amperometric, potentiometric, and conductometric devices are used [33].

A piezoelectric sensor uses the piezoelectric effect to measure quantities of interest such as pressure, force, or acceleration. The Quartz Crystal Microbalance (QCM) is the most well-known type of piezoelectric sensor [34]. In this sensor, the resonant frequency of a quartz crystal is measured to deduce changes in the surface mass concentration. QCM is used in gaseous, vacuum and fluidic environments [35].

Thermometric biosensors use thermometry or measurement of temperature. The most known version of such a system is a thermometer [28]. The principle in thermometric devices is based on heat measurement using sensitive thermistors [36]. Thermometric biosensors use the fundamental property of biological reactions such as absorption or evolution of heat. They are also utilized as a part of enzyme-linked immunoassay (ELISA). This new method is known as thermometric ELISA (TELISA) [37,38].

Optical biosensors measure an optical quantity or attribute such as absorption, fluorescence, luminescence, reflectance, Raman scattering, or refractive index [39-41]. Optical biosensors can provide highly sensitive, direct, real-time, and label-free detection of many biological and chemical substances [42]. Optical biosensors operate in label-based or label-free mode [42]. In label-based sensors, a label is used, and then an optical signal is produced by a colorimetric, fluorescent, or luminescent method. In label-free devices, the detected signal is generated directly by the interaction of the analyzed material with the transducer [42]. There are different varieties of optical biosensors, such as optrode fibre optics, evanescent-wave waveguides, flow immunosensors, and surface plasmon resonance (SPR).

Surface plasmon polaritons (SPPs) are propagating modes at the interface between a metal and a dielectric medium, and biosensors based on SPPs are among the most studied and used devices because of the small mode area and large surface fields [43]. These features make them very sensitive to changes in the refractive index near the metallic surface. However, propagation losses associated with the absorption of light in the metal is a limitation, but this problem can be addressed using symmetric structures based on a thin metal layer to support long-range SPPs (LRSPPs). The existence of LRSPPs requires that both the upper and lower claddings have a similar refractive index. Sensing in an aqueous environment limits the choice of lower cladding materials, *e.g.*, to polymers such as Teflon or Cytop, which leads to limitations in the fabrication of devices, especially in terms of thermal excursions during processing. An alternative approach consists of using a one-dimensional photonic crystal (1DPC) [43]. A 1DPC can be used on one of the sides of a thin metal layer and they can mimic the optical properties of the medium on the other side over a limited wavelength range. The modes supported in such a structure are called Bloch LRSPPs.

LRSPP waveguides consisting of Au stripes can be integrated with input and output grating couplers. Grating couplers enable broadside (top) coupling with good efficiency and a low level of background light. The scheme simplifies optical alignments and does not require high-quality input and output edge facets. Chips bearing a Au LRSPP waveguide, along with a Pt electrode and Pt/Cu electrical contact pads, are used in this thesis. The gold LRSPP waveguides also operate as working electrodes, and the Pt stripes as counter electrodes. This chip structure provides a platform for the integration of optical (LRSPP) biosensors with electrochemical sensors. The high sensitivity of Au stripe LRSPP waveguide biosensors in addition to suitability for high levels of integration make them a good choice for multi-modal sensing strategies useful in disease detection. A combination of electrochemical probes with plasmonic structures is of interest to investigating light-induced hot-carrier electrochemical reactions. This thesis investigates LRSPPs and their role in electrochemical detection.

1.2 Thesis scope and outline

This thesis aims to demonstrate the characterization of optical and electrochemical biosensors based on Bloch LRSPPs. Gold waveguides both on CYTOP and a one-dimensional photonic crystal (1DPC) supporting Bloch LRSPPs are used in this dissertation. Each chapter is presented as a scientific article with an introductory section. The dissertation is organized as follows:

Chapter 2 presents a comprehensive review of Bloch long-range surface plasmon polaritons (LRSPPs) and plasmonic hot-carrier catalysis. First, the surface plasmon theory is explained, followed by a summary of surface plasmon resonance (SPR) and previous works in that area. A discussion about LRSPPs, Bloch waveguides, grating couplers, and microelectrodes is also provided in this chapter.

Chapter 3 reports fabrication and analysis of grating couplers for Au stripe waveguides embedded in Cytop. Grating couplers are used extensively throughout the thesis. Optical experiments are performed to illustrate coupling loss and determine the grating coupling efficiencies using a cleaved bow-tie PM fiber and a lensed PM fiber over a broad operating wavelength range. A numerical calculation is also made to find coupling loss and grating coupling efficiencies for both types of fibers.

Chapter 4 investigates lithographically-defined and evaporated Au and Pt microelectrodes on a 1DPC substrate for electrochemical detection applications. This study demonstrates the need to “burn-in” (current anneal) microelectrodes before electrochemical measurements. Cyclic voltammetry (CV) measurements at various scan rates and concentrations of potassium ferricyanide as the redox species are performed. The diffusion coefficient of potassium ferricyanide is obtained by fitting our experimental data to the Randles–Sevcik equation. The results from CV measurements obtained from chips are compared with commercial macroscopic electrodes. CV measurements are compared with theoretical results computed using the Butler-Volmer equation while extracting the rate constant at zero potential of our redox species.

Chapter 5 reports plasmonic catalysis in electrochemistry with surface plasmon waveguides and infrared light. It is shown in this study that redox current densities increase by 10× under plasmonic excitation. Oxidation, reduction, and equilibrium potentials also drop by as much as 2× beyond a clear threshold with optical power. Redox potentials drop beyond threshold with increasing photon energy, *i.e.*, exhibiting optical control of redox potentials.

Chapter 6 investigates the convolutional voltammetry. Convolutional voltammetry is performed by monitoring the SPP output power versus the applied voltage as cyclic voltammetry (CV) and chronoamperometry measurements are taken. Experimentally and theoretically, we demonstrate that the SPP output power is proportional to the convolution of the electrochemical current. It is confirmed by SPP voltammograms that signal changes are due mostly to changes in refractive index between reduced and oxidized forms of redox species. Furthermore, we show that energetic carriers resulting from SPP absorption significantly improve the sensitivity of electrochemical detection.

1.3 Copyright permissions

1.3.1 Chapter 3

The article in this chapter is presented in full and is reprinted with the permission of the Optical Society of America.

Z. Hirbodvash**,** M. Khodami, N. R. Fong, E. Lisicka-Skrzek, A. Olivieri, H. Northfield, R. N. Tait, P. Berini, "Grating couplers fabricated by e-beam lithography for long range surface plasmon waveguides embedded in a fluoropolymer" Applied Optics, 2994-3002 (58), 2019.

1.3.2 Chapter 4

The article in this chapter is presented in full and is reprinted with the permission of MDPI.

Z. Hirbodvash, M. S. E. Houache, O. Krupin, M. Khodami, H. Northfield, A. Olivieri, E. A. Baranova, P. Berini, “Electrochemical Performance of Lithographically-Defined Micro-Electrodes for Integration and Device Applications” Chemosensors, 277 (9), 2021.

1.3.3 Chapter 5

The article in this chapter is presented in full and is reprinted with the permission of AAAS.

Z. Hirbodvash, O. Krupin, H. Northfield, A. Olivieri, E. A. Baranova, P. Berini, “Infrared surface plasmons on a Au waveguide electrode open new redox channels associated with the transfer of energetic carriers” Science Advances, eabm9303 (8), 2022.

1.3.4 Chapter 6

The article in this chapter is presented in full and is reprinted with the permission of ACS.

Z. Hirbodvash, E. A. Baranova, P. Berini, “Real-time convolutional voltammetry enhanced by energetic (hot) electrons and holes on a surface plasmon waveguide electrode” Analytical Chemistry, 13145–13152 (94), 2022.

Chapter 2.

Background and Literature Review

2.1 Plasmonic

2.1.1 Electromagnetics of Metals

A classical theory based on Maxwell's equations describes the interactions of electromagnetic waves with metals at frequencies up to the visible spectrum. Metals were traditionally used for circuitry and guiding microwaves or far-infrared EM waves. Metals can be considered perfect electric conductors (PEC) in these applications since the conduction electrons cancel out the external charge field, effectively preventing a wave's propagation through the metal. Field penetration increases as frequencies increase toward the near-infrared and visible portions of the spectrum, which results in increased absorption and dissipation. Metals exhibit complex, frequency-dependent dielectric functions in this region of the spectrum. The metal permittivity can be described by various models. In the following, two well-known models, Drude-Sommerfeld and Drude Lorentz models are explained.

2.1.2 The plasma models

The permittivity of metals at optical frequencies can be described in a very simple way. Metals can be modelled to a first-order approximation as a plasma (free electron gas). Electromagnetic waves produce electron oscillations with respect to a lattice of positive ions. An oscillation can be described by its frequency, and interaction with the lattice by the collision frequency which is inversely proportional to the relaxation time of the free electrons. In this model, the free electrons constitute a cold plasma.

The expression for the dielectric function of a plasma is expressed using the Drude-Sommerfeld model [44]:

$$\varepsilon(\omega) = 1 - \frac{\omega_p^2}{\omega^2 + i\gamma\omega} \tag{1}$$

where ω_p is the plasma frequency, γ is collision frequency which is proportional to the inverse value of relaxation time of the electrons ($\tau = 1/\gamma$) [45], and $\varepsilon(\omega)$ is relative permittivity. The plasma frequency is given by

$$\omega_p = \sqrt{\frac{n_e e^2}{m^* \varepsilon_0}} \tag{2}$$

in which n_e is electron density, e is the electron charge, m^* is the effective electronic mass and ε_0 is the permittivity of free space. The plasma frequency occurs in the visible range for most metals.

The frequency dependent dielectric function of a plasma has real and imaginary components:

$$Re\,\{\varepsilon(\omega)\} = 1 - \frac{\omega_p^2}{\omega^2 + \gamma^2} \tag{3}$$

$$Im\,\{\varepsilon(\omega)\} = \frac{\gamma\omega_p^2}{\gamma(\omega^2 + \gamma^2)} \tag{4}$$

The plasma (free electron gas) behaves as a metal if $\omega_p > \omega$. Permittivity is mostly real, and the medium acts as an undamped free-electron plasma.

For $\omega_p \leq \omega$, corresponding to short visible wavelengths and the ultraviolet region for most metals, the free electron gas model does not match the observed permittivity behavior, due to the existence of vertical (inter-band) electron transitions in the metal – in this case the

Drude-Sommerfeld model needs a correction. Inter-band electron transitions increase the imaginary component of the permittivity dramatically [44]. Terms are added to the Drude-Sommerfeld model to improve the accuracy of the dielectric function [46,47]:

$$\varepsilon(\omega) = \varepsilon_\infty - \frac{\omega_p^2}{\omega^2 + i\gamma\omega} + \varepsilon_{int}(\omega) \tag{5}$$

where ε_∞ is a material specific polarization correction factor and $\varepsilon_{int}(\omega)$ is a fitted permittivity which corrects for the inter-band transitions, described as [46,47]:

$$\varepsilon_{int}(\omega) = 1 - \frac{\widetilde{\omega}_p{}^2}{(\omega_\circ{}^2 - \omega^2) - i\gamma\omega} \tag{6}$$

where $\widetilde{\omega}_p$ is analogous to ω_p in the Drude-Sommerfeld model. This model is called the Drude-Lorentz model.

Because of the complex optical response of metals, the optical permittivity functions of metals are usually derived from experimentally determined values [47,48]. Fig. 1. shows the real and imaginary parts of gold's optical permittivity based on the Drude-Sommerfeld and Drude-Lorentz formulas and experimental data all from reference [49]. Most of the metals at optical frequencies show plasma behavior: for gold $\omega_p = 13.8 \times 10^{15}/s, \gamma = 1.075 \times 10^{14}/s$ such that gold appears metallic throughout most of the visible and all the infra-red spectral regions, approaching a perfect electric conductor at long wavelengths beyond about 10 μm.

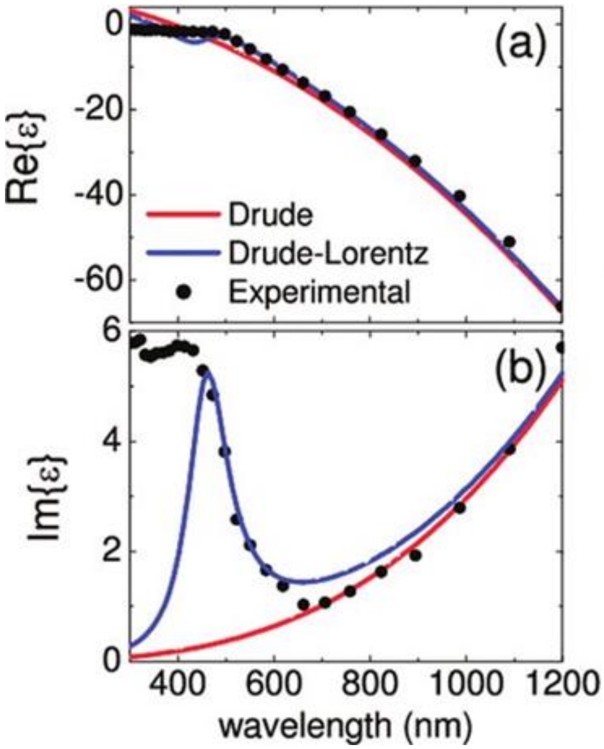

Fig. 1. (a) Real and (b)imaginary parts of the permittivity of gold in the optical regime. Black dots correspond to the experimental data. The red and blue lines are fits to the Drude-Sommerfeld and Drude-Lorentz formulas. Reproduced with permission [49].

2.1.3 Surface Plasmon Polaritons (SPPs)

Electromagnetic (EM) waves in the visible and near-infrared ranges, under the right circumstances, can couple to electron oscillations on the surface. Appropriate excitation leads to an induced quantized oscillations referred to as surface plasmons. Hence, surface plasmons (SPs) at metal surfaces are resonant collective electron oscillations that are coupled to an evanescent light field [44,49-51]. Plasma oscillations of a conduction electron gas on the surface of metallic structures can couple with incident light to form surface plasmon polaritons (SPPs). The two main groups of SPPs are propagating surface plasmon polaritons (PSPP) and localized surface plasmon polaritons (LSPP). LSPP refers to surface plasmons that exist on the surface of a nanostructure such as nanoparticles.

The electromagnetic excitation propagating at the planar interface between a dielectric and a conductor, evanescently confined in the perpendicular direction, is known as a propagating SPP [44,49-51]. In Fig. 2, the SPP in the interface of a metal and dielectric is illustrated.

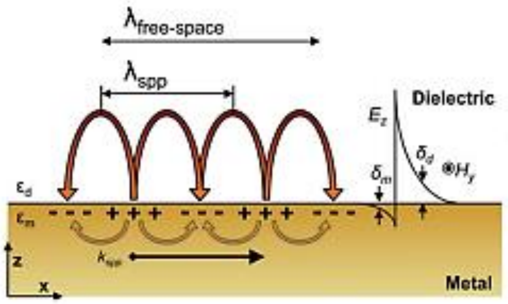

Fig. 2. Coupled excitation between EM fields (curved lines) and electron surface charge density (+ and -) forming surface plasmon polaritons propagating at a metal-dielectric interface.

As is depicted in Fig. 2, the coupled excitation involves EM fields that induce a coherent oscillation of surface charges indicated by the "+" and "-" signs - the curved arrows indicate the associated electric fields. The SPP will propagate along the interface in the *x*-direction with a complex propagation constant K_{spp} implying an exponential decay with propagation due to absorption.

According to the boundary conditions, the electric displacement field (D_z) has to be continuous across the boundary such that $\varepsilon_m E_{z,m} = \varepsilon_d E_{z,d}$, where ε_d is the relative permittivity of the dielectric, ε_m is the real part of the relative permittivity of the metal, and E_z is the electrical field in both regions. Since $\varepsilon_m \neq \varepsilon_d$, there is a discontinuity at the surface in the electric field, resulting in surface charges at the interface. The real permittivity of plasma metals at these frequencies is negative, while the permittivity of dielectrics is positive, resulting in a change in direction of the electric field across the interface, which implies the propagation of an optical wave coupled to electron oscillations as diagrammed. The EM portion within the dielectric is called a polariton and the surface electron oscillation a plasmon, so the mode is termed a surface plasmon polariton. TE polarized waves (s-polarized) have no E field component perpendicular to the surface, thus cannot induce significant polarization, so only TM (p-polarized) modes can propagate.

Solving the vector wave equations for a planar interface between semi-infinite metal and dielectric media (single interface) yields the dispersion equation for propagating SPPs as follows [53]:

$$K_{sp} = \frac{\omega}{c}\sqrt{\frac{\varepsilon_d \varepsilon_m}{\varepsilon_d + \varepsilon_m}} \tag{7}$$

in which ω is the optical angular frequency, and c is the speed of light in free space. Based on the Drude-Sommerfeld model, ε_m can be expressed as in Eq. (3). For visible and near-infrared light, $\gamma \ll \omega_p$, so the Eq. (3) is often simplified to:

$$\varepsilon_m = 1 - \frac{\omega_p^2}{\omega^2} \tag{8}$$

The dispersion curve of the propagating SPP can be plotted by inserting Eq. (8) in Eq (7), as shown in Fig. 3. SPPs behave like free space photons at low frequencies, but their dispersion curves move increasingly to the right of the light line as frequency increases. At the surface plasma frequency, $\omega_{L=\frac{\omega_P}{\sqrt{2}}}$, K_{sp} reaches an asymptotic limit. The dispersion curve bends to the right of the light line, so the SPP has greater momentum than incident light, which means it cannot be excited directly by light. Usually, a prism or a grating coupler is used to add extra momentum to the incident light. By using these mechanisms, the momentum mismatch is compensated, allowing light to couple into propagating SPPs that travel along with the dielectric-metal interface.

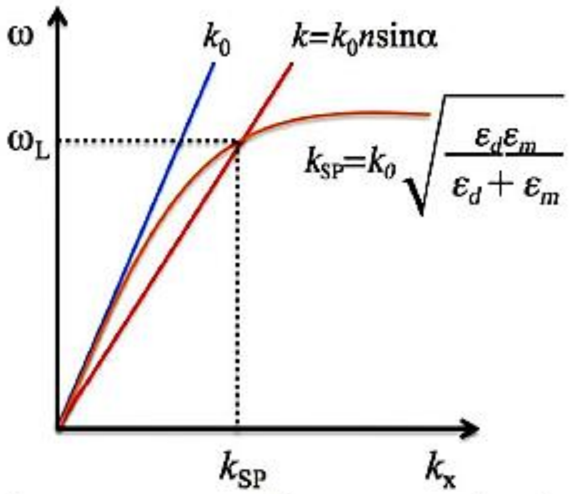

Fig. 3. A dispersion plot of a SP mode shows the problem of momentum mismatch between illuminated light (blue line) and SP modes (orange line). It is necessary to overcome momentum mismatch in order to couple the light and SP modes together, with the SP mode lying always beyond the light line, having higher momentum (K_{sp}) than a free space photon (k_0) of the same frequency. In order to provide additional momentum, one can use the evanescent wave produced in TIR, $k = k_0\ n\ sin\alpha$ (red line).

Fig. 4(a) illustrates a 1D electric field profile for the single-interface SPP where there is a semi-infinite metal of permittivity ε_m and a dielectric of permittivity ε_{d1} [46]. The *z*-component of the electric field in a single-interface SPP peaks at the interface and decays exponentially on each side. A single-interface SPP propagates along the surface until its energy is dissipated via absorption in the metal (resistive loss) or scattered. This leads to a propagation length of the order of 10 to 100 µm for plasmonic material around visible and near-infrared wavelengths. Most common plasmonic metals over the visible and near-infrared ranges are Al, Ag, Au and Cu [55].

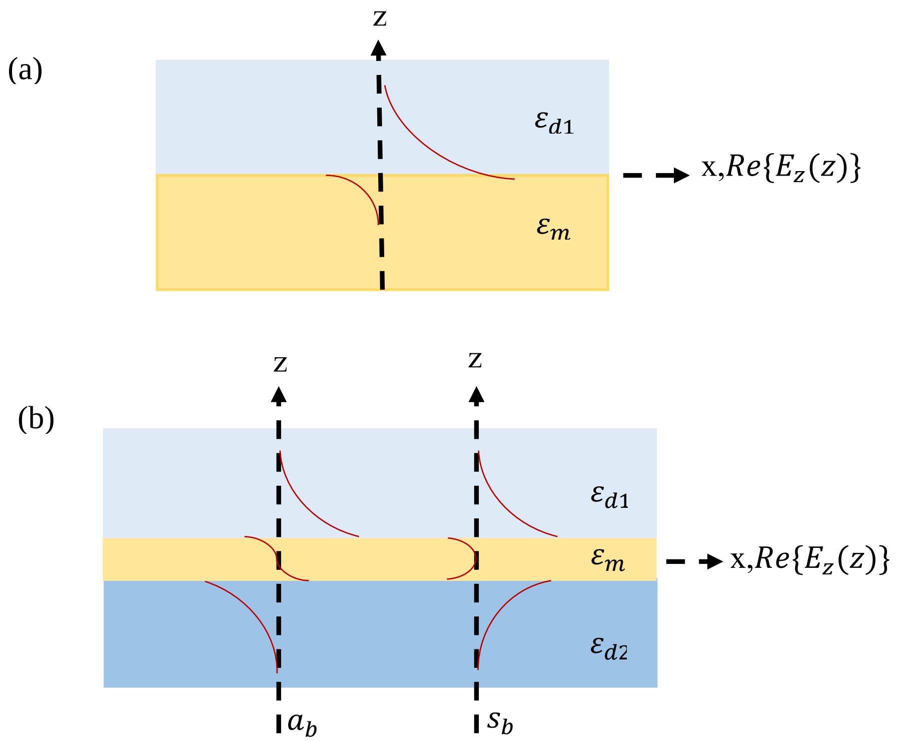

Fig. 4. 1D electric field profiles for: (a) Single-interface SPP; (b) coupled SPP modes on a thin metal layer.

Fig. 4(b) illustrates a finite thickness metal slab with dielectrics on both sides. Here, the two SPPs become bound coupled modes (sometimes referred to as mixed modes or supermodes). They are described by symmetric (s_b) or asymmetric (a_b) transverse electric field profiles as sketched.

An interesting condition occurs for the modes on the metal slab if the permittivity of the surrounding dielectrics (lower-cladding and upper-cladding) are equal ($\varepsilon_{d1} = \varepsilon_{d2}$), and both claddings are lossless (dielectric) [56]. The symmetric mode has decreasing attenuation with decreasing metal thickness as the electric field within the metal will be increasingly expelled. Conversely, the asymmetric mode will have increased confinement in the metal with decreasing thickness and thus increasing attenuation. The symmetric mode is known as a long-range surface plasmon polariton (LRSPP). LRSPP modes have lower attenuation (at least one to two orders of magnitude) than their single interface and asymmetric counterparts. The lowered attenuation allows for longer propagation lengths and much longer interaction lengths in sensor applications.

2.1.4 2D plasmon waveguides

Fig. 4(b) shows a slab of thickness *t* surrounded by a lower and upper cladding in 1D (infinite in *x* and *y* directions, finite in *z*). However, the metal slab can be limited to a width *w*, forming a metal stripe. Such a situation is depicted in Fig. 5.

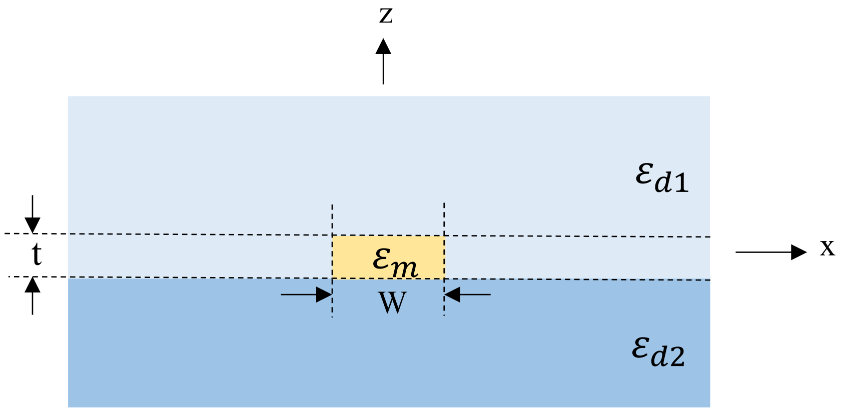

Fig. 5. Metal stripe of finite width (infinite in *x*, propagation in *y*). The substrate and cladding are not necessarily the same, but $\varepsilon_{d1} = \varepsilon_{d2}$ is required for LRSPP propagation.

As shown in Fig. 4(b), the slab waveguide, has two fundamental modes (a_b and s_b). These two fundamental modes are either asymmetric or symmetric about the *x*-axis. Fig. 5 shows the additional horizontal confinement. As a result of the width limitation, lateral confinement occurs, dramatically changing the modal solutions. This horizontal confinement adds modes to the system that can be symmetric or asymmetric about the *z*-axis. This leads to having four fundamental modes in the case of metal stripe, including one that is symmetric about both the x and z axes (referred to as the ss_b° mode). This symmetric mode has the lowest attenuation and is referred to as the LRSPP mode of the stripe waveguide [57]. This metal stripe structure facilitated the fabrication of passive integrated optical structures such as straight waveguides, bends, splitters, and Mach-Zehnder interferometers for sensing applications [58].

The lateral confinement changes the modal solutions dramatically, and modal analysis requires the use of numerical methods. Numerical methods for modal calculations include the method of lines (MoL) [59], the finite element method (FEM) [60] or the finite difference method (FDM) [61]. If the permittivity of the lower cladding equals the upper cladding, a long-range mode can be supported like the metal slab case. If the incident beam profile overlaps the symmetric LRSPP profile, a high coupling efficiency can be achieved.

2.1.5 Excitation Techniques of Surface Plasmon Polaritons

To excite SPPs, both energy and momentum (phase matching) conservation must be fulfilled. Phase matching requires that the propagation constants of the input light ($k = \frac{\omega}{c}$) be equal to the propagation constant of the SPP (K_{sp}). Fig. 3. shows that K_{sp} is always larger than k for single-interface SPPs, so the direct excitation of SPPs is not possible.

The most common technique to excite SPPs is via prism coupling where the attenuated total reflection (ATR) condition is indicative of SPP excitation at the metal dielectric interface. The Otto configuration is one prism-coupling method used to excite single-interface SPPs [56] where a dielectric gap is placed between the prism and the metal surface. The Kretschmann–Raether configuration for exciting single-interface SPPs is more convenient as the metal film is deposited directly onto the base of the prism (Fig. 6)

[56]. A prism-coupled system based on the Kretschmann-Raether configuration is the most common method of exciting SPPs in Surface Plasmon Resonance (SPR) sensors [64-66].

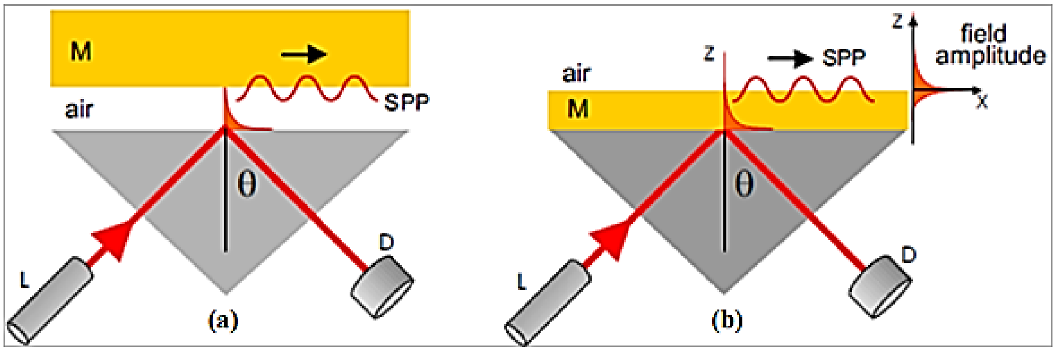

Fig. 6. Excitation of surface plasmon using Otto (left) and Kretschmann (right) configurations . Reproduced with permission [67]. M: Metal, L: Laser, and D: Detector

In the Kretschmann geometry, the momentum matching condition for the excitation of SPPs on the metal film is described as:

$$k_x = \left(\frac{2\pi}{\lambda}\right) n_p \sin\theta = Re\{K_{sp}\} \tag{9}$$

where k_x is the wavenumber of the incident light at incident angle θ which can coupled into SPPs, and n_p is the refractive index of the prism.

Conventional SPR biosensors based on the Kretschmann-Raether configuration use a glass prism to excite surface plasmons. An immobilized bio-recognition element is coated on the metal surface as shown in Fig. 7. Plasmon excitation occurs at a specific angle termed the SPR angle. At this angle, the incident light is coupled to SPPs which leads to a decrease in the intensity of the reflected beam. The refractive index of the sensing solution and the presence of an adlayer at the metal/solution interface determine the SPR angle. Biochemical reactions change the thickness of the adlayer which changes the SPR angle required to maintain excitation of SPPs. Changing the refractive index of the dielectric medium on the other side of the metal film, or forming an adlayer thereon, will result in significant changes in the SPP coupling angle (Eq. (9), as K_{sp} is altered). Plotting the intensity *vs*. the incident angle over time produces a sensorgram from which binding kinetics can be extracted [68,69].

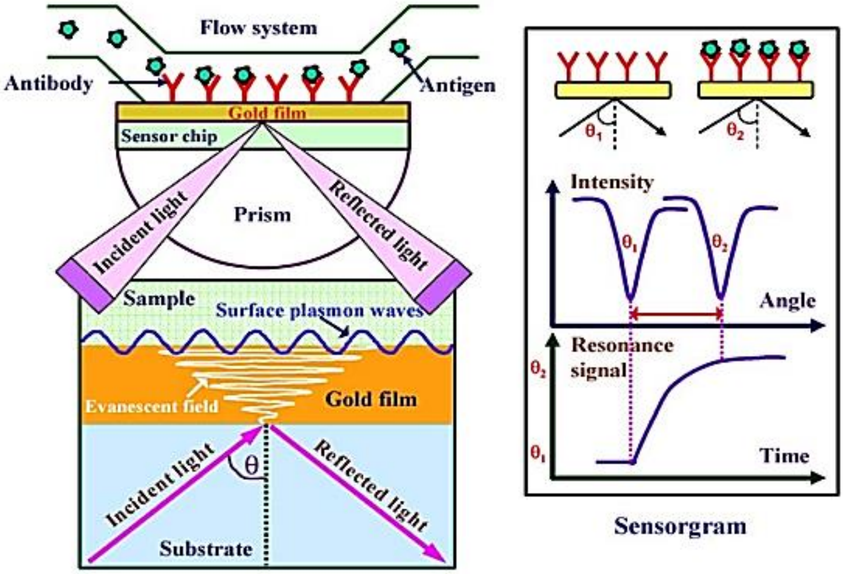

Fig. 7. Schematic view of the SPR immunoassay technique. Reproduced with permission [69].

Wavelength interrogation is also possible, where the excitation of propagating SPPs is revealed as the appearance of a dip in the reflectance spectrum, for a fixed angle of incidence. The spectral width of this dip is typically ~50 nm full width at half-maximum (FWHM) for Au films [70], and it is accompanied by an apparent phase change near the minimum of the resonance for the reflected light. SPR biosensors conventionally exploit single-interface SPPs which have a high attenuation and broad resonance conditions.

LRSPP excitation can be done either by a prism coupled system based on attenuated total reflection (ATR) or in an end-fibre coupling scheme (butt coupling) using a TM polarized laser beam [71,72].

In a prism-coupled system, the incident angle can be changed beyond the critical angle and the reflected power is monitored using a photodetector as shown in Fig. 8.

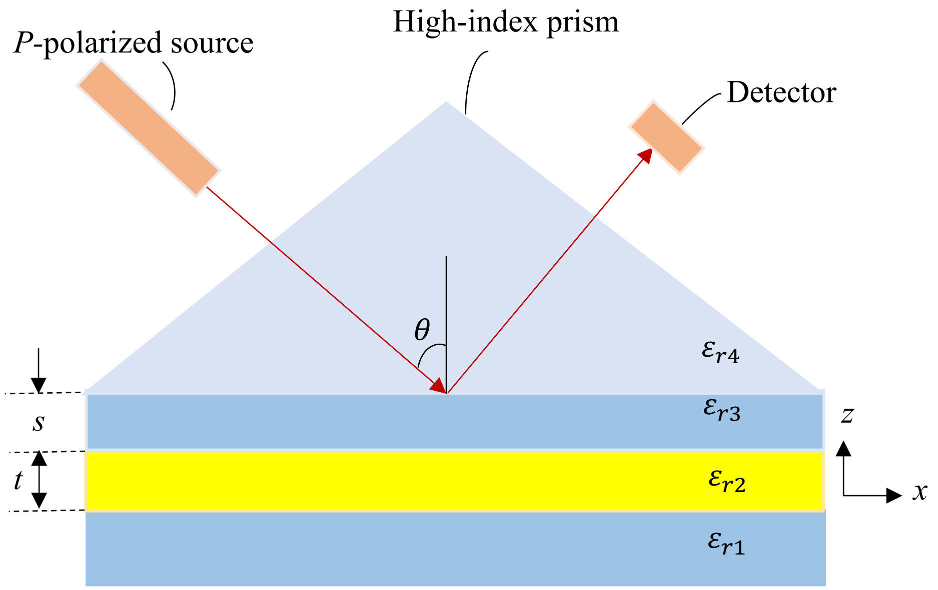

Fig. 8. Prism coupling technique for exciting LRSPPs.

The wavenumber of the incident beam is equal to the wavenumber of the propagating LRSPP mode at a certain angle, and a drop in the reflected power is observed (similar to the Kretschmann-Raether configuration for single-interface SPPs). In this configuration a thin metal slab is bounded by two dielectric (insulator) layers forming an insulator-metal-insulator (IMI) structure that can support LRSPPs. Although prism coupling is simple, it can be somewhat bulky and often impractical.

Another method of exciting SPPs and LRSPPs is with grating couplers. Fig. 9 shows a grating, formed of either periodic bumps or trenches, with a period of Λ. Grating couplers must be designed to satisfy the momentum conservation condition [68]:

$$\Lambda = m\lambda_{\circ}(n_{eff} - n_c \sin\theta) \tag{10}$$

Where m is the (integer) order of the grating, n_{eff} is the average effective index of the LRSPP mode propagating along the waveguide with the grating, λ_0 is the free-space operating wavelength, n_c is the refractive index of the medium from which the beam is incident, and θ is the angle of incidence.

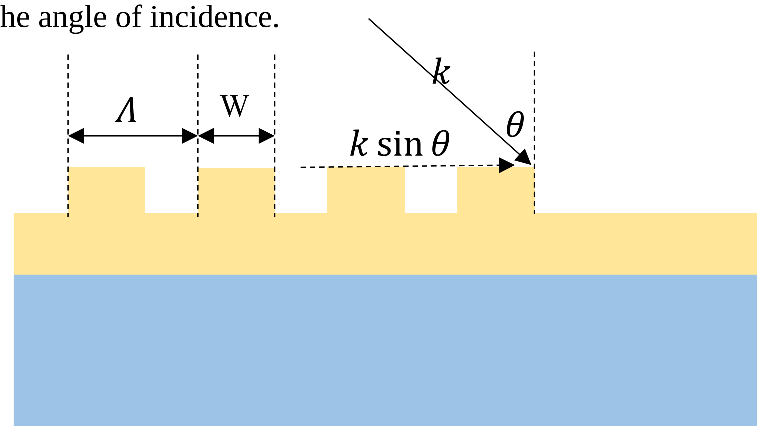

Fig. 9. Example of a grating coupler for SPPs as a step-in-height metal pattern.

Fig. 9 shows periodicity in the metal pattern, but the grating can be patterned as another material such as a dielectric. These couplers work by scattering incoming light with propagation constant k at incident angle θ into SPPs. The component of the scattered light which matches the propagation constant of the SPP (K_{sp}) will couple that energy into the waveguide. The phase matching condition is described as follows:

$$K_{sp} = k \sin\theta \pm m \frac{2\pi}{\Lambda} \tag{11}$$

where m is an integer, The grating coupler can be designed to excite a specific mode of interest. Grating couplers are easy to align and excite but the coupling efficiency is limited due to the nature of the structure.

2.2 Bloch long-range surface plasmon polaritons (Bloch LRSPPs)

For waveguide structures as shown in Fig. 4(b), the mode propagates in the *y* direction with a complex propagation constant, $\gamma = \alpha + i\beta$, where α is the attenuation constant and β is the phase constant. The mode power attenuation (MPA) in dB/m computed from attenuation constant α is [45]:

$$MPA = 20\,\alpha\,\log_{10} e \tag{12}$$

The mode power is reduced by a factor of 1/e in a distance from the launch point defined as the propagation length of the mode (L_e) [45]:

$$L_e = \frac{1}{2\alpha} \tag{13}$$

The coupling efficiency can be obtained by estimating the overlap factor *C* of the LRSPP mode (ss_b°) with the source field. The overlap factor is:

$$C = \frac{\iint E_{z1}.E_{z2}^{*}\,dA}{\sqrt{(\iint E_{z1}.E_{z1}^{*}\,dA)(\iint E_{z2}.E_{z2}^{*}\,dA)}} \tag{14}$$

which is computed from the transverse spatial distribution of the main transverse electric-field component of the LRSPP, E_{z1}, and the source field, E_{z2}.

The mode power coupling efficiency is given by $|C|^2$ if there is no discontinuity in the materials at the coupling plane. The mode power coupling loss (C_{pl}) is expressed in dB:

$$C_{pl} = -20\,\log_{10}|C| \tag{15}$$

In biosensing applications, the choice of bottom cladding material depends on the bulk refractive index of the target sensing fluid. Most sensing fluids in biosensor applications are aqueous in nature - clean buffers carrying analyte or patient samples (urine, blood) diluted in buffer, for example. Thus, the choice of bottom cladding or substrate should be limited to materials that have a refractive index close to water, such as Cytop [73] and Teflon [74]. An alternative method is using a truncated one-dimensional photonic crystal (1DPC) [43]. 1DPC can be used as a lower cladding, and it can mimic the optical properties of the medium on the other side of the metal stripe or slab over a limited range of wavenumber and wavelength. Such a mode supported in this structure is called a Bloch LRSPP.

Fig. 10(a) shows the structure of interest. The 1DPC is formed on a Si substrate and covered by an optically infinite Cytop layer. In this structure, a 5 µm wide, 35 nm-thick Au ($n_{Au} = 0.448 + i9.228$) stripe is deposited on top of a 0.5 nm-thick Cr layer ($n_{Cr} = 4.467 + i4.519$) for adhesion purposes, on top of a truncated 1DPC, defined as a $\mathrm{SiO_2/Ta_2O_5}$ multilayer stack constructed of N = 12 periods, $d_{\mathrm{SiO_2}} = 625$ nm ($n_{\mathrm{SiO_2}} = 1.447$) and $d_{\mathrm{Ta_2O_5}} = 209$ nm ($n_{\mathrm{Ta_2O_5}} = 2.069$). Each layer was chosen for its thickness to tailor the field decay in the stack and minimize losses from light tunnelling into the Si substrate. In the stack, a top capping layer of $\mathrm{SiO_2}$ of thickness d_{first} = 462 nm, was selected to obtain an SPP supported by the stack at λ_0 = 1310 nm of the same wavenumber as an SPP supported by the corresponding Au/Cytop system [43]. The dispersion diagram is shown in Fig. 10 (b). The dispersion diagram shows Bloch LRSPP guided by a gold stripe on a truncated 1DPC (solid green) and the LRSPP guided by a gold stripe buried in Cytop (solid red). k_{SP} is defined as Eq. (16):

$$k_{SP}=\frac{\omega_0}{c}\sqrt{\frac{\varepsilon_{Cytop}\varepsilon_{Au}}{\varepsilon_{Cytop+}\,\varepsilon_{Au}}}=(6.4846+i8.3428\times10^{-3})\mu m^{-1} \tag{16}$$

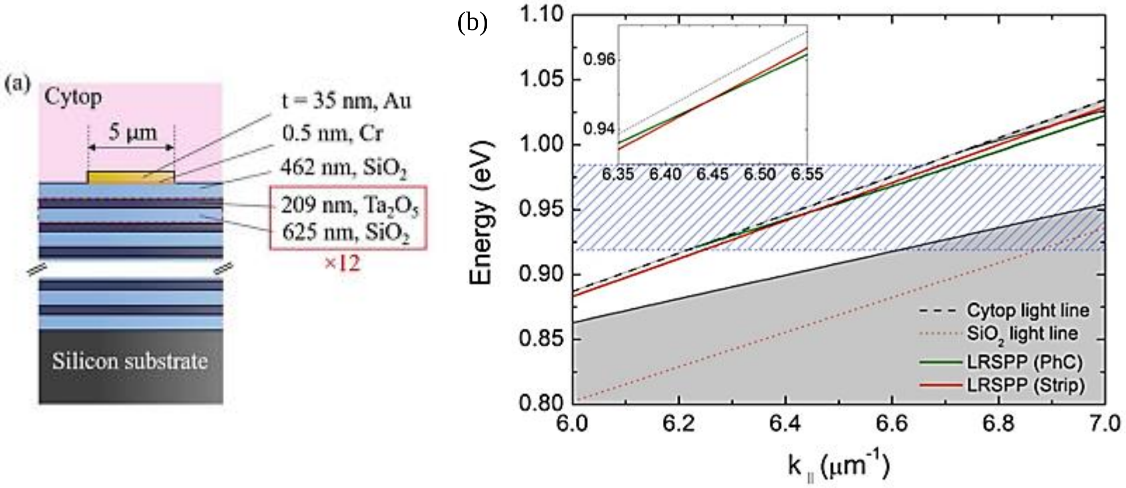

Fig. 10. Dispersion diagram of the Bloch LRSPP guided by a gold stripe on a truncated 1DPC (solid green) compared to the LRSPP guided by a gold stripe buried in Cytop. Reproduced with permission [43].

It is possible to observe the opening of a photonic bandgap in an ideal dielectric structure, whose position and width are determined by the system's material and geometric properties. Considering the finite number of periods (N = 12), a high reflectivity spectral region (a stopband) is expected [43], which models the ideal bandgap. Also, the presence of a truncated layer creates a defect mode within the stopband, which is well-located near the surface, namely at the interface between the Au and SiO_2 layers. The dispersion relation of both LRSPPs (Cytop embedded, red; and Bloch LRSPP, green) is nearly identical around the target wavelength ($\lambda_0 = 1310$ nm) [43].

The dispersion diagram depends critically on the design of the unit cell as well as the design of the cap layer (*i.e.*, the SiO_2 layer of thickness d_{first}). It is crucial to know the refractive index of the materials used when fabricating a design for maximum reliability. There is a possibility that the refractive index characteristic of amorphous materials may cause the wavelength to shift. In Fig. 10, the blue hatched region represents the energy range in which the working point would fluctuate assuming a variation of ±10% in the optical thickness of each layer [43]. As shown in the blue hatched region, the mode power attenuation (MPA) of the Bloch LRSPP shows very little deviation from the LRSPP in the corresponding Cytop structure, with values ranging from 11 to 12 dB/mm. In Fig. 10, the gray shaded region corresponds to the area below the light line of Cytop but outside the photonic bandgap.

Fig. 11 shows the perpendicular (E_y) field amplitude squared profiles of the modes, computed by the FDE (Finite Difference Eigenmode) method, for the LRSPP on the corresponding structure (Cytop embedded) and for the Bloch LRSPP on the truncated 1DPC. MPAs of 6.8 and 11 dB/mm are calculated for each, leading to propagation lengths of $\mathrm{L}_{\mathrm{Cytop}} = 638\ \mu m$ and $\mathrm{L}_{\mathrm{1DPC}} = 389\ \mu m$.

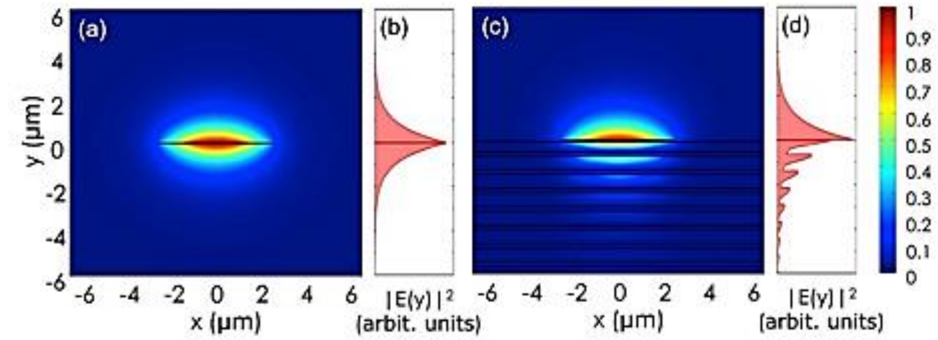

Fig. 11. Profiles of the amplitude squared of the perpendicular electric field (E_y) for: (a) and (b) the LRSPP on a stripe of Au buried in Cytop; and (c) and (d) the Bloch LRSPP on a Au stripe on a 1DPC with a Cytop upper cladding. Reproduced with permission[43].

The slightly larger field fraction in the gold stripe on the 1DPC structure accounts for the difference in propagation losses between the modes. Similarly, the field distribution within the Cytop upper cladding is similar in both cases, while the distribution within the 1DPC exhibits oscillatory behavior corresponding to the Bloch LRSPP propagating in the plane of a truncated 1DPC within the stopband. These modes display comparable lateral extent, indicating a similar confinement level and enabling bending in plane, leading to Bloch LRSPP integrated optical structures, such as S-bends, Y-junctions, couplers, and MachZehnder interferometers, comparable to these operating with LRSPPs [56]. The vertical extend of the modes is also comparable, so Bloch LRSPPs should exhibit similar sensing performance to LRSPPs waveguides [75,76].

Fig. 12 schematically illustrates an excitation scheme consisting of illuminating a Au grating coupler on a Au stripe with a *p*-polarized Gaussian beam launched using an aligned optical fiber.

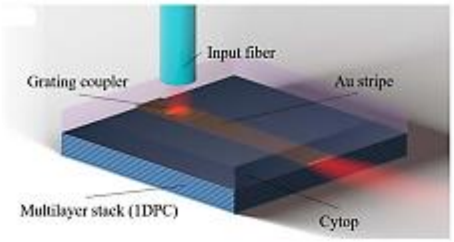

Fig. 12. 3D sketch of the metal stripe waveguide with a grating coupler, illustrating an excitation arrangement. Reproduced with permission [43].

Such an excitation scheme has the advantage of not requiring a high-quality input facet, as well as simpler optical alignments in comparison to butt-coupling. However, the coupling efficiency is typically lower in such a scheme. The grating design selected consists of 16 rectangular ridges of dimensions W and H disposed over a period of Λ. The grating was modeled in the frequency domain with the 2D FEM using software available commercially, and the coupling efficiency was calculated by capturing the power carried by the Bloch

LRSPP far away from the grating region (150 μm to the left) to eliminate the effects of spatial transients, as described in [77].

The coupling efficiency was maximized by optimizing the dimensions using a 2D model, H = 150 nm, W = 450 nm, and Λ = 1000 nm for t = 35 nm. A coupling efficiency of 16 % (coupling loss of 8 dB) is expected at $\lambda_0 = 1310$ nm over about 70 nm of bandwidth [43]. Using a full model, optimization of 3D grating designs is expected to further improve the coupling efficiency. Some modifications to the grating coupler design were implemented in the some of the works related to this thesis (Chapters 4, 5 and 6).

2.3 Principle of Plasmonic Sensors

There are two basic types of plasmon excitation techniques as discussed in sub-section 2.1.5, and correspondingly two types of biosensors: Kretschmann (prism coupling) and grating coupling [78-80]. Regardless of the excitation technique and sensor types, there are four primary optical interrogation methods that can be applied to both configurations. Firstly, phase interrogation, where a phase shift in the collected light indicates a change in refractive index, with the wavelength and angle of collection remaining constant. Secondly, there is angular interrogation, in which a single wavelength (monochromatic) laser is used and the shift in angle of SPP coupling is measured indicating refractive index changes. Thirdly, spectral interrogation uses a broadband source or tunable laser for plasmon excitation and a shift in the resonant wavelength of the reflectance/transmittance spectrum to examine the change in refractive index. Fourthly, intensity interrogation is a method that measures the change in transmitted and reflected light intensity, while maintaining constant the wavelength and the angle at which the signal is collected [78].

Structures for sensing applications can be characterized by parameters such as bulk sensitivity, surface sensitivity, and figure of merit (FOM). Bulk sensitivity is defined as a change in measurand, *e.g.*, a resonant wavelength λ_{res} *vs*. the change in refractive of the bounding medium (*e.g.*, $\partial\lambda_{res}/\partial n_c$). By changing the refractive index of the bounding medium from nominal value to another, step by step, one can calculate the bulk sensitivity [78].

With the change in thickness of an adlayer, which develops at the interface between the metal and the bounding medium, the surface sensitivity determines how the measurand shifts. The metal surface in biosensing experiments is in contact with a sensing solution (bounding medium) and is functionalized chemically to react selectively with a target analyte. As analyte attaches, an adlayer of a higher refractive index than the sensing solution forms, causing a shift in measurand. The surface sensitivity can be defined as the shift in the measurand, *e.g.*, a resonance wavelength λ_{res}, as a function of adlayer thickness a at the metallic/solution interface (*e.g.*, $\partial\lambda_{res}/\partial a$). However, the overall sensing performance of a system also depends on the spectral width of a resonance. The narrower the resonance, the more accurate the measurement of small shifts in the resonance wavelength caused by changes in the bounding medium's refractive index. In general, the FOM is defined as the ratio of the resonance wavelength shift to the refractive index change (bulk sensitivity) divided by the resonance spectral width and is used to evaluate the overall quality of a sensor [78].

In this thesis, we focus on studying LRSPPs and their role in electrochemical detection. In recent years, many theoretical and experimental studies have been carried out as researchers have designed and tested SPPs, LSPPs, and LRSPPs in conjugation with electrochemical approaches for a variety of applications, especially sensing. The following section reviews some of these studies.

2.4 Electrochemical surface plasmon resonance

Electrochemical surface plasmon resonance (EC-SPR) records optical faradaic processes by monitoring the change in refractive index that happens with a change in redox state at the electrode surface in electrochemical Kretschmann SPR systems [81]. EC-SPR is an important application of SPR to study local electrochemical reactions on the surface of the electrode.

Cyclic voltammetry (CV) is a powerful electrochemical technique that investigates the reduction and oxidation processes of molecular species. The following section explains cyclic voltammetry [82].

2.4.1 Cyclic voltammetry

Electrochemical methods, such as cyclic voltammetry (CV), are widely used to study molecular reduction and oxidation processes. CV is also useful for studying chemical reactions initiated by electron transfer, such as catalysis. The traces in Fig. 13 are called voltammograms or cyclic voltammograms [83]. Here, the *x*-axis represents a parameter imposed on the system, the applied potential (V), and the *y*-axis represents the response (measurand), the resulting current (C). CV data are commonly reported using two conventions, but sign convention used to obtain and plot the data is rarely stated. As shown in Fig. 13, the potential axis gives a clue to the convention used.

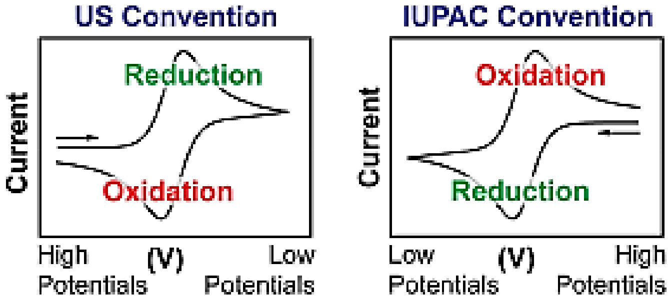

Fig. 13. Schematic voltammograms. To report CV data, US and IUPAC conventions are commonly used. The data reported in the two conventions appears rotated by 180°. Reproduced with permission [83].

During a CV experiment, the potential is varied linearly at a rate of a few millivolts per second. This parameter is called the scan rate and it is one of the most important parameters in cyclic voltammetry. Fig. 14(a) shows the relation between time and an applied potential with the potential plotted on the *x*-axis to see the relationship with the corresponding voltage voltammogram of Fig. 14(b).

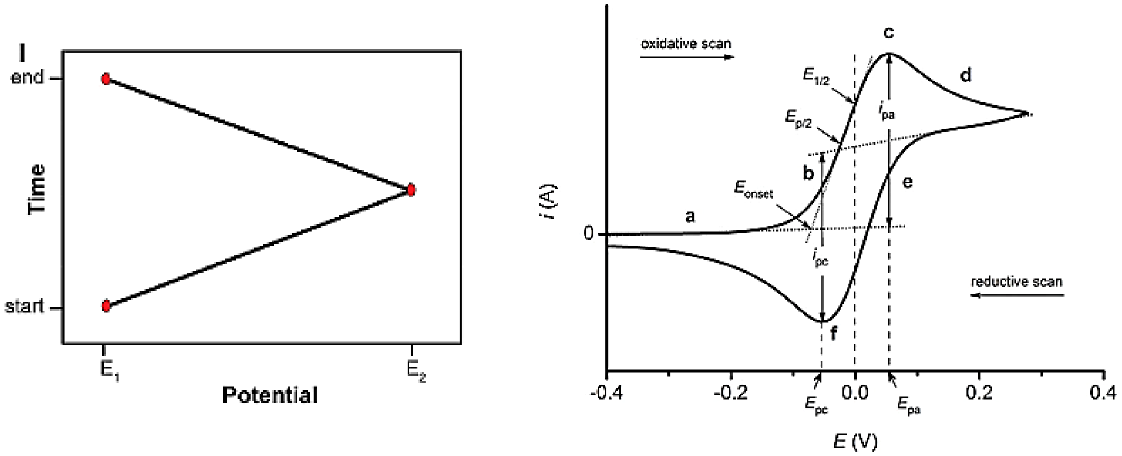
(a)

(b)

Fig. 14 (a) Applied potential as a function of time for a generic cyclic voltammetry experiment, with the initial, switching, and end potentials represented. Reproduced with permission [83]. (b) Voltammogram of a reversible reaction.

In Fig. 14, the potential is swept positively in the forward scan from the starting potential E_1 to the switching potential E_2. This is termed the anodic trace. The scan direction is then reversed, and the potential is swept positively back to E_1, called a cathodic trace.

Taking into account the equilibrium between oxidized and reduced species, the Nernst equation (Eq. 17) describes this equilibrium [83].

$$E = E^{\circ} + \frac{RT}{nF} \ln \frac{(OX)}{(Red)} = E^{\circ} + 2.3026 \log_{10} \frac{(OX)}{(Red)} \qquad (17)$$

The Nernst equation defines the potential of an electrochemical cell (E) as the standard potential of a species (E°) and the relative activities of the oxidized (Ox) and reduced (Red) analyte in the system at equilibrium. *F* is Faraday's constant, *R* is the universal gas constant, *n* is the number of electrons transferred in the reaction, and *T* is the temperature.

The formal potential is specific to the experimental conditions and is often determined by the $E_{1/2}$ value (average potential between points f and c in Fig. 14(b)). In response to a change in the concentration of a species in solution or a change in electrode potential, the Nernst equation provides a powerful way to predict how a system will respond. When $E = E^{\circ} = E_{1/2}$ is applied to a system, the Nernst equation predicts that oxidized form will be reduced to the reduced form until concentration of both reduction and oxidation species equal, and equilibrium will be achieved. As an alternative, when the potential is scanned during the CV experiment, the concentration of the species in solution near the electrode changes over time based on the Nernst equation.

The reduction of oxidized to reduced form locally at the electrode occurs when a solution of oxidized species is scanned to negative potentials, resulting in a current measurement and depletion of oxidized species at the electrode surface. Fig. 14(b) presents the resultant cyclic voltammogram.

When the potential is scanned negatively, the oxidized species is steadily depleted near the electrode as it is reduced to reduced form. At point c of Fig. 14(b), where the peak anodic current (i_{pc}) is observed, the current is determined by the delivery of additional oxidized species via diffusion from the bulk solution. During the scan, the diffusion layer continues to grow at the surface of the electrode containing the reduced species. As a result, mass transport of the oxidized species slows. Therefore, upon scanning to more negative potentials, the diffusion rate of the oxidized species from the bulk solution to the electrode surface slows down, resulting in a decrease in current (c → d, Fig. 14(b)). When the switching potential is reached, the scan direction is reversed, and the potential is scanned in the negative (cathodic) direction. The concentration of oxidized species at the electrode surface decreased, while the concentration of reduced species at the electrode surface increases, satisfying the Nernst equation. As the applied potential becomes more positive, the reduced species present at the electrode surface is oxidized. Following the Nernst equation, $E = E_{1/2}$, the concentration of oxidized and reduced species at the electrode surface is equal at points b and e (Fig. 14(b)). These two points correspond to the middle potential between the two observed peaks (c and f), which provides a straightforward way to estimate the E° for a reversible electron transfer. Due to the diffusion of analyte to and from the electrode, the two peaks are separated.

When the electrode reaction is controlled by diffusion, the plot of peak currents (anodic and cathodic), i_p, *vs*. the square root of the scan rate (ϑ) must satisfy the Randle-Sevcik equation [83]:

$$i_p = 0.4463\, nFAC \left(\frac{n\, F\vartheta D}{RT}\right)^{1/2} \tag{18}$$

where i_p is the peak oxidative current, n is the number of electrons transferred per redox event, A is the electrode area (m^2), D is the diffusion coefficient (m^2/s), C is the concentration of the redox species (mol/m^3), ϑ is the scan rate (V/s), R is the gas constant (J/(mol·K)), T is the temperature (K), and F is the Faraday constant (C/mol).

2.4.2 Electrochemical surface plasmon resonance – EC-SPR

One of the earliest comprehensive studies of SPR with CV was reported in reference [84]. In this work, EC-SPR analysis led to a new way to measure convolution voltammetry directly without the need for numerical integration of the current response.

According to reference [84], the EC-SPR signal is proportional to the electrochemical current density measured by conventional electrochemical methods. Based on the following equation, the SPR signal is a convolution of currents:

$$\Delta\theta(t) = B(\alpha_R D_R^{-1/2} - \alpha_0 D_0^{-1/2})\,(nF\pi^{\frac{1}{2}})^{-1} \times \int_0^t i(t')\;(t-t')^{-1/2}\,dt' \qquad (19)$$

where $\Delta\theta = \theta(t) - \theta_0$ measures the changes in SPR resonance (coupling) angle, the constant B (deg/RIU) represents the sensitivity of the SPR angle to changes in the bulk index of refraction (bulk sensitivity), which can be calibrated for a given SPR setup and reaction species, n is number of electrons transferred per reaction, F (C/mol) is the Faraday constant, D_0 (m^2/s) and D_R are the diffusion coefficients of the reaction species, and $\theta_0 = B(\alpha_0 C_0^0 + \alpha_R C_R^0)$ is the SPR angle at $t = 0$.

All experiments done in this article [84] utilized a prism based SPR imaging setup as illustrated in Fig. 15(A). This experiment utilized a BK7 triangle prism with a collimated red LED (wavelength 670 nm) as the light source and a high-speed CCD camera as the detector. As the SPR sensing surface, a gold-coated microscope coverslip was placed on the prism using index match fluid. Using the top opening of the electrochemical cell, a platinum wire counter electrode and an Ag/AgCl reference electrode were inserted into the electrochemical cell [84].

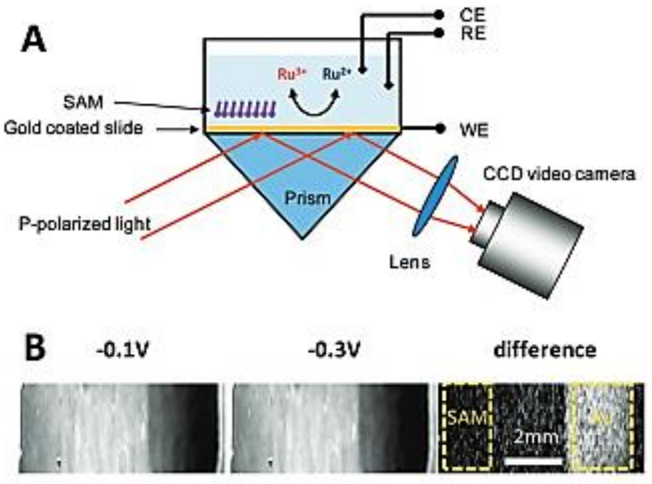

Fig. 15. (A) Illustration of the SPR setup. (B) SPR images in 11.78 mM $Ru\ (NH_3)_6^{3+}$ dissolved in phosphate buffer (0.5 M pH 7) at -0.1 and -0.3 V (*vs.* Ag/AgCl reference electrode) and their differences. Bare Au and SAM-coated areas used for data extraction and processing are indicated by yellow squares. Reproduced with permission [84].

In Fig. 16(A), the cyclic voltammograms are plotted for three scan rates, 0.01, 0.1, and 1.0 V/s, demonstrating that the peak current increases by 10 times when the scan rate is increased from 0.01 to 1.0 V/s. Voltammograms simultaneously recorded at different scan rates (Fig. 16(B)) illustrate that the total amount of SPR response is not dependent on the scan rate. The most important prediction of the theory is that the SPR voltammogram is simply a time convolution of the current (Eq. (17)).

From the current shown in Fig. 16(A), the SPR voltammogram was calculated using Eq. 17 and the coefficients $B\alpha_R$ (2.5 mDeg/mM) and $B\alpha_0$ (5 mDeg/mM) were independently calibrated [84].

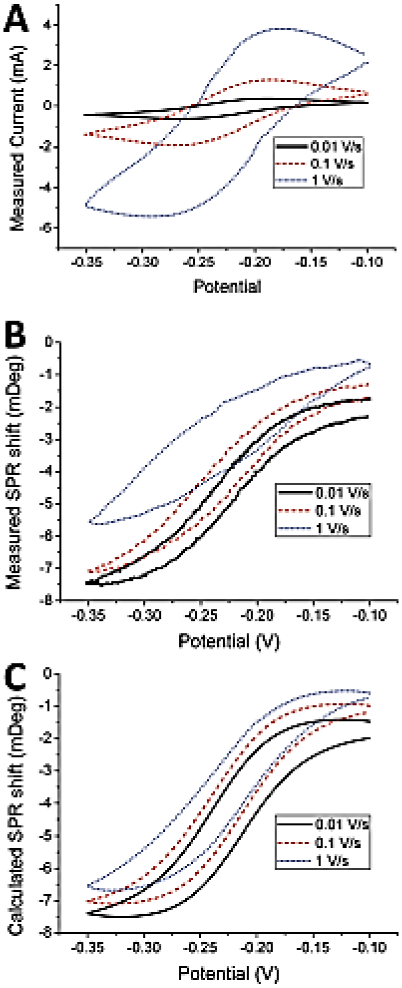

Fig. 16. A. Measured current voltammograms. B Measured SPR voltammograms. C SPR voltammograms calculated using Eq. 17 and the results of panel A as inputs. The electrolyte was 3 mM $Ru\ (NH_3)_6^{3+}$ in phosphate buffer and the electrode/SPR surface was bare gold. Reproduced with permission [84].

Prior studies of optical and electrochemical sensing platforms have exploited SPPs excited within prism-coupled systems (SPRs), in which electrochemical reactions affecting the metal/liquid interface shift the reflection minimum. A prism covered by a silver film was utilized in an ATR configuration with perchlorate and halide electrolytes as an optical probe of electrochemical reactions [85]. As the electrode potential becomes more positive, the resonance shifts to a smaller wave vector at a fixed wavelength (Fig. 17). Changes in electron density at the metal surface, ion adsorption, and changes in optical properties of the ionic double layer are some of the factors contributing to this shift.

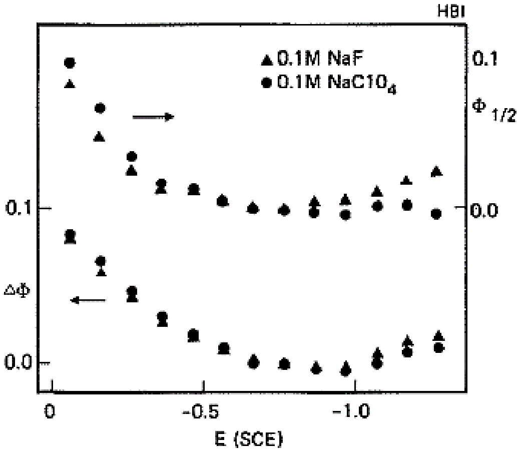

Fig. 17. Shift in peak position and width *vs*. potential for silver in 0.1 M NaF and 0.1 M $NaClO_4$. The shifts are relative to the position and width at -0.76 V. Reproduced with permission [85].

EC-SPR was also demonstrated to be a highly effective tool for detecting and measuring intermediates and is being explored as a potential tool for studying reaction kinetics. The semiquinone radical anion $\mathrm{BQ}^{\cdot -}$ was detected in the hydroquinone-benzoquinone ion system by producing a large negative shift on a flow-through electrochemical SPR system (Fig. 18) [86]. The study demonstrates that flow-through EC-SPR can be used to monitor not only surface interactions but also chemical reactions in solution.

During potentiostatic oxydoreduction, an electrochemical SPR biosensor with an absorptive redox mediator film was used to detect reversible refractive index changes in the film. Using the organic dye Methylene Blue (MB) as an electroactive label, this work examined the theoretical and experimental parameters of electrochemical SPR (eSPR) sensing. The electrochemical activation of the SPR response is dependent on the local MB concentration and can be used to design highly sensitive and selective biosensing systems. [87].

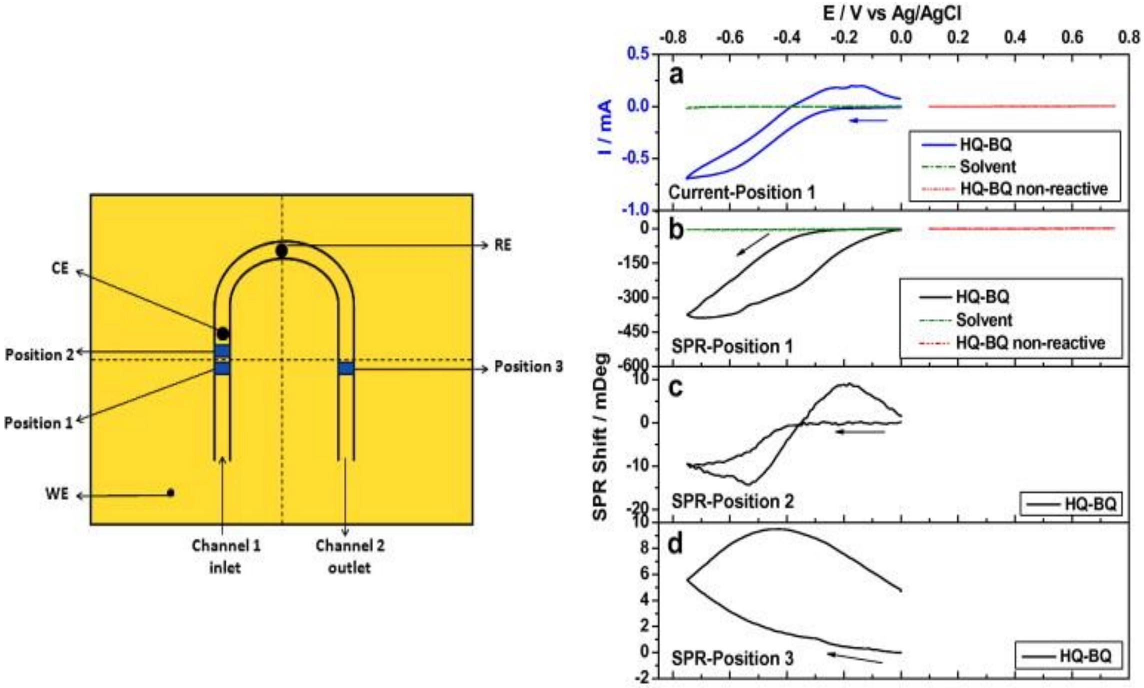

Fig. 18. Left panel: Gold-coated sensing chip with a flow channels and electrodes shown schematically (top view). The two channels are connected in a U-shape. The width, height, and length of each channel are respectively 2.0, 0.5, and 5 mm. The working electrode (WE) is connected to the sensing chip via a contact pin. The reference electrode (RE) and counter electrode (CE) are in the flow channel as shown in the figure. The solution enters the cell through channel 1 and exits through channel 2. Position 1 is located on the WE, while positions 2 and 3 are downstream. For 100 μL/min flow rate, it takes 0.1 s and 5 s

for a sample to flow from position 1 to positions 2 and 3, respectively. Right panel: Characterization of $BQ^{\bullet-}$ with CV-SPR at positions 1, 2 and 3 of the sensing chip. (a) Current of the HQ–BQ and solvent (0.1 M Bu_4NPF_6 in the acetonitrile), and HQ–BQ in a non-reactive potential window, (b) SPR signal of the HQ–BQ and solvent (0.1 M Bu_4NPF_6 in the acetonitrile), and HQ–BQ in a non-reactive potential window at position 1. (c) SPR signal of the HQ–BQ at position 2. (d) SPR signal of the HQ–BQ at position 3. Potential scan rate: 0.1 V/s. Flow rate 100 μL/min. Reproduced with permission[86].

Studies of localized surface plasmon resonance (LSPR)-based sensors with electrochemistry were also reported. It was demonstrated that cyclic voltammetry, synchronized with localized surface plasmon resonance (LSPR) sensing, could be used to detect surface reactions on gold nanostructures electrically and optically using electrochemistry [88]. In this study, the gold nanoparticles were immobilized on an indium tin oxide (ITO) substrate, which served as the working electrode. Optical signals that were linear with the applied potential were detected in the capacitive charging regime. During reduction, gold was partially redeposited and dissolved above the oxidation potential, which changed the size and conformation of gold nanoparticles. Fig. 19 shows kinetic peak shift plots after stepwise potential application at different salt concentrations. In kinetic measurements, lower salt concentrations resulted in a slower potential establishment. Simulations using the multiple multipole program (MMP) suggested the formation of a lossy layer by combining charge depletion of gold and negative ion adsorption even below the reaction potential.

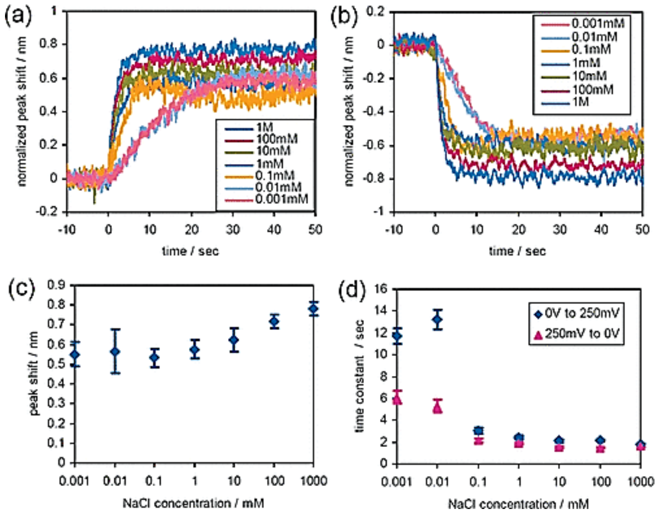

Fig. 19. Kinetic peak shift plots after stepwise potential application at different salt concentrations: (a) Potential applied from 0 to 250 mV, and (b) from 250 to 0 V at time *t* = 0. To eliminate variations due to different samples and positions, the magnitudes are normalized to the measurement at 1 M concentration which was recorded at the same spot. (c) Peak shift plot at saturation, and (d) time constant plot for potential applications from 250 mV to 0 V and 0 V to 250 mV as functions of concentration. Reproduced with permission [88].

2.5 Hot (Energetic) Charge Carriers

Hot (energetic) charge carriers (HCs) refer to either photoexcited holes or electrons that exist in non-equilibrium high-kinetic energy states in photoactive materials after being exposed to photons [89,90]. Photoexcited, non-equilibrium hot carriers in metallic nanostructures could lead to bandgap-free photodetection and selective photocatalysis [91]. However, hot carrier devices must be significantly improved to meet practical application requirements. A promising pathway for increasing the efficiency of these systems is the excitation of surface plasmon polaritons [91].

The energy in an SPP is dissipated as free-space radiation (radiative loss) or as absorption (nonradiative decay). The nonradiative decay of SPPs produces highly energetic carriers (both electrons and holes) in the metal that are not in thermal equilibrium with the lattice. These non-equilibrium hot carriers enable efficient energy-harvesting applications, in technologies ranging from photovoltaics, photodetection, to photon up-conversion and photocatalysis [89,90,92].

Recent attention has focused on studying the role played by energetic carriers created by SPP absorption in electrochemical reactions [93]. However, the underlying mechanisms of hot carrier transfer in photochemical processes remain a mystery, particularly for those involving hot holes. Using photoelectrochemistry, hot holes and hot electrons can be localized on photoanodes and photocathodes, allowing analysis of the hole-transfer and electron-transfer dynamics separately.

Electrodes in general electrochemical setups are classified as anodes (oxidation reactions) and cathodes (reduction reactions), which are also applicable to plasmonic photoelectrodes. The structures and working principles of photoanodes (metal nanoparticle or metal/n-type semiconductor) and photocathodes (metal/p-type semiconductor) are explained as they are used repeatedly in the literature [93]. Heterostructures as metal on an n-type semiconductor have been extensively investigated as photoanodes in plasmonic photocatalysis. For n-type semiconductors, Fermi levels are near the conduction band (CB). When semiconductors come into contact with metals, they donate electrons to the metal to equalize Fermi levels. An upward band bending occurs at metal/semiconductor interfaces (called a "Schottky barrier"). When hot electrons generated by plasmas have sufficient energy, they can overcome the Schottky barrier and reach the CB of semiconductors; however, due to upward band bending, they are rapidly swept away from interfaces (Fig. 20). As electrons travel along the external circuit, they eventually accumulate at the counter electrode to participate in reduction reactions (*e.g.*, water reduction, Fig. 20(a)). Hot holes are left on metal surfaces to drive oxidation reactions (*e.g.*, water oxidation, Fig. 20(a)). This results in an anodic photocurrent on the working electrode [93].

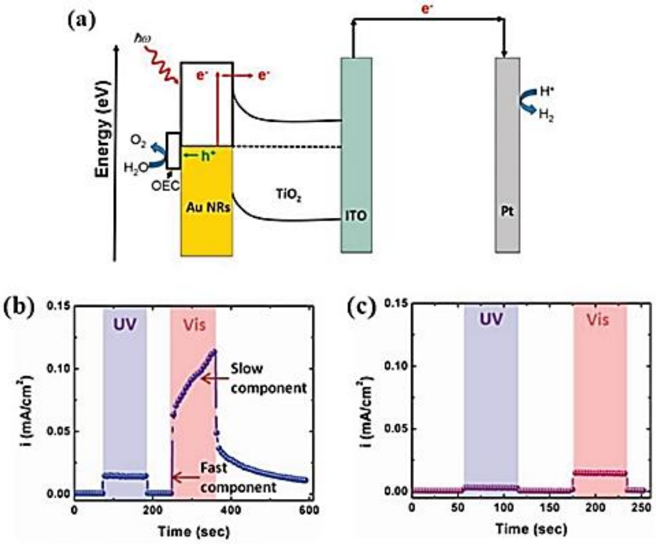

Fig. 20. Oxidation of water using a plasmonic metal/n-type semiconductor photoanode. a) Diagram of the energy band of an Au/TiO_2 photoanode. Au generates electron-hole pairs under visible light excitation. Hot electrons are injected into TiO_2, and hot holes are extracted by Co-based oxygen evolution catalyst (Co-OEC) on Au to facilitate water oxidation. Plots of photocurrent versus time for b) Au/$\mathrm{TiO_2}$ with and c) without Co-OEC irradiation. Reproduced with permission [93].

The potentiostat controls electron transfer in this scenario. The magnitude of the photocurrent is determined by the kinetics of hot-hole-driven photochemical reactions on the working electrode. A high anodic photocurrent results from water oxidation on photoanodes because the slow kinetics of water oxidation are incompatible with the short lifetimes of the hot holes.

The use of plasmonic photocatalysts as photocathodes is less reported than that of photoanodes. Photocathodes consist of metal/p-type semiconductor heterostructures, on which plasmon-generated hot holes are captured by p-type semiconductors and electrons are confined within metal NPs for driving reduction reactions (Fig. 21(a)). For a highly active photocathode, semiconductors must be able to collect hot holes efficiently. In theory, photo-excited holes above the interband threshold are considerably hotter than their electron counterparts for Au, which implies a greater collecting efficiency of hot holes than hot electrons for similar Schottky barrier heights in the optical range [93]. However, due to the relatively short mean free path of hot holes and the lack of p-type semiconductors with wide band gaps, harvesting hot holes from plasmonic metals remains challenging. Gallium nitride (p-GaN) has recently been used as semiconductor support in plasmonic photocathodes. In Au/p-GaN heterostructures, Au nanoparticles introduced holes into p-GaN's valence band (VB) and the adaptive Schottky barrier prevented holes from returning to Au. During plasmon-driven CO_2 reduction, electrons trapped on Au contributed to the cathodic photocurrent (Fig. 21(b)). There have also been recent reports of photocathodes containing nanostructured metals (*e.g.*, Au and Ag) for catalyzing reduction reactions (*e.g.*, hydrogen evolution, CO_2 reduction, and NO_3 reduction). Electron-hole separation on the pure metal NP electrodes remains a major issue without the above-mentioned p-type semiconductor as a hole-trapping mediator. Even under intense illumination, most previously reported photocurrent responses on metal NP photocathodes were still low. The development of molecular electron/hole trapping mediators would enable a decent charge separation for driving photochemical reactions effectively [93].

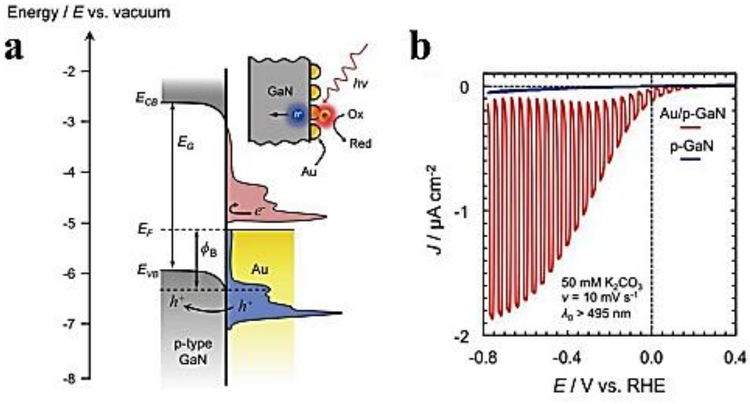

Fig. 21. A plasmonic metal/semiconductor photocathode. a) Energy band diagram of Au/p-GaN photocathode, depicting E_{VB}, E_{CB}, E_G, E_F, and $\emptyset_B$. Plasmon excitation generated hot electrons (red) and hot holes (blue) above and below EF of Au, respectively. Only those hot holes with energies larger than $\emptyset_B$ are able to surmount interfacial barrier and populate available VB levels of p-GaN. b) Linear sweep voltammetry (LSV) of Au/p-GaN (red) and bare p-GaN (blue) photocathodes. Reproduced with permission [93].

Some discussions are mainly focused on photoelectrochemical (PEC) measurements on photoanodes [93]. Under open-circuit conditions, both hot-hole and hot-electron transfers contribute to the photovoltage generation on plasmonic electrodes. Because electron transfer is controlled by the potentiostat under closed-circuit conditions, hole transfer and accumulation on electrode surfaces dominate reaction rates and mechanisms. When the distinct roles of hot holes and hot electrons are verified, physical locations of active sites and the energetics of hot carriers can be determined from PEC measurements. The clarified working principles are expected to benefit mechanistic research of hot-carrier transfer in plasmonic photocatalysis. Finally, the photothermal effect should be carefully considered in plasmon-driven photochemical reactions [93].

On the other hand, by creating energetic carriers through SPP absorption, metal temperatures always rise, with heat diffusing into the nearby reaction volume. Due to the temperature dependence of chemical reactions, separating the roles of temperature and energetic carriers is not trivial yet essential to provide an understanding of results [94-98]. An analytical and experimental investigation of the thermal effects on the electrochemical response of electrodes decorated with plasmonic nanostructures under illumination is presented in reference [99]. In terms of time-dependent temperature profiles in the vicinity of illuminated electrodes, a straightforward approach is taken that considers heat flow via conduction away from a planar electrode solution interface, yielding analytical expressions for the temperature profile in the system and subsequent increases in electrochemical rate because of enhanced diffusion [99].

Fig. 22 illustrates the distribution of velocity and temperature in the system consistsing of a cylindrical glassy carbon electrode surrounded by an insulating sheath immersed in a cylindrical electrochemical cell containing an aqueous electrolyte when a power input of $10\ \mathrm{W\ cm}^{-2}$ is applied over 10 seconds. Local heat input at the electrode surface results in significant solution flows that run initially vertically from the electrode edge, dissipating and changing direction further into the solution. Convective flows have the effect of lowering the temperature increase at the electrode surface by a factor of ∼2 as they serve as a mechanism for transferring heat away from the electrode surface [99].

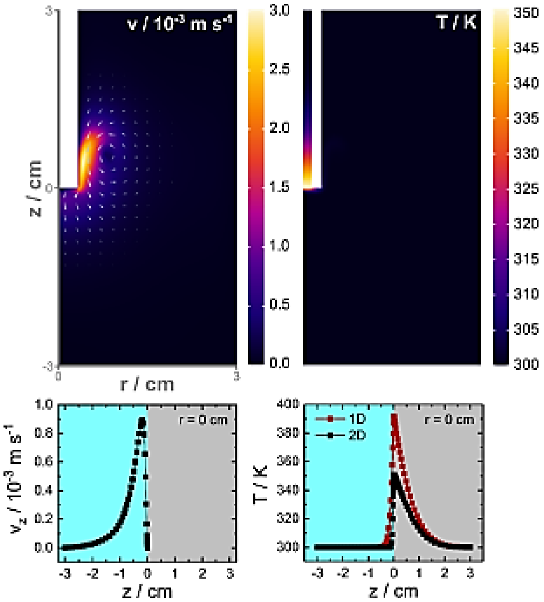

Fig. 22. Example velocity (left) and temperature (right) profiles in an electrochemical cell. The results of finite element simulations of heat transfer including both conduction and convection for a 1.5 mm radius glassy carbon electrode in water with a 10 $W\ cm^{-2}$ heat input at the surface. Magnitude and temperature data are encoded using color maps, and values are given 10 seconds after the onset of heating. In the bottom panels are the vertical profiles of the *z*-component of solution velocity, v_z, and temperature. The red curve on the bottom right panel shows the temperature profile computed in 1D ignoring convection. Reproduced with permission [99].

There is a correlation between heating and mass transfer in electrochemical systems. Increasing local temperatures would affect electrochemical reaction rates through

enhancements in mass transfer, an increase in heterogeneous electron transfer rates, and shifts in reduction potentials. In an electrochemical experiment, heat will alter the mass transfer-limited current observed in two ways, by altering the diffusion coefficient for the redox-active species, and by creating significant solution velocities via convection.
As predicted by the straightforward theoretical analyses of these systems in this work [99], which are based only on fundamental equations governing heat transfer via conduction and convection, light absorption at electrode surfaces produces significant local temperature increases and solution flows. According to this analysis, mass transfer enhancements alone would result in significant current increases, and these increases would apply to any electrochemical reaction involving dissolved reactants and/or products.

Models of diffusion, convection, and mass transport predict that redox currents increase approximately linearly with heating power rather than exponentially (as might be expected from the Arrhenius law) and that the current rises within 10 seconds of heating. Temperature trends are not straightforward, so electrochemical cells should be stabilized, electrode temperatures monitored, independent thermal control experiments conducted, and optical variables besides intensity should be varied to separate the effects of temperature from those of energetic carriers.

Plasmonic catalysis is interesting for opening new reaction pathways that are not possible thermally. Up to now, most plasmonic catalysis research has involved colloidal arrangements of Au nanoparticles illuminated at visible wavelengths. This scenario, however, poses certain challenges: The temperature near nanoparticles is often difficult to predict and measure because of collective effects [96]. Furthermore, carriers excited by wavelengths above the interband threshold ($h\upsilon$ ~ 2 eV) have very short lifetimes (due to electron-electron scattering at high carrier energies) [100].

Chapter 3.

Grating couplers for LRSPP Waveguides in Fluoropolymer

3.1. Summary

Au stripe waveguides embedded in Cytop with grating couplers are demonstrated and analyzed. The grating couplers are used for a broadside coupling scheme, which involves a laser beam incident on a stripe of Au in Cytop. The use of gratings for excitation of LRSPPs simplifies optical alignment and eliminates the need for high-quality input and output edge facets. An optical experiment is performed on cleaved bow-tie PM fibers and lensed PM fibers to demonstrate coupling loss and determine coupling efficiency. An aligned bow-tie PM fiber had input coupling losses of about 20 dB, while an aligned lensed PM fiber had input coupling losses of about 9 dB. Additionally, both types of fibers are characterised for their coupling loss and grating coupling efficiency. Both measurements and theory agree well with each other. Despite the samples being designed to work at 1310 nm, the minimum coupling loss was found at around 1345 nm. According to AFM images obtained on an etched grating coupler, the fabricated structures have a slight out-of-plane curvature, possibly induced during fabrication (e-beam exposure), explaining the observed shift and slight increase in coupling losses.

3.2. Contribution

The results provided in this chapter are published in Applied Optics. Zohreh Hirbodvash designed the experiments and carried out the experimental work. Maryam Khodami did the theoretical calculation using COMSOL. Biosensor chips used in this series of experiments were fabricated by Norman Fong, E. Lisicka-Skrzek, A. Olivieri, and H. Northfield, former or current member of our group. Zohreh Hirbodvash interpreted the results and wrote the manuscript. Dr. Berini contributed to the interpretation of the results and revised the manuscript.

3.3. Article

The article follows here verbatim.

2994 Vol. 58, No. 11 / 10 April 2019 / *Applied Optics* **Research Article**

applied optics

Grating couplers fabricated by e-beam lithography for long-range surface plasmon waveguides embedded in a fluoropolymer

ZOHREH HIRBOODVASH,[1,2,*] MARYAM KHODAMI,[2,3] NORMAN R. FONG,[4] EWA LISICKA-SKRZEK,[2] ANTHONY OLIVIERI,[2] HOWARD NORTHFIELD,[2] R. NIALL TAIT,[5] AND PIERRE BERINI[1,2,3]

[1]Department of Physics, University of Ottawa, Ottawa, Ontario K1N 6N5, Canada
[2]Center for Research in Photonics, University of Ottawa, Ottawa, Ontario K1N 6N5, Canada
[3]School of Electrical Engineering, University of Ottawa, Ottawa, Ontario K1N 6N5, Canada
[4]National Research Council Canada, Ottawa, Ontario K1A 0R6, Canada
[5]Department of Electronics, Carleton University, Ottawa, Ontario K1S 5B6, Canada
**Corresponding author:* [redacted]

Received 8 January 2019; revised 15 March 2019; accepted 15 March 2019; posted 18 March 2019 (Doc. ID 356550); published 10 April 2019

Long-range surface plasmon polariton waveguides consisting of Au stripes integrated with input and output grating couplers embedded in thick Cytop claddings are proposed and demonstrated experimentally. Under the right conditions, grating couplers enable broadside (top) coupling with good efficiency while producing a low level of background light. The scheme does not require high-quality input and output edge facets, and it simplifies optical alignments. We demonstrate coupling using a cleaved bow-tie fiber and a lensed fiber, and we determine the grating coupling efficiencies in both cases over a broad operating wavelength range. The lensed fiber produces a better overlap with the long-range surface plasmon mode of interest and thus results in a better coupling efficiency with essentially no background light as observed on an infrared camera. The measurements are compared with theoretical results obtained using a realistic model of the structures, including out-of-plane curvature in the grating profile resulting from our fabrication process. The coupling scheme along with the surface plasmon waveguides hold strong potential for biosensing applications.

https://doi.org/10.1364/AO.58.002994

1. INTRODUCTION

Single-interface surface plasmon polaritons (SPPs) are electromagnetic surface waves propagating at the interface of a dielectric and a metal at optical wavelengths [1]. They are characterized by high surface and bulk sensitivities, an energy asymptote in their dispersion curve, and sub-wavelength confinement near their energy asymptote. The high surface sensitivity of SPPs has motivated their use in biosensors.

Biosensors are analytical devices that use biochemical reactions to selectively detect a target analyte [2]. Biosensors combine an immobilized biologically active receptor with a physical signal transducer and ancillary (opto-)electronic components [3]. There are many different types of biosensors depending on the underlying transducer technology, including electrochemical, piezoelectric, thermal, and optical biosensors [2,3]. There are different types of optical biosensors based on, e.g., optrode fiber optics, evanescent-wave waveguides, flow immunosensors [4], and surface plasmon resonance (SPR) [5].

SPR-based devices are among the most efficient and practical, and they are among the most advanced label-free biosensors available [5]. Conventional SPR biosensors are based on the measurement of changes in the coupling characteristics of single-interface SPPs to an incident optical beam arising from changes in the effective refractive index as biomaterial binds to the surface [5]. Prism coupling has been employed extensively in SPR biosensors to excite single-interface SPPs at the metal–liquid interface [1]. This approach has been applied to a large number of biodetection problems, including, e.g., biosensing of pesticides [6], dual-parameter biosensing [7], protein biosensing [8], the detection of foodborne pathogens [9], Bovine Serum Albumin (BSA) [10], cardiac troponin [11], Benzo[a]pyrene (BaP) [12], and pituitary hormones [13].

Single-interface SPPs have high propagation losses due to absorption of light in the metal, which limits sensing performance and the architectures available for the implementation of transducers. Alternatively, long-range SPPs (LRSPPs) have a much lower attenuation. LRSPPs are surface waves propagating along a thin metal slab or stripe bounded by dielectrics of similar refractive index [14]. They have a lower surface sensitivity, but this can be more than compensated for by the long optical interaction with the sensing medium made possible by the lower attenuation. In a biosensing application using

1559-128X/19/112994-09 Journal © 2019 Optical Society of America

LRSPPs, the choice of cladding material depends on the bulk refractive index of the target sensing fluid. Most sensing fluids in biosensor applications are aqueous in nature, e.g., clean buffers carrying analyte or patient samples (urine, blood) diluted in buffer. Thus, the choice of cladding should be limited to materials that have a refractive index close to water, such as Cytop [15] and Teflon [16]. LRSPPs on a thin metal slab (of optically infinite extent) and excited in a prism-coupling configuration similar to conventional SPR have been exploited for bulk sensing [17] to investigate the effects of toxins on HEK-293 cells [18], to monitor cellular micro-motion within fibroblast cells [19], and for the detection of E. coli bacteria [20].

LRSPPs on a thin metal stripe (of limited width) retain the benefit of low attenuation but are additionally confined in the plane transverse to the direction of propagation, thereby enabling integrated optical structures [14]. Thin metal stripes lead naturally to straight waveguide LRSPP biosensors, specifically, as a thin Au stripe embedded in Cytop integrated with etched microfluidic channels [21–23]. In these structures, the LRSPPs are excited via butt coupling to an optical fiber, leading to high coupling efficiency and a compact sensing arrangement [22,23]. This approach has been used in various biodetection experiments, including the detection of Dengue infection in patient blood plasma [24,25], the selective detection of human red blood cells for blood-typing applications [26], the detection of leukemia markers in patient serum [27], the extraction of binding kinetics of an immunological pair [28], and achieving high-sensitivity detection using enhanced assays [29].

Butt coupling requires high-quality optical facets, implying that diced chips may require polishing post-dicing. Rough facets reduce the coupling efficiency and produce scattering in the forward direction, which can compete with the sensing mode in the form of background light. This issue motivates the use of other coupling techniques, such as phase-selective coupling by integration of grating couplers. This approach has been implemented with metal stripes on thin free-standing membranes for LRSPP gas-sensing applications [30] and with metal stripes on a truncated photonic crystal to excite Bloch-LRSPPs [31]. Grating coupling is advantageous in that easier broadside optical alignments are enabled, high-quality end facets are not required, and uncoupled light propagates orthogonally to the sensing wave. Drawbacks are that coupling efficiencies are generally lower compared to butt coupling, and high-resolution lithography may be required to define the gratings.

In this paper, we propose, fabricate, and characterize LRSPP Au stripe waveguides integrated with Au grating couplers embedded in Cytop, anticipating application to biosensors. This paper differs from [30] and [32] in that the latter describes waveguide structures on a freestanding membrane intended for gas-sensing applications (no fluids) that are fabricated using a different process, and it differs from [31], where the structures operate with Bloch LRSPPs, which are very different modes. First, we briefly describe the fabrication process flow. Then, we present the experimental results obtained and compare them with theory. A brief conclusion closes the paper.

2. DEVICE STRUCTURE AND FABRICATION PROCESS FLOW

A. Device Structure

Figure 1 shows the structure of interest, consisting of an Au stripe waveguide of target width 5 μm and thickness 35 nm bearing a grating coupler, along with the proposed excitation scheme, shown here as an aligned optical fiber launching *p*-polarized light (alternatively an aligned and focused *p*-polarized optical beam—not shown). *L*, *D*, and *C* represent the length of the waveguide from the input grating coupler to the end facet, the distance between the fiber end facet and the grating, and the width of the grating ridges ($C = 4$ μm), which is narrower than the width of the Au stripe (5 μm). A longitudinal cross-sectional sketch of the structure is shown in Fig. 2. The grating design consists of 20 rectangular ridges of target width $W = 450$ nm and height $H = 100$ nm disposed in a period of $\Lambda = 1000$ nm (first order). These dimensions were selected for good broadside (perpendicularly incident) coupling to the LRSPP of the stripe at the free-space wavelength of $\lambda_0 = 1310$ nm. Grating couplers must be designed to satisfy the momentum conservation condition [33]

$$\Lambda = m\lambda_0(n_{\mathrm{eff},a} - n_c \sin\theta), \qquad (1)$$

where m is the (integer) order of the grating, $n_{\mathrm{eff},a}$ is the average effective index of the LRSPP mode propagating along the waveguide with the grating, λ_0 is the free-space operating wavelength

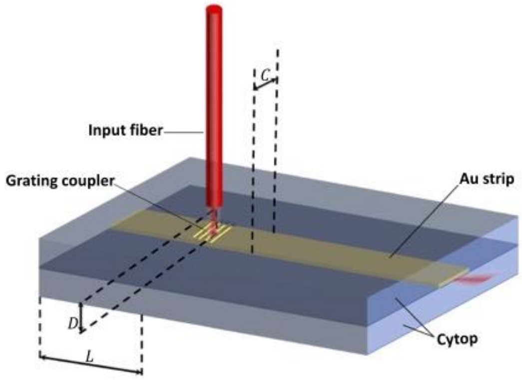

Fig. 1. 3D sketch (not to scale) of the structure of interest, consisting of an Au stripe waveguide integrated with a grating coupler in Cytop, along with the excitation scheme.

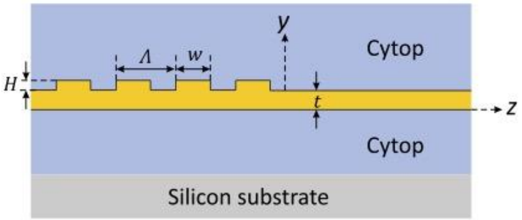

Fig. 2. Longitudinal cross-sectional sketch of the structure.

(1310 nm), n_c is the refractive index of the medium from which the beam is incident (Cytop in this case, $n_c = 1.3348$ [15]), and θ is the angle of incidence. Here we set $\theta = 0°$ for broadside excitation, and we choose $m = 1$ for the lowest grating order.

B. Fabrication Process Flow

An overview of the fabrication process flow is depicted in Fig. 3. The structure is supported by a Si substrate. A layer of 5% Cytop [M-grade] followed by five layers of 9% Cytop [S-grade] were spin-coated on the Si wafer at 1500 and 1000 RPM, respectively. Then, a layer of 5% M-grade was coated on the stack to complete the lower cladding. A 30 min soft-bake time was applied at 70°C after spinning each layer. The full stack was ramped to 200°C at 10°C per hour and baked for 20 h. This process produces a seamless 8 μm thick Cytop lower cladding.

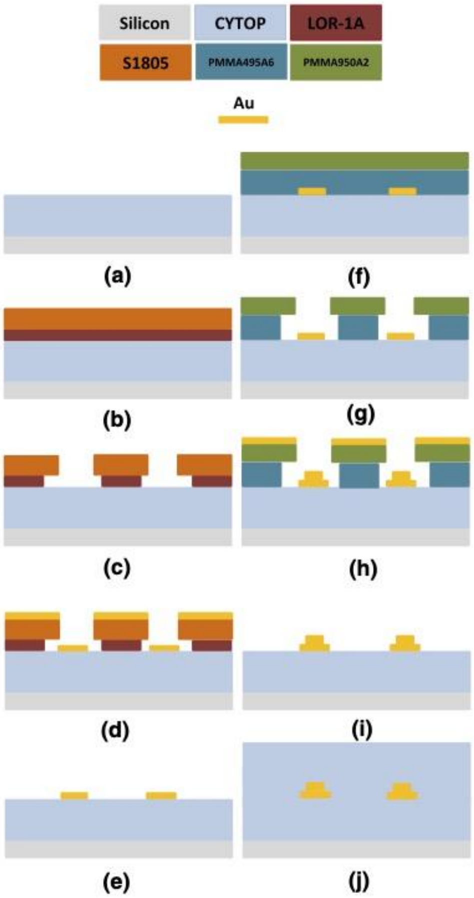

Fig. 3. (a) Cytop coating; (b) bilayer photoresist deposition; (c) UV exposure and development of photoresist to define waveguides; (d) Au deposition by thermal evaporation; (e) lift-off to form Au waveguides; (f) bilayer e-beam resist deposition; (g) electron-beam pattering of resist to define gratings; (h) Au deposition by e-beam evaporation; (i) lift-off to form gratings; (j) Cytop coating.

A bilayer lift-off process comprising LOR1A lift-off resist and S1805 photoresist was used to define the waveguides on the Cytop substrate by contact photolithography. A 1 min O_2 plasma descum was performed before thermal evaporation of Au (35 nm). Au lift-off was then achieved via soaking in two baths of Microposit 1165, each for a duration of 10 min at 80°C. 10s ultrasonic agitation was applied between the baths, which were then followed by baths in isopropyl alcohol (IPA) and deionized (DI) water, each for 10 min, as the final lift-off steps.

A bilayer lift-off process, comprising PMMA 495A6 ($\approx$300 nm) and PMMA 950A2 ($\approx$90 nm), was used to define gratings on Au stripes via e-beam exposure (Raith Pioneer 30 kV system). A charge dissipation layer was spin-coated on the sample prior to e-beam exposure (ESpacer). Once the e-beam exposure was completed, a DI water rinse was applied to remove the e-spacer, and the sample was developed in a 1:3 solution of methyl isobutyl ketone (MIBK) and IPA for 120 s at room temperature. A 20 s plasma reactive ion etching (RIE) O_2 descum was performed before the thermal evaporation of Au at a thickness of 100 nm. Lift-off was then accomplished by a static overnight acetone bath at room temperature.

The Cytop upper cladding ($\approx$8 μm) was deposited using a similar recipe applied for the lower cladding, except that longer lower temperature bakes were applied in order to not damage the embedded Au features.

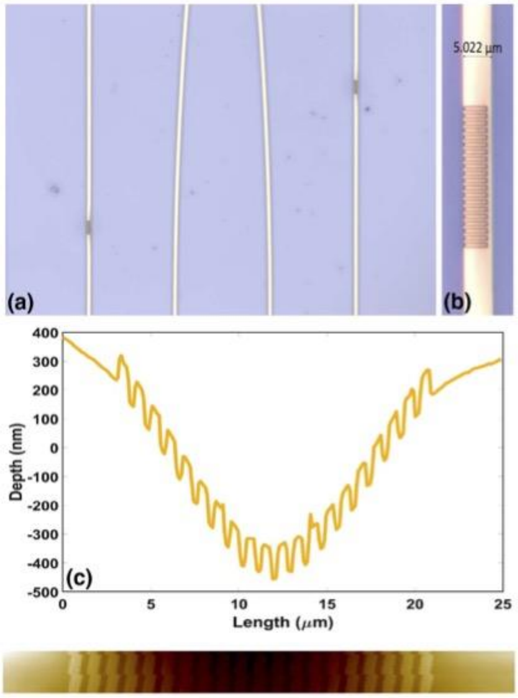

Fig. 4. (a) Low-magnification optical microscope image of grating couplers on Au stripes in Cytop. (b) High-magnification optical microscope image of a 5 μm wide Au stripe bearing a grating coupler embedded in Cytop. (c) Atomic force microscope (AFM) image of a grating coupler on an Au stripe, post-etching of the top Cytop cladding.

Wafers were segmented into rectangular die using a dicing saw. Dies were cleaned and used as is without end facet polishing (only to observe mode outputs). Figure 4 shows two microscope images of the diced samples. Figure 4(a) is a low-magnification image of two gold stripes bearing grating couplers embedded in Cytop. As is evident from the image, the gratings are placed at different locations from the output edge to facilitate cutback measurements. The Au stripes are separated from each other in order to avoid crosstalk. Figure 4(b) shows a high-magnification image of a grating coupler. Ideally, the grating ridges should be centered on the stripe; a slight misalignment to the left is apparent. Figure 4(c) shows an atomic force microscope (AFM) image of an Au stripe bearing a grating coupler. The AFM image was obtained by first etching away the upper cladding of Cytop from a die using an O_2 RIE process. The AFM scan reveals a height of $H = 100$ nm, a pitch of 900 nm, and a roughness of 1.6 nm RMS on top of the grating ridges. The grating was expected to be flat (Fig. 2); however, Fig. 4(c) reveals that it rests on a slightly curved (out-of-plane) surface, and a curvature of about 800 nm over a length of about 25 μm is observed. This curvature is believed to have been created during e-beam exposure of the PMMA bilayer. The curvature is reproducible as long as the e-beam parameters are controlled. All of the gratings observed under optical microscope on our test wafer had a curvature, and the cutback measurements discussed below suggest that the gratings are very similar (a very high R^2 goodness of fit was achieved for all linear models).

3. EXPERIMENTAL SETUP

A schematic diagram of the experimental arrangement is sketched in Fig. 5. The setup consists of a tunable laser connected to an optical fiber aligned perpendicularly to an input grating coupler. The light output from an LRSPP waveguide is first collimated by an objective lens. After passing through the aperture, the beam is split by a 50:50 beam splitter. One beam is then captured by an optical power meter, and the other is captured by an IR camera. As shown in Fig. 5, a 90° metallic holder was used to mount the fiber. The experiment was conducted with two different types of optical fiber. First, a cleaved bow-tie style polarization-maintaining (PM) optical fiber with a 6.6 μm core diameter was aligned to the input grating coupler. Second, a lensed PM fiber producing an output beam 4 μm in diameter at a working distance of 1 mm was used. The LRSPP mode supported by the Au stripe is approximately 5 μm in diameter, so a 4 μm diameter beam leads to a high overlap. Thus, the lensed fiber is expected to produce a higher coupling efficiency in this system than the cleaved fiber.

Figure 6 plots the results obtained using the bow-tie PM fiber. Figure 6(a) shows the insertion loss response for different lengths of waveguide L, determined as the distance between the input grating and the output facet. The effects of the setup were removed by calibration. As is obvious from the figure, the insertion loss increases with the waveguide length. The grating

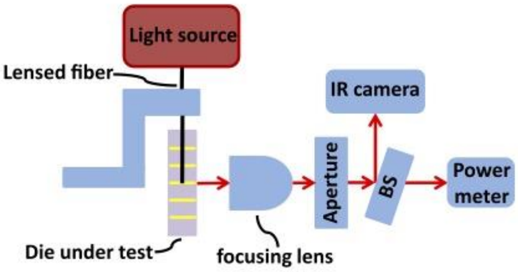

Fig. 5. Schematic diagram of the experimental setup.

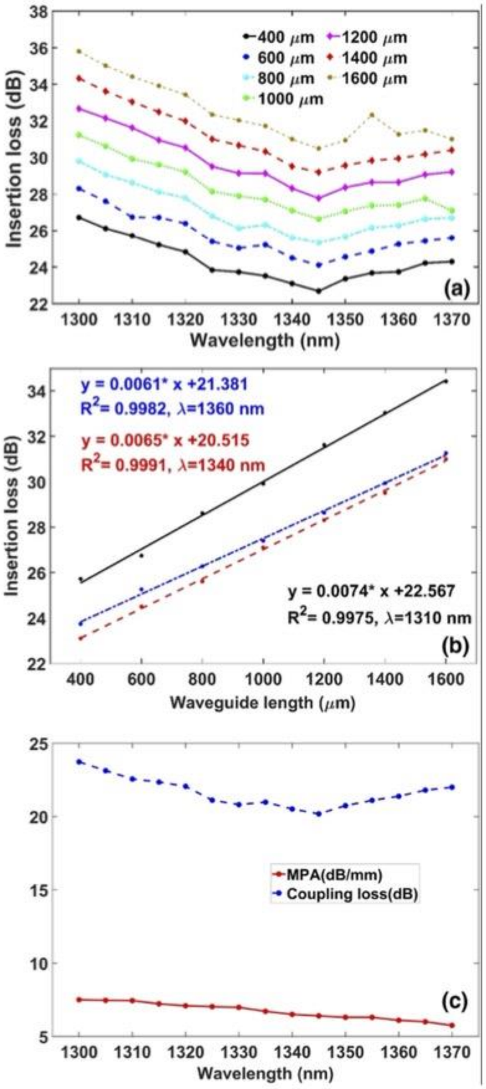

Fig. 6. (a) Insertion loss response of Au stripe waveguides of different lengths (see legend), each bearing an identical input grating coupler, excited with an aligned cleaved PM fiber; (b) cutback plots formed from the wavelength responses; (c) mode power attenuation and coupling loss obtained from the cutback plots.

couplers were designed to operate at $\lambda_0 = 1310$ nm; however, the minimum insertion loss in all cases occurs near $\lambda_0 = 1345$ nm. The target design of the gratings was $W = 450$ nm, $H = 100$ nm, and $\Lambda = 1000$ nm on a flat surface, but in the experimental case the dimensions achieved are $W = 444$ nm, $H = 100$ nm, and $\Lambda = 918$ nm, and the gratings are on a curved surface. These differences due to fabrication imperfections explain the shift in optimal coupling wavelength, as discussed further below in the theoretical section.

Figure 6(b) shows three typical curves obtained using the cutback technique from the wavelength responses of Fig. 6(a) at $\lambda_0 = 1310$ nm, $\lambda_0 = 1340$ nm, and $\lambda_0 = 1360$ nm. Here the insertion loss is plotted as function of waveguide length, and a linear model is fit to the results to determine the mode power attenuation (MPA—slope) and the total coupling losses (intercept). The coupling loss of the input grating coupler is taken as the total coupling loss because the LRSPP is allowed to emerge freely from the output facet of the die (which is of high quality) and Cytop–air Fresnel losses are negligible. The goodness of fit is high in all cases ($R^2 \approx 0.99$), suggesting that the waveguides and grating couplers are very similar to each other across the samples tested.

Figure 6(c) summarizes the MPA and the input grating coupling loss obtained at all wavelengths considered. As expected, the grating coupling loss first decreases, then increases with wavelength. However, the MPA simply decreases monotonically with wavelength, also as expected [14]. The measured MPA of about 7 dB/mm is in agreement with theoretical expectations, but the best input grating coupling loss of 21 dB is high.

Figure 7 shows the mode outputs emerging from the waveguide of length 800 μm (through its polished end facet) at several free-space wavelengths. The waveguide was excited via the input grating coupler using an aligned cleaved fiber (bowtie fiber, as in Fig. 6). The images reveal a strongly guided mode along with significant background light guided by the Cytop slab. Here, the mode emerging form the cleaved fiber spreads as a Gaussian beam propagating over a distance $D \approx 200$ μm to the grating. Thus, the spot size intersecting the grating is about 25 μm in diameter, which is significantly larger than the grating width ($C = 4$ μm) and LRSPP mode size on the Au stripe (≈5 μm). Thus, a significant portion of the incident beam scatters into slab modes (background light).

Figure 8 gives the results obtained using the lensed PM fiber to excite the input grating couplers. Figure 8(a) plots the insertion loss response for different waveguide lengths L. Comparing Figs. 6(a) and 8(a) reveals similar wavelength responses but insertion loss levels that are much lower in the latter. Two lengths of waveguide, 400 μm and 600 μm, are missing from our measurements with the lensed fiber due to mechanical issues—the lens assembly on the fiber is thick, precluding characterization of these short waveguides.

Figure 8(b) gives a few corresponding cutback curves for the three lengths of stripe waveguide given in the legend, and Fig. 8(c) summarizes the MPA and coupling loss values obtained at all wavelengths considered. The measured MPAs (slopes) work out to about 7 dB/mm, which is similar to that reported in Fig. 6(c), as expected, but the coupling loss values are significantly lower in the present case, near 9 dB in the best case. Comparing Figs. 6(c) and 8(c) reveals a 11 dB improvement in coupling loss because of better overlap between the incident beam and the LRSPP. In general, the coupling loss can be decreased by improving the overlap between the incident beam and the waveguide mode to be excited [34–36]; further improvements can be expected as designs are optimized in this regard. Furthermore, in our experiments, the grating coupler splits the incident beam in half with each portion propagating in opposite directions, but the output is taken from one facet only. Unidirectional grating couplers could address this problem by increasing the coupling efficiency in one direction. There are different approaches to the design of unidirectional

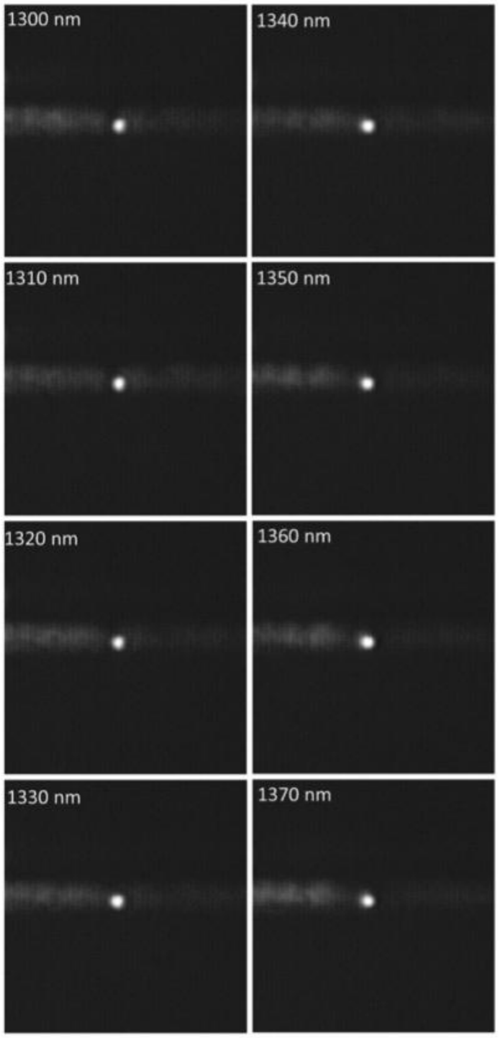

Fig. 7. Mode outputs emerging from the waveguide 800 μm in length, captured using the infrared camera at the free-space wavelengths indicated on each image. Excitation using a cleaved PM fiber aligned to the input grating coupler.

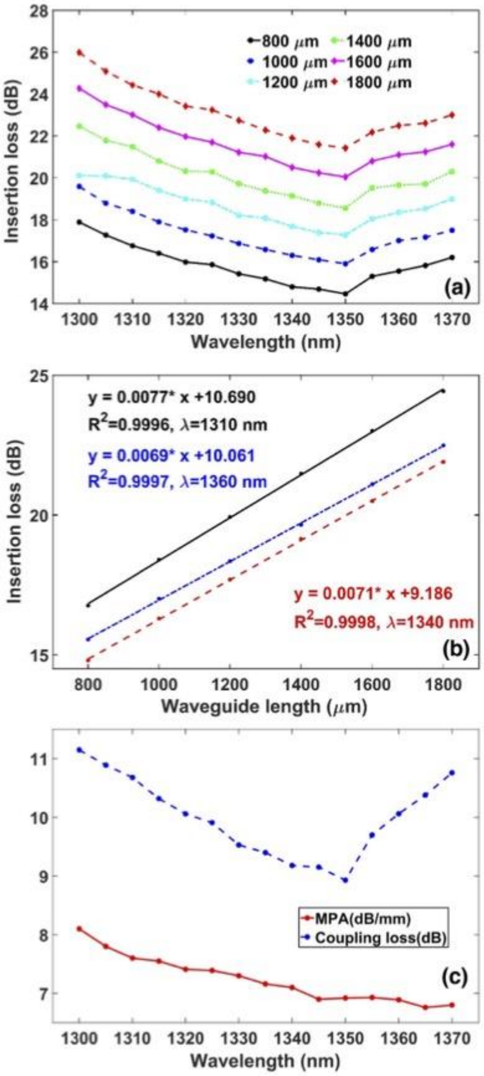

Fig. 8. (a) Insertion loss response of Au stripe waveguides of different lengths (see legend), each bearing an identical input grating coupler, excited with an aligned lensed PM fiber; (b) cutback plots formed from the wavelength responses; (c) mode power attenuation and coupling loss obtained from the cutback plots.

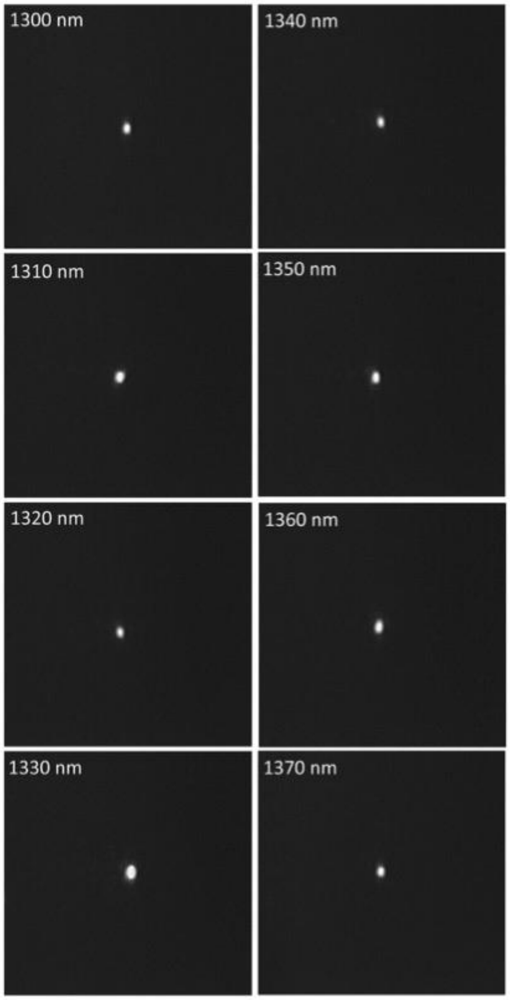

Fig. 9. Mode outputs emerging from the waveguide 800 μm in length, captured using the infrared camera at the free-space wavelengths indicated on each image. Excitation using a lensed PM fiber aligned to the input grating coupler.

grating couplers such as using slanted lamellar or sinusoidal gratings [37], blazed gratings [38], or introducing subwavelength features in the direction perpendicular to the grating period [39]. In such cases, the grating symmetry is broken, leading to coupling in a preferred direction.

Figure 9 shows a mosaic of outputs emerging from the 800 μm long stripe waveguide, captured at different wavelengths using an infrared camera, with its input grating coupler excited with the lensed PM fiber. Comparing Figs. 9 and 7 reveals that excitation with the lensed fiber leads to essentially no background light. Indeed, in this case the coupling efficiency to the LRSPP is significantly better because the incident beam is very well size matched. The lensed fiber produces a spot size that is 4 to 5 μm in diameter on the grating coupler, and the LRSPP mode guided by the Au stripe is of comparable diameter. Thus, coupling to slab modes can be minimized by altering and optimizing the grating design to completely match the illuminating beam to the guided mode of interest (or vice versa).

Figure 10 summarizes the measured coupling efficiency obtained using the cleaved fiber and lensed fibers to ease comparisons with modelling in the next section. The coupling

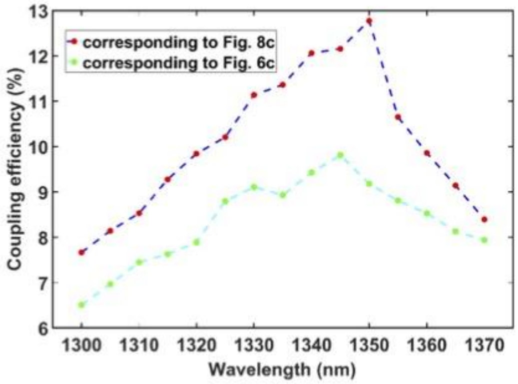

Fig. 10. Coupling efficiency corresponding to the coupling losses summarized in Fig. 6(c) (cleaved fiber), and Fig. 8(c) (lensed fiber) (see legend).

loss C_{dB} is related to the coupling efficiency C as $C_{\mathrm{dB}} = -10\log_{10}|C|$ [21].

4. THEORETICAL

The structure of interest is composed of an Au strip embedded in Cytop, supporting LRSPPs with a grating coupler used as input means. We carry out two types of computations to model the performance of the experimental structures. The first is a 2D modal analysis of the waveguide cross section (x–y plane in Fig. 2) to determine the propagation characteristics of the LRSPP. The second is a 2D scattering computation, which consists of modeling a longitudinal cut along the length of the structure (y–z plane in Fig. 2) including the grating coupler to determine the input coupling efficiency. In both cases, the finite element method implemented in commercial code was used [40].

The refractive index of Cytop is set to 1.3348 [15] and that of the Au stripe and grating to $N_{\mathrm{au}} = 0.448 + i9.228$ at the free-space wavelength of 1310 nm. The size of the mesh was set to 5 nm inside the gold regions and 75 nm everywhere else, ensuring reasonably converged results.

The computed electric field distribution along the longitudinal cross section is shown in Fig. 11(a). Here a 1D Gaussian beam of waist diameter 4 μm was launched toward the grating from a position of 10 μm above at a slight offset of 7 μm toward the left edge of the grating [the rectangular outline in Fig. 11(a) shows the location of the source]. The dimensions of the grating coupler were selected as those used in the layout of the structure ($W = 450$ nm, $H = 100$ nm, $\Lambda = 1000$ nm). The grating successfully couples the incident beam to LRSPPs propagating along the z direction as expected, but a region of spatial transients is present near the grating due to diffraction into other directions. A zoom of the electric field magnitude near the grating coupler, as shown in Fig. 12, makes the diffraction evident. A Ey field cut taken about 200 μm away from the grating edge is plotted in Fig. 11(b), showing that the spatial transients have sufficiently decayed at this distance for the LRSPP mode field distribution to become evident.

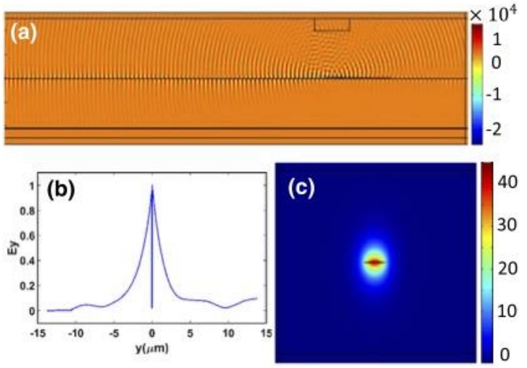

Fig. 11. (a) Longitudinal cross-sectional distribution of the computed field amplitude near the grating coupler and along the waveguide; (b) 1D field cut of the propagating LRSPP 200 μm away from the grating; (c) mode field distribution of the LRSPP guided by the Au stripe.

The LRSPP mode field distribution and its propagation constant were determined from the 2D modal analysis setting the stripe width to 5 μm and its thickness to 35 nm. The computed MPA is 6.76 dB/mm, which compares very well with the measured value of 7 dB/mm, and the field distribution obtained is shown in Fig. 11(c), comparing very well with the measured outputs of Fig. 9.

A longitudinal cross-sectional sketch of an out-of-plane curved grating coupler is illustrated in Fig. 13. A 1D Gaussian beam perpendicularly incident to the grating plane is modeled such that the size of the beam matches the experiment by setting the beam waist to 4 μm and 6.6 μm, respectively, to represent the beams emerging from the cleaved and lensed fibers. The associated coupling efficiency is calculated for both the nominal grating design ($W = 450$ nm, $H = 100$ nm, and $\Lambda = 1000$ nm) on a flat surface and the experimental grating ($W = 444$ nm, $H = 100$ nm, and $\Lambda = 918$ nm) on a curved surface, following the approach described in Ref. [41]. As AFM scans reveal [see Fig. 4(c)], the grating ridges rests on a curved

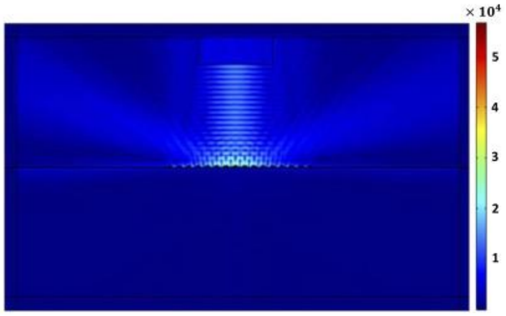

Fig. 12. Gaussian beam perpendicularly incident on a grating coupler embedded in Cytop, diffracting into two orders (+1, −1) and into LRSPPs propagating along the metal stripe.

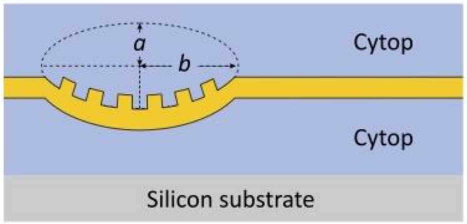

Fig. 13. Front cross-sectional sketch of curved grating couplers.

surface, believed to be created during e-beam exposure (possibly by heating and reflow of Cytop, which has a glass transition temperature of 108°C). This curvature is modelled as elliptical with major and minor axes of 8.5 μm and 0.6 μm, respectively, chosen to best represent the structure.

The curvature causes a drop in the coupling efficiency relative to the flat surface, as determined through modeling. We find for the nominal design, the peak of the coupling efficiency occurs at 1310 nm for the small beam size, while for the curved design the peak is shifted to around 1330 nm, which is in good agreement with the peak coupling efficiency observed experimentally, occurring near 1350 nm (Fig. 10).

5. SUMMARY AND CONCLUDING REMARKS

In conclusion, we proposed, fabricated, and demonstrated grating couplers for Au stripe waveguides embedded in Cytop as a means for input excitation. Input coupling losses of about 20 dB were measured using an aligned bow-tie PM fiber and of about 9 dB using an aligned lensed PM fiber. The measured coupling losses are in good agreement with theory. The samples were designed to work at 1310 nm; however, the minimum coupling loss was obtained at around 1345 nm. AFM images obtained on an etched grating coupler reveal that the fabricated structures have a slight out-of-plane curvature, possibly induced during fabrication (e-beam exposure), explaining the observed shift and slight increase in coupling losses as corroborated through modelling. Grating couplers simplify optical alignments and remove the need for high-quality end facets. Furthermore, uncoupled light propagates orthogonally to the excited waveguide mode and is thus less likely to cause interference with the output at detection opto-electronics.

REFERENCES

1. S. A. Maier, *Plasmonics: Fundamentals and Applications* (Springer, 2007).
2. A. Sadana, *Fractal Binding and Dissociation Kinetics for Different Biosensor Applications* (Elsevier, 2005).
3. F. Scheller and F. Schubert, *Biosensors: Techniques and Instrumentation in Analytical Chemistry* (Elsevier, 1992).
4. F. S. Ligler and C. R. Taitt, "Fluorescence lifetime biosensing: entering the mainstream," in *Optical Biosensors: Today and Tomorrow* (Elsevier Science, 2008), pp. 287.
5. A. Rasooly and K. E. Herold, *Biosensors and Biodetection* (Springer, 2009).
6. E. Mauriz, A. Calle, J. Manclus, A. Montoya, and L. M. Lechuga, "Multi-analyte SPR immunoassays for environmental biosensing of pesticides," Anal. Bioanal. Chem. **387**, 1449–1458 (2007).
7. D. M. Hernández, J. Velázquez-González, D. Luna-Moreno, M. Torres-Cisneros, and I. Hernández-Romano, "Prism-based surface plasmon resonance for dual-parameter sensing," IEEE Sens. J. **18**, 4030–4037 (2018).
8. R. Boruah, D. Mohanta, A. Choudhury, P. Nath, and G. A. Ahmed, "Surface plasmon resonance-based protein bio-sensing using a Kretschmann configured double prism arrangement," IEEE Sens. J. **15**, 6791–6796 (2015).
9. V. Koubova, E. Brynda, L. Karasova, J. Škvor, J. Homola, J. Dostalek, P. Tobiška, and J. Rošický, "Detection of foodborne pathogens using surface plasmon resonance biosensors," Sens. Actuators B **74**, 100–105 (2001).
10. W. Lee, D.-B. Lee, B.-K. Oh, W. H. Lee, and J.-W. Choi, "Nanoscale fabrication of protein A on self-assembled monolayer and its application to surface plasmon resonance immunosensor," Enzyme Microb. Technol. **35**, 678–682 (2004).
11. J. Wei, Y. Mu, D. Song, X. Fang, X. Liu, L. Bu, H. Zhang, G. Zhang, J. Ding, W. Wang, Y. Mu, D. Song, X. Fang, X. Liu, L. Bu, H. Zhang, G. Zhang, J. Ding, W. Wang, Q. Jin, and G. Luo, "A novel sandwich immunosensing method for measuring cardiac troponin I in sera," Anal. Biochem. **321**, 209–216 (2003).
12. K. V. Gobi, C. Kataoka, and N. Miura, "Surface plasmon resonance detection of endocrine disruptors using immunoprobes based on self-assembled monolayers," Sens. Actuators B **108**, 784–790 (2005).
13. J. Treviño, A. Calle, J. M. Rodrguez-Frade, M. Mellado, and L. M. Lechuga, "Surface plasmon resonance immunoassay analysis of pituitary hormones in urine and serum samples," Clin. Chim. Acta **403**, 56–62 (2009).
14. P. Berini, "Long-range surface plasmon polaritons," Adv. Opt. Photon. **1**, 484–588 (2009).
15. Asahi Glass Company, "Cytop technical brochure," 2009 http://www.agc.com.
16. Dupont, "Teflon AF properties," http://www.dupont.com.
17. R. Slavk and J. Homola, "Ultrahigh resolution long range surface plasmon-based sensor," Sens. Actuators B **123**, 10–12 (2007).
18. V. Chabot, Y. Miron, M. Grandbois, and P. G. Charette, "Long range surface plasmon resonance for increased sensitivity in living cell biosensing through greater probing depth," Sens. Actuators B **174**, 94–101 (2012).
19. C.-T. Yang, R. Mejard, H. J. Griesser, P. O. Bagnaninchi, and B. Thierry, "Cellular micromotion monitored by long-range surface plasmon resonance with optical fluctuation analysis," Anal. Chem. **87**, 1456–1461 (2015).
20. M. Vala, S. Etheridge, J. Roach, and J. Homola, "Long-range surface plasmons for sensitive detection of bacterial analytes," Sens. Actuators B **139**, 59–63 (2009).
21. W. R. Wong, O. Krupin, F. R. M. Adikan, and P. Berini, "Optimization of long-range surface plasmon waveguides for attenuation-based biosensing," J. Lightwave Technol. **33**, 3234–3242 (2015).
22. C. Chiu, E. Lisicka-Skrzek, R. N. Tait, and P. Berini, "Fabrication of surface plasmon waveguides and devices in Cytop with integrated microfluidic channels," J. Vac. Sci. Technol. B **28**, 729–735 (2010).
23. O. Krupin, H. Asiri, C. Wang, R. N. Tait, and P. Berini, "Biosensing using straight long-range surface plasmon waveguides," Opt. Express **21**, 698–709 (2013).
24. W. R. Wong, O. Krupin, S. D. Sekaran, F. R. M. Adikan, and P. Berini, "Serological diagnosis of dengue infection in blood plasma using long-range surface plasmon waveguides," Anal. Chem. **86**, 1735–1743 (2014).
25. W. R. Wong, S. D. Sekaran, F. R. M. Adikan, and P. Berini, "Detection of dengue NS1 antigen using long-range surface plasmon waveguides," Biosens. Bioelectron. **78**, 132–139 (2016).
26. O. Krupin, C. Wang, and P. Berini, "Selective capture of human red blood cells based on blood group using long-range surface plasmon waveguides," Biosens. Bioelectron. **53**, 117–122 (2014).
27. O. Krupin, C. Wang, and P. Berini, "Detection of leukemia markers using long-range surface plasmon waveguides functionalized with protein G," Lab Chip **15**, 4156–4165 (2015).

28. M. Khodami and P. Berini, "Biomolecular kinetics analysis using long-range surface plasmon waveguides," Sens. Actuators B. **243**, 114–120 (2017).
29. M. Khodami and P. Berini, "Low detection limits using sandwich and inhibition assays on long-range surface plasmon waveguide biosensors," Sens. Actuators B **273**, 1156–1161 (2018).
30. N. R. Fong, P. Berini, and R. N. Tait, "Characterization of grating-coupled long range surface plasmon polariton membrane waveguides," Opt. Express **23**, 17421–17430 (2015).
31. N. R. Fong, M. Menotti, E. Lisicka-Skrzek, H. Northfield, A. Olivieri, N. Tait, M. Liscidini, and P. Berini, "Bloch long-range surface plasmon polaritons on metal stripe waveguides on a multilayer substrate," ACS Photon. **4**, 593–599 (2017).
32. N. R. Fong, P. Berini, and N. Tait, "Fabrication of long-range surface plasmon hydrogen sensors on Cytop membranes integrating grating couplers," J. Vac. Sci. Technol. B **33**, 021201 (2015).
33. A. Hessel and A. Oliner, "A new theory of Wood's anomalies on optical gratings," Appl. Opt. **4**, 1275–1297 (1965).
34. D. Taillaert, F. Van Laere, M. Ayre, W. Bogaerts, D. Van Thourhout, P. Bienstman, and R. Baets, "Grating couplers for coupling between optical fibers and nanophotonic waveguides," Jpn. J. Appl. Phys. **45**, 6071–6077 (2006).
35. J.-M. Lee, K.-J. Kim, and G. Kim, "Enhancing alignment tolerance of silicon waveguide by using a wide grating coupler," Opt. Express **16**, 13024–13031 (2008).
36. F. Van Laere, G. Roelkens, M. Ayre, J. Schrauwen, D. Taillaert, D. Van Thourhout, T. F. Krauss, and R. Baets, "Compact and highly efficient grating couplers between optical fiber and nanophotonic waveguides," J. Lightwave Technol. **25**, 151–156 (2007).
37. N. Bonod, E. Popov, L. Li, and B. Chernov, "Unidirectional excitation of surface plasmons by slanted gratings," Opt. Express **15**, 11427–11432 (2007).
38. B. Bai, X. Meng, J. Laukkanen, T. Sfez, L. Yu, W. Nakagawa, H. P. Herzig, L. Li, and J. Turunen, "Asymmetrical excitation of surface plasmon polaritons on blazed gratings at normal incidence," Phys. Rev. B **80**, 035407 (2009).
39. B. H. Kleemann, J. Ruoff, and R. Arnold, "Area-coded effective medium structures, a new type of grating design," Opt. Lett. **30**, 1617–1619 (2005).
40. "Comsol Multiphysics reference manual, version 5.3," https://www.comsol.com.
41. C. Chen and P. Berini, "Grating couplers for broadside input and output coupling of long-range surface plasmons," Opt. Express **18**, 8006–8018 (2010).

Chapter 4.

Electrochemical Performance of Lithographically Defined Micro-Electrodes for Integration and Device Applications

4.1. Summary

It is of considerable interest to design and develop ultra-compact electrochemical sensing devices that use small, lithographically defined, closely-spaced metallic features with dimensions and separations in the micrometre range. Microelectrode systems such as these can be integrated with microfluidics and optical biosensors, such as surface plasmon waveguide sensors, to enable multi-modal sensing. By performing cyclic voltammetry (CV) measurements with potassium ferricyanide as the redox species in potassium nitrate as the supporting electrolyte, we investigate lithographically defined gold and platinum micro-electrodes. Voltammograms are used to estimate the magnitude of the double-layer capacitance. Based on our CV measurements, potassium ferricyanide concentration curves were extracted as a function of scan rate and could be employed as calibration curves from which a concentration of potassium ferricyanide in the range of 0.5–5 mM can be determined. To confirm the validity of the calibration curve, a blind test was conducted. Our CV measurements are also fitted to the Randles-Sevcik equation to determine the diffusion coefficient of potassium ferricyanide. In our study, we compared our CV measurements with those obtained using macroscopic commercial electrodes, demonstrating good agreement, and indicating that the CV curve shape is not determined by the geometry of the microelectrodes (but by the area). In addition to comparing our CV measurements with theoretical curves computed using the Butler–Volmer equation, we

obtained an essentially perfect agreement on the rate constant at zero potential for our redox species. Furthermore, we compare the results obtained with electrodes as-deposited with those obtained with burn-in to demonstrate the importance of stabilizing electrodes from electromigration and grain reorganization before use in CV measurements. Electrochemical sensing devices generally benefit from burning in (or annealing) lithographic microelectrodes before use.

4.2. Contribution

The results provided in this chapter are published in Chemosensors. Zohreh Hirbodvash designed the experiments and carried out the measurements, performed the theoretical calculations, interpreted the results and wrote the manuscript. Mohamed S. E. Houache, Oleksiy Krupin, and Anthony Olivieri helped in designing the setup. Biosensor chips used in this series of experiments were fabricated by Maryam Khodami, and Howard Northfield, former members of our group.

Dr. Berini and Dr. Baranova contributed to the interpretation of the results and revised the manuscript.

4.3. Article

The article follows here verbatim.

chemosensors

Article

Electrochemical Performance of Lithographically-Defined Micro-Electrodes for Integration and Device Applications

Zohreh Hirbodvash [1,2], Mohamed S. E. Houache [3], Oleksiy Krupin [2], Maryam Khodami [2,4], Howard Northfield [2], Anthony Olivieri [2], Elena A. Baranova [3] and Pierre Berini [1,2,4,*]

[1] Department of Physics, University of Ottawa, 150 Louis Pasteur, Ottawa, ON K1N 6N5, Canada; [redacted]
[2] Center for Research in Photonics, University of Ottawa, 25 Templeton St., Ottawa, ON K1N 6N5, Canada; okrupin097@uottawa.ca (O.K.); mkhod007@uottawa.ca (M.K.); Howard.Northfield@uottawa.ca (H.N.); aolivie5@uottawa.ca (A.O.)
[3] Department of Chemical and Biological Engineering, Center for Catalysis Research and Innovation (CCRI), University of Ottawa, 161 Louis-Pasteur, Ottawa, ON K1N 6N5, Canada; mhoua015@uottawa.ca (M.S.E.H.); Elena.Baranova@uottawa.ca (E.A.B.)
[4] School of Electrical Engineering and Computer Science, University of Ottawa, 800 King Edward Ave., Ottawa, ON K1N 6N5, Canada
[*] Correspondence: pberini@uOttawa.ca

Abstract: Small; lithographically-defined and closely-spaced metallic features of dimensions and separation in the micrometer range are of strong interest as working and counter electrodes in compact electrochemical sensing devices. Such micro-electrode systems can be integrated with microfluidics and optical biosensors, such as surface plasmon waveguide biosensors, to enable multi-modal sensing strategies. We investigate lithographically-defined gold and platinum micro-electrodes experimentally, via cyclic voltammetry (CV) measurements obtained at various scan rates and concentrations of potassium ferricyanide as the redox species, in potassium nitrate as the supporting electrolyte. The magnitude of the double-layer capacitance is estimated using the voltammograms. Concentration curves for potassium ferricyanide are extracted from our CV measurements as a function of scan rate, and could be used as calibration curves from which an unknown concentration of potassium ferricyanide in the range of 0.5–5 mM can be determined. A blind test was done to confirm the validity of the calibration curve. The diffusion coefficient of potassium ferricyanide is also extracted from our CV measurements by fitting to the Randles–Sevcik equation ($D = 4.18 \times 10^{-10}$ m^2/s). Our CV measurements were compared with measurements obtained using macroscopic commercial electrodes, yielding good agreement and verifying that the shape of our CV curves do not depend on micro-electrode geometry (only on area). We also compare our CV measurements with theoretical curves computed using the Butler–Volmer equation, achieving essentially perfect agreement while extracting the rate constant at zero potential for our redox species ($k^o = 10^{-6}$ m/s). Finally, we demonstrate the importance of burn-in to stabilize electrodes from the effects of electromigration and grain reorganization before use in CV measurements, by comparing with results obtained with as-deposited electrodes. Burn-in (or equivalently, annealing) of lithographic microelectrodes before use is of general importance to electrochemical sensing devices

Keywords: biosensors; cyclic voltammetry; microfluidics; lithographic microelectrodes

check for updates

Citation: Hirbodvash, Z.; Houache, M.S.E.; Krupin, O.; Khodami, M.; Northfield, H.; Olivieri, A.; Baranova, E.A.; Berini, P. Electrochemical Performance of Lithographically-Defined Micro-Electrodes for Integration and Device Applications. *Chemosensors* **2021**, *9*, 277. https://doi.org/10.3390/chemosensors9100277

Academic Editor: Patricia Khashayar

Received: 30 August 2021
Accepted: 25 September 2021
Published: 28 September 2021

1. Introduction

Small, closely spaced metallic features of dimensions and separation in the micrometer range are of interest in electrochemical device applications or for integration with optical biosensors, e.g., based on surface plasmon-polaritons (SPPs) [1–3]. Optical biosensors exploiting long-range surface plasmon-polariton (LRSPP) waveguides have solicited significant interest because they enable compactness in integrated architectures, and offer very high sensitivity in an arrayed format [4–7]. LRSPPs are supported by a thin metal slab or stripe bounded by dielectrics of similar refractive index [8]. For biosensing, the metal stripe is typically formed of Au and is supported by a cladding of low refractive index, e.g., a fluoropolymer such as Cytop, which has an index close to water and is thus well-matched to the index of aqueous biosensing media [5,6]. Alternatively, Au-sensing waveguides can be fabricated on a multilayer dielectric cladding, behaving optically as a 1-D photonic crystal (1DPC), and supporting Bloch LRSPPs within the bandgap of the 1DPC [4,5,7]. Advantageously, the multilayer cladding in such structures can be formed of robust inorganic dielectrics (e.g., SiO_2, Si_3N_4, Ta_2O_5), allowing multiple wafer-scale processing steps to be applied thereon, thereby enabling a high degree of integration and conferring strength and resilience to the chips [7].

Prism-coupled surface plasmon resonance (SPR) biosensors have been combined with other sensing techniques, such as mass spectroscopy [9–11], SELEX [12], and electrochemistry [13–27]. An early study on electrochemical SPR reports the use of surface plasmons to probe the electrochemical interface in perchlorate and halide electrolytes [13]. In another study, the SPR response was monitored as the potential on the Au sensing surface was cycled similarly to cyclic voltammetry [14]. Electrochemical SPR was recently used for the label-free detection of the cancer biomarker miRNA-145 [15].

The drive towards compactness and high levels of integration has motivated electrochemical SPR sensing approaches based on Au micro- and nano-structures [16,17]. Electrochemical SPR sensors on optical fibers present another alternative [18], where a gold-coated optical fiber sensor was also used as the working electrode in an electrochemical set-up [19]. In recent work, a flow-injection electrochemical plasmonic optical fiber sensor was proposed, with the sensor inserted into a PDMS flow channel [20].

Other approaches to integrating optical and electrochemical sensing include a gold-coated graded-index optical waveguide sensor, where changes in optical transmittance were measured while cyclic voltammetry was performed in sulfuric or perchloric acid solutions [21]. An electrochemical thin-film chlorine sensor on a planar optical waveguide was also proposed to measure oxidation in the thin-film by monitoring the light transmitted through the waveguide [22]. An electrochemical SPR glucose biosensor was reported, with the ability to detect enzymatic reactions in a conducting polymer/glucose oxidase (Gox) multilayer thin film [23]. In addition to sensing applications, combining electrochemical probes with plasmonic structures is of interest in the investigation of light-induced hot-carrier electrochemical reactions [24–27].

Cyclic voltammetry (CV) plays an essential role in the interrogation of electrochemical sensors in general [28]. Voltammetry can be the fundamental mode of operation of a sensor because the measured current is linearly dependent on the analyte concentration in a well-designed system [29]. Furthermore, a single scan is very rich in information on the chemical and physical behaviors of an electrochemical system, and CV can be inexpensively implemented in a compact form-factor [28,29].

Motivated by the high sensitivity of Au stripe LRSPP waveguide biosensors [4–7], along with their suitability for high levels of integration, we investigate microelectrode systems suitable for integration with such optical biosensors, to ultimately enable multi-modal sensing strategies, of strong interest in, e.g., disease detection problems. The use of high-volume wafer-scale manufacturing tools and techniques in the fabrication of the sensors ensures a low chip cost. Electrochemical measurements are performed in the form of CV for different scan rates and concentrations of the redox species (potassium ferricyanide). We also demonstrate the importance of microelectrode burn-in (current annealing) before performing electrochemical measurements. Burn-in is a crucial issue, inducing electromigration and grain reorganization in lithographically-defined and evaporated electrodes, ultimately stabilizing them before use. Peak oxidative currents in the CV measurements are plotted vs. concentration and used as a calibration curve, from which an unknown concentration of potassium ferricyanide in the range of 0.5–5 mM can be determined. The diffusion coefficient of potassium ferricyanide is obtained by fitting our experimental data to the Randles–Sevcik equation. A comparison of CV measurements with theoretical results computed using the Butler–Volmer equation is done while extracting the rate constant at zero potential of our redox species.

2. Experimental

2.1. Electrode Structures

Figure 1a shows a sketch of a chip bearing a Au LRSPP waveguide designed to also operate as a working electrode (WE), a Pt counter electrode (CE), and Pt/Cu electrical contact pads. These structures were arranged in an array along the width of the chip to enable multiple sensing channels. The metal structures are supported by a multilayer dielectric stack consisting of 15 periods of SiO_2/Ta_2O_5. Both Au and Pt stripes are lithographically defined and evaporated. Fabrication details and the optical operation of the LRSPPs waveguides are reported elsewhere [4,5,7].

Identical dimensions were used for the Au and Pt stripes, as illustrated in Figure 1a. Figure 1b gives a microscope image taken near the top of a chip, showing portions of contact pads to working and counter electrodes (the substrate appears green). An atomic force microscope (AFM) scan of both stripes reveals that their thickness is 35–40 nm (including 3 nm of Ti for adhesion), and that the roughness levels are less than 2 nm (RMS) along the top surface of both. The edge-to-edge lateral separation between them is l_s = 40 µm. The contact pads are formed of a Pt/Cu stack, 50/200 nm in thickness. The Pt layer is used to passivate the Cu and provide a more resilient surface for probing. The geometry, dimensions and thickness of the Au working electrodes are constrained by their dual use as Bloch LRSPP waveguides [4]. An identical design was adopted for the Pt counter electrodes for simplicity.

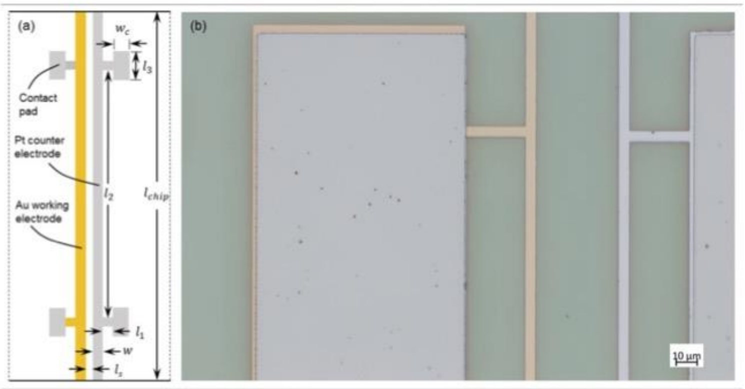

Figure 1. (**a**) Schematic (not to scale) of a chip bearing a Au LRSPP waveguide/working electrode, Pt counter electrode, and electrical contact pads on a multilayer dielectric substrate. The dimensions are: l_1 = 29 µm, l_2 = 2600 µm, l_3 = 250 µm, l_{chip} = 3000 µm, w_c = 100 µm, w = 5 µm, l_s = 40 µm. (**b**) Microscope image of a fabricated chip.

2.2. Electromigration

Electromigration and grain reorganization may occur initially when a current density flows for the first time through an as-deposited metal nanostructure or stripe [30–32]. Electromigration occurs mainly via the current-induced migration of metal ions along the grain boundaries of a structure, and grain reorganization consists mainly of thermally-driven coalescence of small grains into larger ones. Consequently, metal electrodes should be stabilized, through annealing, or burn-in via the passage of current density, before use in a CV experiment. In the case of burn-in, the injected current density induces electromigration and heating via Ohmic loss leading to grain reorganization, the effects of which are evident in the evolution of the measured resistance of the structure as a function of current density and time.

A controlled voltage was applied to a metal stripe, via a pair of probes touching its contact pads, and the injected current and resistance were measured. The applied voltage was increased in steps of 0.1 V with each voltage held constant for 10 s. The burn-in process was repeated a few times to determine the burn-out (open-circuit) point of the stripes, which was about 30 V for our Au stripes and 120 V for our Pt stripes. Once these values were known, the burn-in process consisted of cycling the applied voltage several times to just below the burn-out point until electromigration and grain reorganization no longer occurred, as evidenced by a stable measured resistance.

Figure 2 shows typical measured burn-in curves for as-deposited (evaporated) Au and Pt stripes, consisting of cycling the voltage applied between a pair of pads at each end of a stripe, six times (6 runs) while measuring the current and resistance. Run 1 in both cases shows the stripe resistance increasing with voltage up to a threshold, 22 V for the Au stripe (Figure 2a) and 60 V for the Pt stripe (Figure 2b), beyond which the resistance flattens, to then increase again with voltage. The behavior observed in run 1 for both stripes indicates that electromigration and current-induced thermal annealing occurred on the stripes, resulting in grain reorganization and lowered stripe resistance. After cycling a few additional runs, the stripe resistance stabilizes with no further significant grain reorganization. In this regime, the stripe resistance varies with voltage in a manner that is consistent with the dependence of resistivity on temperature, and the electrodes are deemed ready for CV measurements. Using electrodes as-evaporated (not burned-in or annealed) produce inaccurate CV results, as demonstrated and discussed further below.

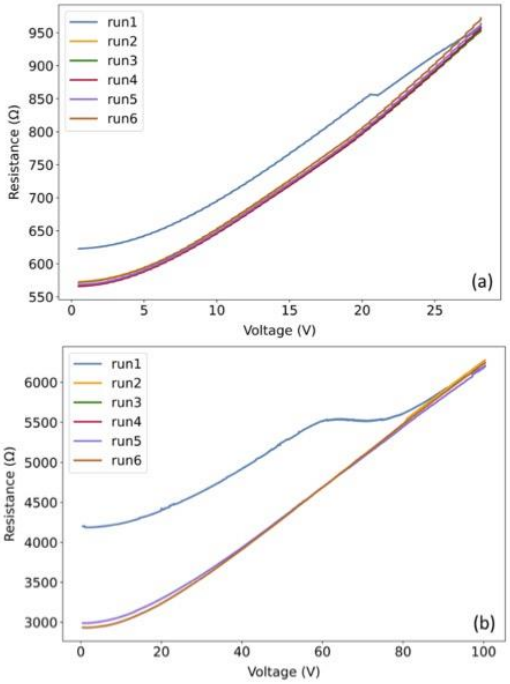

Figure 2. Measured stripe resistance vs. voltage in steps of 0.1 V. Each voltage step was held constant for 10 s. (**a**) Au stripe over the voltage range from 0.5 to 30 V; (**b**) Pt stripe over the voltage range from 0.5 to 100 V.

2.3. Materials

Potassium ferricyanide, potassium nitrate, and an external Ag/AgCl reference electrode (double junction PH combination, glass body, BNC connector) were purchased from (Sigma-Aldrich Canada Ltd, Oakville, ON, Canada). The cyclic voltammetry experiments were performed by a WaveDriver 20 BiPotentiostat (basic bundles) from (Pine Research Instrumentation Inc., Durham, NC, USA). A commercial Au electrode (outer diameter 6 mm, inner diameter 1.6 mm) was purchased from London Scientific.

2.4. Setup

CV experiments were performed with a Au stripe operating as the working electrode, and a neighboring Pt stripe operating as the counter electrode, both on chip, as sketched in Figure 1. Potassium ferricyanide (a mediator for glucose detection) was used as the redox species [33,34]. CV measurements were obtained for various potassium ferricyanide concentrations. Specifically, the experiments were carried out using 20 mL of 0.5, 1, 3, and 5 mM potassium ferricyanide, dissolved in 100 mM potassium nitrate as the supporting electrolyte, the latter providing low resistance and high ionic strength, leading to unperturbed near-zero electric fields within the electrochemical cell [35] CV experiments were carried out over the potential range of 0–0.5 V vs. the Ag/AgCl reference electrode using a triangular waveform at scan rates of 5, 10, 20, 50, and 100 mV/s (see Appendix A.1) Applying such a voltage to the system leads to the reversible reaction of potassium ferricyanide ($K_3[Fe(CN)_6]$) to potassium ferrocyanide ($K_4[Fe(CN)_6]$) as a redox couple in a 1-electron transfer process:

$$K_4[Fe(CN)_6] \leftrightarrow K_3[Fe(CN)_6] + e^- \tag{1}$$

The electrochemical cell made of glass consisted of a Petri dish with the chip affixed to the bottom with epoxy. Electrical contacting to the working electrode (Au stripe) and counter electrode (Pt stripe) was achieved using two tungsten needles. The needles were attached to the arms of two precision positioners to align and establish contact to the contact pads. Any possible reaction between the needles and the redox species or the electrolyte was eliminated by coating the body of the needles with PMMA (except for their tips). The chip was then immersed in electrolyte. The Ag/AgCl reference electrode was also immersed in electrolyte to establish a constant and stable reference potential (Appendix A.1).

The tungsten needles, coated with poly (methyl methacrylate)—PMMA—except for their tips, were independently tested to make sure that they have no effects on the CV measurements. A needle was immersed in the solution (1 mM of potassium ferricyanide as the redox species in 100 mM of potassium nitrate) and used as a working electrode. An external Pt wire was used as a counter electrode along with the Ag/AgCl reference electrode. CV experiments were carried out at different scan rates (5, 10, 20, 50, and 100 mV/s). The measured currents produced no discernable patterns and were in the range of nA, which corresponds to the noise floor of our potentiostat. The probing needles therefore do not interact electrochemically in this system.

3. Results and Discussion

3.1. CV Measurements

Figure 3 shows the cyclic voltammograms obtained using the on-chip Au and Pt stripes as working and counter electrodes (Figure 1a), for different scan rates and concentrations of ferricyanide.

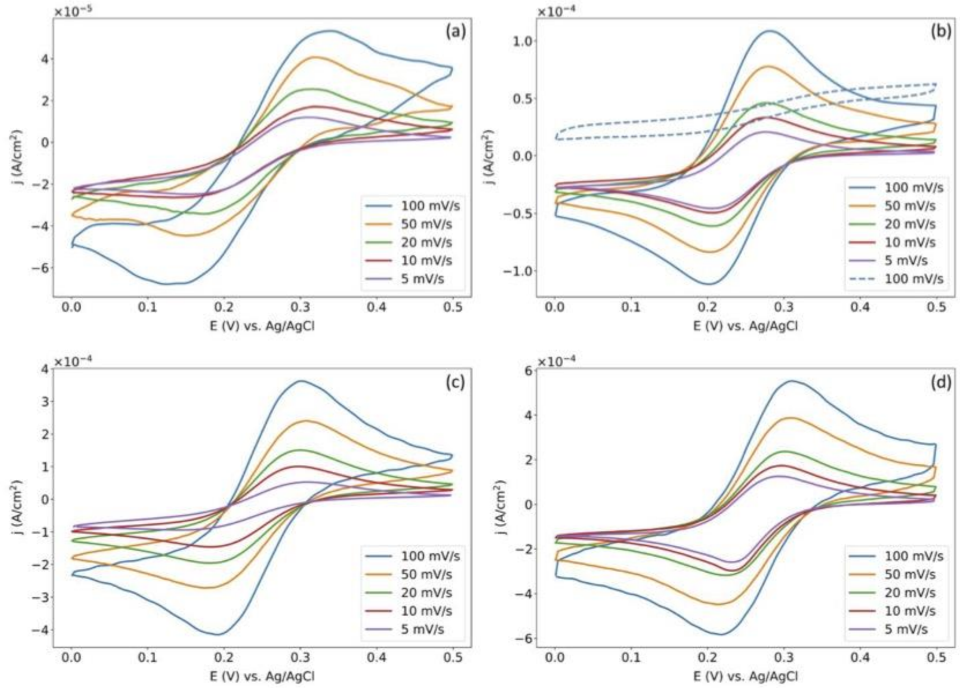

Figure 3. Cyclic voltammograms of Au stripes on chip, at different scan rates (legend), for different concentrations of potassium ferricyanide: (**a**) 0.5 mM, (**b**) 1 mM, (**c**) 3 mM, (**d**) 5 mM. The dash-dot curve in (**b**) corresponds to a CV measurement for electrodes that were not burned-in (cf. electromigration section).

The results of Figure 3 were obtained using on-chip electrodes of identical design with different concentrations of the redox species. Comparing the results reveals that the CV curves are very similar, the main difference being the magnitude of the currents measured. As discussed earlier, the measurements were carried out under a high electrolyte concentration, such that the main difference between the experiments is the concentration of the redox species.

Slight differences in the shape of the CV curves are attributed to the use of different chips in gathering the measurements reported in the four panels of Figure 3. Different chips were needed because of accumulated damage caused to the contact pads during repeated probing. However, a complete set of experiments for a specific concentration (e.g., 0.5 mM) involving all scan rates was completed with the same on-chip electrodes.

In cases where the same on-chip electrodes could be used, cleaning between measurements involving different concentrations is required. For cleaning, a chip was placed into a large glass vial of acetone which was then transferred to into an ultrasonic bath for 5 min. Next, the chip was immediately rinsed using pipettes filled with 3–4 isopropyl alcohol (IPA), followed by deionized (DI) water, and then N_2 gas was used to blow dry the chip. Finally, the chip was placed into a UV/ozone chamber with the UV source on for 30 min then off for another 30 min.

Figure 3b also shows a CV measurement at a scan rate of 100 mV/s for electrodes that were not burned-in (dashed-dot curve, cf. electromigration sub-section). As is obvious from this plot, the oxidation and reduction peaks have essentially disappeared. The need to properly burn-in (anneal) micro-electrodes before use in an electrochemical experiment is manifest.

Figure 4 compares the results of Figure 3b with voltammograms obtained using a commercial Au working electrode (outer diameter 6 mm, inner diameter 1.6 mm), and a Pt wire as a counter electrode (the surface area of the Au working electrode on chip is 0.588 mm^2 and the surface area of the commercial Au electrode is 2.010 mm^2 for an area ratio of 3.42).

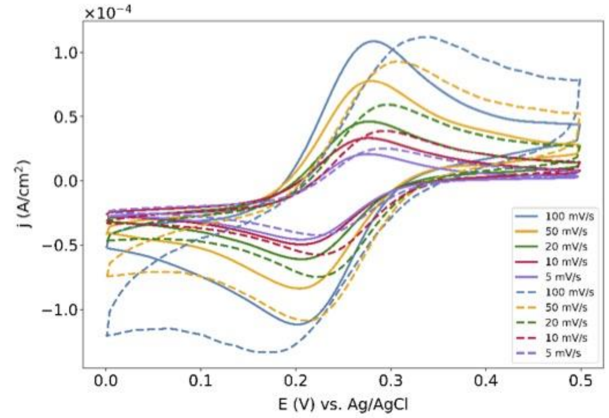

Figure 4. Cyclic voltammograms of Au stripes on chip electrode (solid curves), at different scan rates (legend), compared to measurements obtained using a commercial Au electrode (dashed curves) in 1 mM ferricyanide solution.

As shown in Figure 4, the results obtained using the electrodes on chip are very similar to those obtained using the commercial electrodes. The cathodic and anodic peaks are clearly identifiable in all CV curves and agree well for both sets of electrodes. Referring to the 50 mV/s scan rate, an oxidative current peak at 1.91 µA for an oxidative potential of 0.28 V, and a reductive current peak at −2.23 µA for a reductive potential of 0.21 V, are noted for the commercial electrodes (Figure 4, dashed curves). In the case of the electrodes on chip, the oxidative current peaks at 0.495 µA for an oxidative potential of 0.280 V, and the reductive current peaks at −0.513 µA for a reductive potential of 0.204 V (Figure 4, solid curves). The mean value of the oxidative and reductive potentials occurs at 0.24 V for both sets of electrodes.

Electrochemical impedance spectroscopy (EIS) can be used to determine the electrolyte double-layer capacitance of electrochemical cells. Another approach consists of using CV measurements, as charging currents (forward segment of CV curve) and discharging currents (reverse segment of CV curve) are observed whenever a potential sweep is applied across a capacitive load. The double-layer charging current (i_{DL}) is related to the potential sweep rate (ν) and the double-layer capacitance (C_{DL}) at the surface of a working electrode by the following equation [36]:

$$i_{DL} = C_{DL}\vartheta \tag{2}$$

The vertical separation between the two segments at any point along a voltammogram is equal to $2i_{DL}$. Choosing a point and plotting i_{DL} vs. ν yields C_{DL} from the slope of the graph. Using the data plotted in Figure 3 we find a double-layer capacitance of C_{DL} = 0.29 µF for the working electrode on chip, and C_{DL} = 1.02 µF for the commercial electrode.

3.2. Calibration Curves

The magnitude of the current in the CV curves of Figure 3 is directly proportional to the concentration of redox species. Figure 5 plots the peak oxidative current from these CV curves vs. the concentration of redox species for different scan rates. The plots are clearly linear and can be used as calibration curves to determine unknown concentrations of redox species (in this case potassium ferricyanide) after carrying out a cyclic voltammetry experiment using a similar chip.

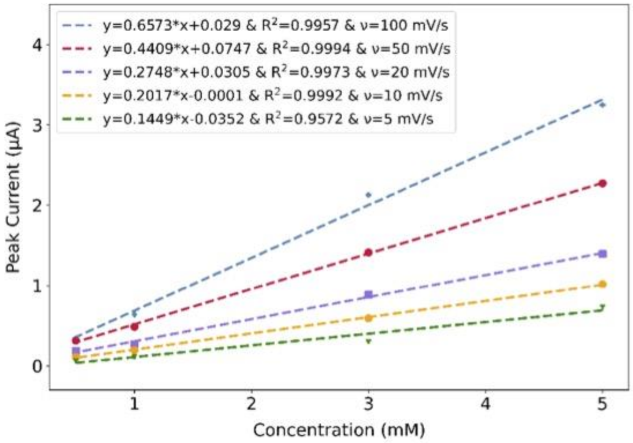

Figure 5. Calibration graphs for various scan rates (legend), taken as the peak oxidative current vs. the concentration of potassium ferricyanide, based on the CV curves of Figure 3, obtained using on-chip Au electrodes.

The intercepts in Figure 5 are not zero as expected when the concentration of redox species is zero. The main cause is noise in the set-up. The noise current of our set-up was measured and found to be in the range of 2–100 nA. This range was obtained using the same setup and electrolyte, but without the redox species.

Blind testing was carried out to ensure that the calibration curves yield the correct concentration of redox species. Electrolyte solutions with three different concentrations of redox species were prepared and given to the experimentalist without communicating the concentrations. The experimentalist performed CV experiments and used Figure 5 to determine the unknown concentration of redox species based on the peak current. The three concentrations measured were 0.5, 2, and 3 mM, corresponding to the prepared concentrations to within 2%.

3.3. Diffusion Coefficient

The diffusion coefficient of a redox species can be obtained from the Randles–Sevcik equation, which describes the relationship between the peak oxidative current, the scan rate, and the diffusion coefficient as follow:

$$i_p = 0.4463\, nFAC\left(\frac{n\, F\vartheta D}{RT}\right)^{1/2} \tag{3}$$

where i_p is the peak oxidative current (A), n is the number of electrons transferred per redox event (here $n = 1$), A is the electrode area (m^2), D is the diffusion coefficient (m^2/s), C is the concentration of the redox species (mol/m^3), ϑ is the scan rate (V/s), R is the gas constant (J/(mol·K)), T is the temperature (K), and F is the Faraday constant (C/mol). The diffusion coefficient of potassium ferricyanide can be obtained from the slope of the peak oxidative current plotted against the square root of the scan rate. The diffusion coefficient thus obtained for potassium ferricyanide using our on-chip electrodes is 4.18×10^{-10} m^2/s, which is in very good agreement with the literature [37].

3.4. Theoretical

A brief synopsis of the applicable theory [38–41] is given in the Appendices A.2 and A.3 The current density passing through the electrode is given by the Butler–Volmer equation (Appendix A.2) [40]:

$$j = Fk^{\circ}\left\{c_{red}^{s}\exp\left(\frac{\alpha\, F\,(E-E^{\circ})}{RT}\right) - c_{ox}^{s}\exp\left(-\frac{(1-\alpha\,)F\,(E-E^{\circ})}{RT}\right)\right\} \tag{4}$$

c_{red}^{s} and c_{ox}^{s} evaluated from the general expressions given in the Appendix A.3, at the electrode position ($x = 0$) (i.e., $c_{red}^{s} = c_{red}(x = 0, t)$, $c_{ox}^{s} = c_{ox}(x = 0, t)$). E is the electrode potential as a function of time (e.g., Figure A1a in the Appendix A), and E° is the equilibrium potential which can be obtained from the experimental curves. Thus, the total current density due to both the reduced and oxidized species is:

$$\begin{aligned} j = Fk^{\circ}\exp(\mu^2 Dt)\,\mathrm{erfc}\left(\mu\sqrt{Dt}\right)\exp\left(\tfrac{|\eta|}{b}\right)\left[c_{ox}^{b}\exp\left(\tfrac{\alpha\, F\,(E-E^{\circ})}{RT}\right)\right. \\ \left. -c_{red}^{b}\exp\left(-\tfrac{(1-\alpha\,)F\,(E-E^{\circ})}{RT}\right)\right] \end{aligned} \tag{5}$$

where α is the transfer coefficient. The anodic and cathodic transfer coefficients, α_a and α_c, are defined by the following equations [42]:

$$\alpha_a = \frac{RT}{F}\left(\frac{d\ln j_a}{dE}\right),\ \alpha_c = \frac{RT}{F}\left(\frac{d\ln j_c}{dE}\right) \tag{6}$$

where j_a and j_c are the anodic and cathodic current densities, respectively. For a 1 electron transfer reaction the transfer coefficient is termed the symmetry factor and could be taken equal to 0.5. Indeed, Figure 3 reveals that the CV curves are symmetric in our case, about the equilibrium potential, E°, so setting $\alpha_a = \alpha_c = \alpha = 0.5$ is justified.

Figure 6 plots the computed current vs. the applied potential E for scan rates of 10 and 100 mV/s. The current was taken as jA where $A = 0.588$ mm^2 is the area of the on-chip working electrode and the current density, j, was computed via Equation (4). For potassium ferricyanide as the redox species, in potassium nitrate as the electrolyte, we extract $k^{\circ} = 10^{-6}$ m/s by adjusting the theoretical curves to the experimental results of Figure 3 (re-plotted in Figure 6 for convenience). The theoretical and experimental CV curves are in excellent quantitative agreement.

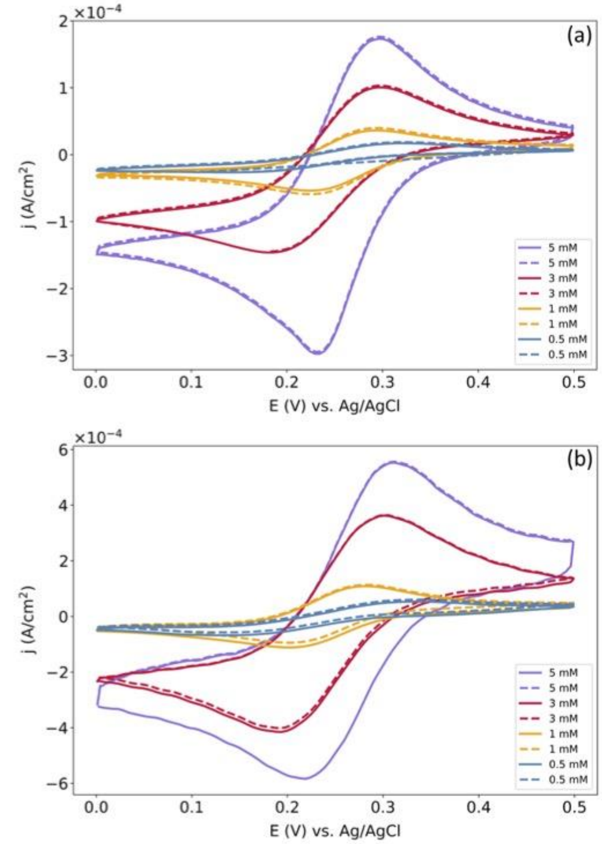

Figure 6. Experimental cyclic voltammogram obtained using Au stripes on chip as working electrodes (solid curve), at a scan rate of (**a**) 10 mV/s and (**b**) 100 mV/s, compared to the computed voltammograms (dashed curves). The concentration of potassium ferricyanide (redox species) was set to 0.5, 1, 3, and 5 mM, as labelled in the legend, in 100 mM of potassium nitrate as the electrolyte.

4. Conclusions

Lithographically-defined and evaporated microelectrodes on a substrate are effective structures for electrochemistry as long as they are burned-in, or (equivalently), annealed before use. Micro-electrodes are of strong interest in compact chip-based electrochemical sensing devices. The working electrodes investigated here serve an additional purpose, that of supporting long-range surface plasmons for optical biosensing which constrains its geometry to that of a thin, narrow, and straight stripe. When operated in sufficiently conductive electrolyte, the shape of the electrode has no bearing on the CV measurements, but its area sets the magnitude of the currents involved.

Evaporated gold and platinum micro-electrodes, used as working and counter electrodes, respectively, produced CV measurements in good agreement with commercial (macroscopic) electrodes. Potassium ferricyanide was used as the model redox system, given the reversible nature of the reaction, and its relevance to glucose sensing. Scan-rate dependent concentration curves for potassium ferricyanide were extracted as the peak oxidative currents in the CV measurements. The diffusion coefficient of potassium ferricyanide, extracted by fitting our experimental data to the Randles–Sevcik equation, is in excellent agreement with the literature. The CV measurements compare very well to theoretical results computed using the Butler–Volmer equation, allowing extraction of the rate constant at zero potential of our redox species.

Micro-electrode systems as investigated here can be integrated with microfluidics and other sensing structures, such as surface plasmon waveguide biosensors, to enable multi-modal sensing strategies.

Author Contributions: Conceptualization, P.B.; methodology, Z.H., M.S.E.H., O.K., M.K., H.N., A.O. and P.B.; validation, Z.H., M.S.E.H., O.K., E.A.B. and P.B.; formal analysis, Z.H., M.S.E.H., O.K., E.A.B. and P.B.; investigation, Z.H.; data curation, Z.H.; writing—original draft preparation, Z.H.; writing—review and editing, M.S.E.H., O.K., E.A.B. and P.B.; supervision, P.B.; funding acquisition, P.B. All authors have read and agreed to the published version of the manuscript.

Funding: This work was supported by the Natural Sciences and Engineering Research Council of Canada. The contract or grant number is 210396.

Institutional Review Board Statement: Not applicable.

Informed Consent Statement: Not applicable.

Data Availability Statement: Data is contained within the article.

Conflicts of Interest: The authors declare no conflict of interest.

Appendix A

Appendix A.1. Setup

A triangular voltage wave, as sketched in Figure A1a, was applied within a potential window selected to reveal the redox current peaks.

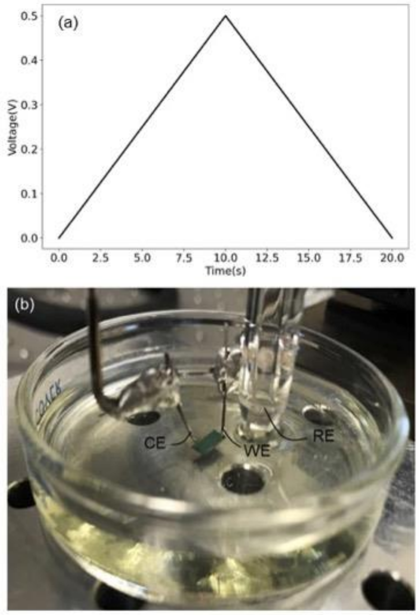

Figure A1. (**a**) Example triangular voltage waveform applied in the CV measurements (0.5 V peak, 50 mV/s scan rate). (**b**) Full CV set-up showing probe needles contacting a chip (green) bearing a Au working electrode (WE) and a Pt counter electrode (CE), and a Ag/AgCl reference electrode (RE).

Appendix A.2. Butler–Volmer Equation

Electrode reactions and kinetics describe the relationship between concentration and current density, and the reaction rate depends on the distribution of the species (concentrations and pressures), the temperature, and the electrode potential, E. The net rate of the electrochemical reaction per unit area of electrode, γ_{net} (mol/M·s), equals the rate of oxidation minus rate of reduction:

$$\gamma_{net} = K_{ox} c^{s}_{red} - K_{red} c^{s}_{ox} \tag{A1}$$

where $c^{s}_{red,ox}$ is the concentration at the surface of the electrode of the reduced and oxidized species (mol/m^3), and $K_{red,ox}$ is the rate constants of reductant and oxidant (m/s). The rate constants are determined using absolute rate theory:

$$K_{ox} = A\exp\left(-\frac{\Delta G^{+}_{ox}(E)}{RT}\right) \text{ and } K_{red} = A\exp\left(-\frac{\Delta G^{+}_{red}(E)}{RT}\right) \tag{A2}$$

where A is a factor (pre-exponential constant in the Arrhenius equation), and $\Delta G^{+}_{ox\ ,red}(E)$ are the molar Gibbs free energies of activation of the oxidized or reduced species (J·K/mol). The molar Gibbs free energies are expressed in the following forms for anodic and cathodic reactions:

$$\Delta G^{+}_{ox}(E) = \Delta G^{+}_{ox}(E^{\circ}) - \alpha_a F\left(E - E^{\circ}\right) \text{ and } \Delta G^{+}_{red}(E) = \Delta G^{+}_{red}(E^{\circ}) + \alpha_c F\left(E - E^{\circ}\right) \tag{A3}$$

where α_a and α_c are the anodic and cathodic transfer coefficients, which must satisfy $\alpha_a + \alpha_c = 1$. Setting $\alpha_a = \alpha$ and $\alpha_c = 1 - \alpha$, we rewrite Equation (A2) as:

$$K_{ox} = \exp\left(-\frac{\Delta G^{+}_{ox}(E)}{RT}\right) = k^{\circ}\exp\left(\frac{\alpha\ F\ (E - E^{\circ})}{RT}\right)$$

$$K_{red} = A\exp\left(-\frac{\Delta G^{+}_{red}(E)}{RT}\right) = k^{\circ}\exp\left(-\frac{(1-\alpha\ )F\ (E - E^{\circ})}{RT}\right) \tag{A4}$$

where $k^{\circ} = A\exp\left(-\frac{\Delta G^{+}_{red}(E^{\circ})}{RT}\right)$.

The observed current density, in units of A/m^2, of the electrode reaction can be expressed as:

$$j = F\gamma_{net} = F(K_{ox} c^{s}_{red} - K_{red} c^{s}_{ox}) \tag{A5}$$

Substituting Equation (A4) into Equation (A5) yields the Butler–Volmer equation (Equation (4) of the main text):

$$j = Fk^{\circ}\left\{c^{s}_{red}\exp\left(\frac{\alpha\ F\ (E - E^{\circ})}{RT}\right) - c^{s}_{ox}\exp\left(-\frac{(1-\alpha)F\ (E - E^{\circ})}{RT}\right)\right\} \tag{A6}$$

Comparing experimental results with theory is useful to validate the electrode designs and the experimental techniques applied, and to extract further information about the redox reactions.

Appendix A.3. Concentration

The Poisson–Nernst–Planck (PNP) equations model a mean-field approximation for ion interactions involving ionic concentration and the electric potential. These equations model ion and charge transport problems in semiconductor devices, electrochemistry and biological systems. In electrochemistry, the PNP model describes the influence of an ionic concentration gradient and of an electric field on the flux of chemical species, specifically ions.

The general form of the conservation of mass equation for an incompressible fluid is combined with the equation for flux density to describe mass transport in a system:

$$\frac{\partial c_i}{\partial t}+\boldsymbol{u}\,\nabla c_i-\nabla\left[D(\nabla c_i+u_{m,i}z_iFc_i\,\nabla\varphi)\right]\;=\;0 \tag{A7}$$

In the above, c_i is the molar concentration (mol/m^3), $\boldsymbol{u}$ is the drift velocity vector (m/s), D is the diffusion coefficient (m^2/s), $u_{m,i}$ is the mobility (s·mol/kg), F is the Faraday constant (C/mol), z_i is the number of electrons involved in a redox reaction, and φ is the electric potential distribution (V) throughout the electrolyte. Recall that an incompressible fluid implies $\nabla\,\boldsymbol{u} = 0$. Equation (A7) is known as the Nernst–Planck equation.

The subscript i in Equation (A7) identifies a particular ionic species for which the equation is written. Thus, the number of ionic species involved in a reaction directly controls the number of equations to be solved—in general, oxidized and reduced species are involved. Thus, Equation (A7) yields i equations with $i + 1$ unknowns. To solve this system, more equations are needed, so Poisson's equation is added, which governs the distribution of the electrostatic potential throughout the system. Poisson's equation relates the potential distribution to the distribution of charged species within a medium:

$$-\,\nabla(\varepsilon\nabla\varphi)\;=\;\sum_i z_ie\,c_i \tag{A8}$$

where e is the elemental charge and ε is the permittivity of the medium. Here the medium is the electrolyte and the only charge carriers involved are the ions (species i). It is assumed that the solvated ions and electric field do not alter the permittivity of the electrolyte. The full set of Poisson–Nernst–Planck (PNP) equations are thus given by Equations (A7) and (A8) written for all ionic species under consideration.

CV experiments are usually performed at a high electrolyte concentration. Under this condition, the resistivity of the solution is sufficiently low that the electric field therein is negligible, and we can assume $\varphi = 0$ throughout the medium. In this circumstance, the PNP equations reduce to:

$$\frac{\partial c_i}{\partial t}+\boldsymbol{u}\nabla c_i-\nabla\left[D(\nabla c_i)\right]\;=\;0 \tag{A9}$$

For zero convection ($\boldsymbol{u} = 0$, no flow), no reaction (null electrode potential), and a constant diffusion coefficient, the simplified PNP Equation (A9) becomes Fick's second law of diffusion:

$$\frac{\partial c_i}{\partial t}\;=\;D\nabla^2c_i \tag{A10}$$

This is a partial differential equation that describes how the concentration of ionic species, i, evolves over time. For our case under consideration, where the electrolyte concentration is high, reactions are limited to the direction normal to the electrode surface and near the latter. As a result, the model simplifies further to one spatial dimension, x, over the domain $x = 0 - L$, the maximum extent of the diffusion layer. Boundary conditions are needed to obtain particular solutions to Equation (A10). For the case of one spatial variable x and time t, two boundary conditions in space at $x = 0$ (electrode position) and $x = L$ (bulk) are required, along with an initial condition at $t = 0$.

$$L\;=\;6\sqrt{Dt_{max}} \tag{A11}$$

A conservative value for L is set by the Cottrell equation to greatly exceed the mean diffusion layer thickness:

Where t_{max} is the period of the cyclic voltammogram. Thus, at $x = L$ we have:

$$c_i\,(x\;=\;L,t)\;=\;c_i^b \tag{A12}$$

where c_i^b is the bulk concentration of ionic species *i*.

At $x = 0$, Fick's first law, which describes the relationship between the diffusive flux and the concentration under steady-state conditions, must be satisfied for all *t*. In one spatial dimension, this law is written in the molar basis as:

$$\frac{k^{\circ}}{D}\exp\left(\frac{|\eta|}{b}\right)c_i^s \;=\; -\frac{\partial C_i}{\partial x}|_{x\,=\,0} \tag{A13}$$

where $c_i^s \;=\; c_i(x \;=\; 0,\; t)$ is the concentration of ionic species, *i*, at the electrode surface ($\mathrm{mol/m^3}$), k° is the rate constant at zero potential (m/s), η is the overpotential, and $b = RT/F$ is a constant. The potential E of the electrode through which a current flows differs from the equilibrium potential E° established when no current flows. The difference between these potentials is the overpotential $\eta = E - E^\circ$. To simplify the notation, the parameter μ is defined as $\mu = \frac{k^{\circ}}{D}\exp\left(\frac{|\eta|}{b}\right)$. Thus, Equation (A13) can be rewritten as:

$$\mu c_i^s \;=\; -\frac{\partial C_i}{\partial x}|_{x\,=\,0} \tag{A14}$$

The last boundary condition required is the initial condition applicable at $t = 0$ (before application of the potential), which holds for all x:

$$c_i\;(x, t \;=\; 0) \;=\; c_i^b \tag{A15}$$

Equation (A10) subject to boundary conditions (A12), (A14), and (A15) can be solved using the Laplace transform. Thus, considering a redox reaction involving one oxidized and one reduced species ($i = ox, red$), the concentration function of the oxidized species, $c_{ox}(x, t)$, has the following form:

$$\frac{c_{ox}(x,t)}{c_{ox}^b} \;=\; 1 - \mathrm{erfc}\left(\frac{x}{\sqrt{4Dt}}\right) + \exp\left(\mu x + \mu^2 Dt\right)\cdot\mathrm{erfc}\left(\frac{x}{\sqrt{4Dt}} + \mu\sqrt{Dt}\right) \tag{A16}$$

The concentration of the reduced species, $c_{red}(x, t)$, has a similar form.

References

1. Bolotsky, A.; Butler, D.; Dong, C.; Gerace, K.; Glavin, N.R.; Muratore, C.; Robinson, J.A.; Ebrahimi, A. Two-dimensional materials in Biosensing and Healthcare: From in virto diagnostic to optogenetics and beyond. *ACS Nano* **2019**, *13*, 9781–9810. [CrossRef]
2. Tencer, M.; Nie, H.-Y.; Berini, P. Electrochemical differentiation and TOF-SIMS characterization of thiol-coated gold features for (bio) chemical sensor applications. *J. Electrochem. Soc.* **2009**, *156*, J386. [CrossRef]
3. Tencer, M.; Olivieri, A.; Tezel, B.; Nie, H.-Y.; Berini, P. Chip-scale electrochemical differentiation of SAM-coated gold features using a photo array. *J. Electrochem. Soc.* **2012**, *159*, J77. [CrossRef]
4. Fong, N.R.; Menotti, M.; Lisicka-Skrzek, E.; Northfield, H.; Olivieri, A.; Tait, R.N.; Liscidini, M.; Berini, P. Bloch long-range surface plasmon polaritons on metal strip waveguides on a multilayer substrate. *ACS Photonics* **2017**, *4*, 593–599. [CrossRef]
5. Khodami, M.; Berini, P. Grating couplers for (Bloch) long-range surface plasmons on metal strip waveguides. *J. Opt. Soc. Am. B* **2019**, *36*, 1921–1930. [CrossRef]
6. Hirbodvash, Z.; Khodami, M.; Fong, N.R.; Lisicka-Skrzek, E.; Olivieri, A.; Northfield, H.; Tait, R.N.; Berini, P. Grating couplers fabricated by e-beam litography for long-range surface plasmon waveguides embedded in a fluoropolymer. *Appl. Opt.* **2019**, *58*, 2294–3002. [CrossRef]
7. Khodami, M.; Hirbodvash, Z.; Krupin, O.; Wong, W.R.; Lisicka-Skrzek, E.; Northfield, H.; Hahn, C.; Berini, P. Fabrication of Bloch long range surface plasmon waveguides integrating counter electrodes andmicrofludic chammels for multimodal biosensing. *J. Microelectromech. Syst.* **2021**, *30*, 686–695. [CrossRef]
8. Berini, P. Long-range surface plasmon polaritons. *Adv. Opt. Photonics* **2009**, *1*, 484–588. [CrossRef]
9. Miyazaki, C.; Shimizu, F.M.; Ferreira, M. Surface plasmon resonance (SPR) FOR sensors and biosensors. In *Nanocharacterization Techniques*; Elsevier: Norwich, CT, USA, 2017; pp. 183–200.
10. Lopez, F.; Pichereaux, C.; Burlet-Schiltz, O.; Pradayrol, L.; Monsarrat, B.; Esteve, J.P. Improved sensitivity of biomolecular interaction analysis mass spectrometry for the identification of interacting molecules. *Proteomics* **2003**, *3*, 402–412. [CrossRef]
11. Zalewska, M.; Kochman, A.; Esteve, J.P.; Lopez, F.; Chaoui, K.; Susini, C.; Ozyhar, A.; Kochman, M. Juvenile hormone binding protein traffic-Interaction with ATP synthase and lipid transfer proteins. *Biochim. Biophys. Acta Biomembr.* **2009**, *1788*, 1695–1705. [CrossRef]

12. Dausse, E.; Barré, A.; Aimé, A.; Gropp, A.; Rico, A.; Ainali, C.; Salgado, G.; Palau, W.; Daguerre, E.; Nikolski, M.; et al. Aptamer selection by direct microfluidic recovery and surface plasmon resonance evaluation. *Biosens. Bioelectron.* **2016**, *80*, 418–425. [CrossRef] [PubMed]
13. Gordon II, J.G.; Ernst, S. Surface plasmons as a probe of the electrochemical interface. *Surf. Sci.* **1980**, *101*, 499–506. [CrossRef]
14. Huang, X.; Wang, S.; Shan, X.; Chang, X.; Tao, N. Flow-through electrochemical surface plasmon resonance: Detection of intermediate reaction products. *J. Electroanal. Chem.* **2010**, *649*, 37–41. [CrossRef]
15. Ribeiroa, J.A.; Sales, M.G.F.; Pereira, C.M. Electrochemistry-assisted surface plasmon resonance detection of miRNA-145 at femtomolar level. *Sens. Actuators B* **2020**, *7*, 128129. [CrossRef]
16. Sannomia, T.; Dermutz, H.; Hafner, C.; Voros, J.; Dahilin, A.B. Electrochemistry on a localized surface plasmon resonance sensor. *Langmuir* **2010**, *26*, 7619–7626. [CrossRef]
17. Steinhauser, B.; Vidal, C.; Barb, R.A.; Heitz, J.; Mardare, A.I.; Hasset, A.W.; Hrelescu, C.; Klar, T.A. Localized-plasmon voltammetry to detect PH dependent gold Oxidation. *J. Phys. Chem. C* **2018**, *122*, 4565–4571. [CrossRef]
18. Guo, T. Fiber grating-assisted surface plasmon resonance for biochemical and electrochemical sensing. *J. Lightw. Technol.* **2017**, *35*, 3323–3333. [CrossRef]
19. Yuan, Y.; Guo, T.; Qiu, X.; Tang, J.; Huang, Y.; Zhuang, L.; Zhou, S.; Li, Z.; Guan, B.; Zhang, X.; et al. Electrochemical surface plasmon resonance fiber-optic sensor: In situ detection of electroactive biofilms. *Anal. Chem.* **2016**, *88*, 7609–7616. [CrossRef]
20. Yua, J.; Jia, P.; Wang, S.; Ebendorff-Heidepriem, H.; Abell, A.D. Electrochemical plasmonic optical fiber probe for real-time insight into coreactant electrochemiluminescence. *Sens. Actuators B* **2020**, *321*, 128469. [CrossRef]
21. Abanulo, J.C.; Harris, R.D.; Sheridan, A.K.; Wilkinson, J.S.; Bartlett, P.N. Waveguide surface plasmon resonance studies of surface reactions on gold electrodes. *Faraday Discuss.* **2002**, *121*, 139–152. [CrossRef]
22. Piraud, C.; Mwarania, E.; Wylangowski, G.; Wilkinson, J.; O'Dwyer, K.; Schiffrin, D.J. An optoelectrochemical thin-film chlorine sensor employing evanescent fields on planar optical waveguides. *Anal. Chem.* **1992**, *64*, 651–655. [CrossRef]
23. Baba, A.; Taranekar, P.; Ponnapati, R.R.; Knoll, W.; Advincula, R.C. Electrochemical surface plasmon resonance and waveguide enhanced glucose biosensing with N-Alkylaminated polypyrrole/glucose oxidase multilayers. *ACS Appl. Mater. Interfaces* **2010**, *2*, 2347–2354. [CrossRef] [PubMed]
24. Al-Zubeidi, A.; Hoener, B.S.; Collins, S.S.E.; Wang, W.; Kirchner, S.R.; Jebeli, S.A.H.; Joplin, A.; Chang, W.S.; Link, S.; Landes, C.F. Hot holes assist plasmonic nanoelectrode dissolution. *Nano Lett.* **2019**, *19*, 1301–1306. [CrossRef]
25. Shin, H.H.; Koo, J.J.; Lee, K.S.; Kim, Z.H. Chemical reactions driven by plasmon induced hot carriers. *Appl. Mater. Today* **2019**, *16*, 112–119. [CrossRef]
26. Jang, Y.H.; Jang, Y.J.; Kim, S.; Quan, L.N.; Chung, K.; Kim, D.H. Plasmonic solar cells: From rational design to mechanism overview. *Chem. Rev.* **2016**, *116*, 14982. [CrossRef] [PubMed]
27. Atwater, H.A.; Polman, A. Photonic design principles for ultrahigh-efficiency photovoltaics. *Nat. Mater.* **2012**, *11*, 174–177.
28. Power, A.C.; Morrin, A. Electroanalytical sensor technology. In *Electrochemistry*; Khalid, M.A.A., Ed.; InTech: Rijeka, Croatia, 2013; pp. 141–178.
29. Grieshaber, D.; MacKenzie, R.; Vörös, J.; Reimhult, E. Electrochemical biosensors-sensor principles and architectures. *Sensors* **2008**, *8*, 1400–1458. [CrossRef]
30. Young, D.; Christou, A. Failure mechanism models for electromigration. *IEEE Trans. Reliab.* **1994**, *43*, 186–192. [CrossRef]
31. Tu, K.N. Recent advances on electromigration in very-large-scale-integration of interconnects. *J. Appl. Phys.* **2003**, *94*, 5451–5473. [CrossRef]
32. Oates, A.S. Electromigration transport mechanisms in Al thin-film conductors. *J. Appl. Phys.* **1996**, *79*, 163–169. [CrossRef]
33. Arslan, F.; Beska, U. An amperometric biosensor for glucose detection from glucose oxidase immobilized in polyaniline-polyvinylsulfonate- potassium ferricyanide film. *Artif. Cells Nanomed. Biotechnol.* **2014**, *42*, 284–288. [CrossRef]
34. Lamas-Ardisana, P.J.; Martínez-Paredes, G.; Añorga, L.; Grande, H.J. Glucose biosensor based on disposable electrochemical paper-based transducers fully fabricated by screen printing. *Biosens. Bioelectron.* **2018**, *109*, 8–12. [CrossRef]
35. Dickinson, E.J.; Petersen, J.L.; Rees, N.V.; Compton, R.G. How much supporting electrolyte is required to make a cyclic voltammetry experiment quantitatively 'difffusional'? *J. Phys. Chem. C* **2009**, *113*, 11157–11171. [CrossRef]
36. Yun, C.; Hwang, S. Analysis of the charging current in cyclic voltammetry and supercapacitor's galvanostatic charging profile based on a constant-phase element. *ACS Omega* **2021**, *6*, 367–373. [CrossRef] [PubMed]
37. Konopka, S.J.; McDuffie, B. Diffusion coefficients of ferri- and ferrocyanide ions in aqueous media, using twin-electrode thin layer electrochemistry. *Anal. Chem.* **1970**, *42*, 1741–1746. [CrossRef]
38. Wang, J.; Zhang, Z. *Analytical Chemistry*; Trans. Tech. Publ.: Zurich, Switzerland, 1994; pp. 3–66.
39. Compton, R.G.; Banks, C.E. *Understanding Voltammetry*; World Scientific: Singapore, 2018.
40. Bard, A.J.; Faulkner, L.R. *Electrochemical Methods: Fundamentals and Applications*; Wiley: New York, NY, USA, 1983; Volume 20, pp. 91–92.
41. Zheng, Q.; Wei, G.W. Piosson-boltzmann-nernst-planck model. *J. Chem. Phys.* **2011**, *134*, 194101. [CrossRef]
42. Guidelli, R.; Compton, R.G.; Feliu, J.M.; Gileadi, E.; Lipkowski, J.; Schmickler, W.; Trasatti, S. Definition of the transfer coefficient in electrochemistry (IUPAC Recommendations 2014). *Pure Appl. Chem.* **2014**, *86*, 259–262. [CrossRef]

Chapter 5.

LRSPPs and Energetic Carriers

5.1. Summary

Plasmonic catalysis opens new reaction pathways that are inaccessible thermally, or improves chemical processes by improving the efficiency. In the present work, we use a stripe of Au as a waveguide that supports infrared surface plasmon polaritons (SPPs), which also functions as a working electrode in a 3-electrode electrochemical cell. Cyclic voltammograms were obtained under SPP excitation as a function of incident optical power and wavelength. By studying oxidation and reduction reactions separately, processes involving energetic holes are separated from the processes involving energetic electrons. SPP excitation increases redox current density by 10×. Beyond a threshold with SPP power, oxidation, reduction, and equilibrium potentials drop by as much as 2× and split in correlation with the photon energy. Under SPP excitation, the electrochemical impedance spectroscopy reveals a drop in charge transfer resistance of almost 2×. The temperature of the working electrode is monitored in situ under SPP excitation and independent control experiments are performed to isolate thermal effects. Chronoamperometry measurements, with SPPs modulated at 600 Hz, yield a rapid current response modulated at the same frequency, excluding thermally enhanced mass transport.

5.2. Contribution

In this chapter, results are presented that are published in Science Advances. Zohreh Hirbodvsh carried out the optical and electrochemical experiments, contributed to the measurement interpretation, and prepared the first draft of the manuscript. Oleksiy Krupin assisted with the measurements and interpretation. Howard Northfield and Anthony Olivieri fabricated the waveguide structures tested. Dr. Baranova assisted with the experimental techniques and the interpretation of the measurements. Dr. Berini carried out the mode computations and directed the research. All Authors contributed to writing the manuscript.

5.3. Article

The article follows here verbatim.

CHEMISTRY

Infrared surface plasmons on a Au waveguide electrode open new redox channels associated with the transfer of energetic carriers

Zohreh Hirbodvash[1,2], Oleksiy Krupin[2]†, Howard Northfield[2], Anthony Olivieri[2], Elena A. Baranova[3,4], Pierre Berini[1,2,5]*

Plasmonic catalysis holds promise for opening new reaction pathways inaccessible thermally or for improving the efficiency of chemical processes. We report a gold stripe waveguide along which infrared ($\lambda_0 \sim 1350$ nanometers) surface plasmon polaritons (SPPs) propagate, operating simultaneously as an electrochemical working electrode. Cyclic voltammograms obtained under SPP excitation enable oxidative processes involving energetic holes to be investigated separately from reductive processes involving energetic electrons. Under SPP excitation, redox currents increase by 10×, redox potentials decrease by ~2× and split in correlation with photon energy, and the charge transfer resistance drops by ~2× as measured using electrochemical impedance spectroscopy. The temperature of the working electrode was monitored in situ, ruling out thermal effects. Chronoamperometry measurements with SPPs modulated at 600 hertz yield a commensurately modulated current response, ruling out thermally enhanced mass transport. Our observations indicate opening of optically controlled nonequilibrium redox channels associated with energetic carrier transfer to the redox species.

INTRODUCTION

Surface plasmon polaritons (SPPs) on metal surfaces have useful properties, such as strong field enhancement and subwavelength localization (*1*), which have long-driven vigorous interest in these waves. SPPs are damped by absorption in the metal (*2*), which limits their propagation length and lifetime. However, the absorption of SPPs creates energetic carriers (cf. hot electrons and holes) along the surface of the metal (*3*), which can be exploited in device applications or in catalysis (*4–7*), thereby turning what is often viewed as a drawback into a benefit. This route for creating energetic carriers is particularly compelling, given the high efficiency with which SPPs can be excited optically. These attributes drive research on plasmonic catalysis, motivated by a desire to open reaction pathways that are inaccessible thermally or to improve the efficiency of chemical processes by involving energetic carriers.

A metal surface supporting SPPs can double as a working electrode (WE) within an electrochemical cell. These electrodes have been constructed as a metal film on a prism in the Kretschmann configuration (*8*, *9*) or as metal nanoparticles on a conductive substrate (*10*, *11*). Redox reactions occurring on the surface of an electrode can be probed using SPPs localized thereon, revealing subtle details of reactions. For instance, SPPs were used to image the local current density directly on a planar WE (*8*). Alternatively, the optical performance of plasmonic structures can be tuned electrochemically, e.g., by shifting the SPP resonance of Au nanorods via charge injection (*11*). Electrochemical cells that incorporate plasmonic structures are also of interest as multimodal chemical transducers (*9*, *12*).

Recently, attention has turned to investigating the role played by energetic carriers created by SPP absorption in electrochemical reactions (*13*). Advantageously, redox currents are easily measured, proportional to reaction rates, and directly connected to experimental conditions, including plasmonic effects. Furthermore, processes involving energetic holes can be separated from processes involving energetic electrons by investigating oxidation or reduction reactions separately.

The creation of energetic carriers via SPP absorption invariably causes the temperature of the metal to rise, with heat diffusing into the nearby reaction volume. Given that chemical reactions are temperature dependent, separating the roles of temperature and energetic carriers is not trivial but essential to proper interpretation of results (*14–18*).

Empirically and in general, a reaction rate K increases exponentially with temperature following the Arrhenius law (*15*, *16*, *18*): $K = A \cdot \exp[-E_a/(R(T_0 + cI))]$, where E_a is the molar activation energy, R is the gas constant, T_0 is the nominal temperature, c is a photothermal conversion coefficient, and A is a constant depending on the reaction. It is generally a good assumption that the temperature of a plasmonic structure increases linearly with incident intensity ($T \propto cI$) as long as the optical response remains linear. Conversely, the reaction rate should depend linearly on optical intensity if energetic carriers play a role because their number is proportional to the number of SPP quanta absorbed, which depends on the number of incident photons (intensity). In principle, the roles of temperature and energetic carriers can be distinguished by varying the intensity and observing whether the reaction rate evolves exponentially or linearly (respectively). However, this approach has pitfalls. For instance, an exponential appears linear for small changes in argument (cf. Taylor series), so experiments involving small intensity changes could imply an incorrect trend.

In electrochemical systems, increasing electrode and electrolyte temperature affects the equilibrium potential and electron transfer

---

[1]Department of Physics, University of Ottawa, 150 Louis Pasteur, Ottawa, ON K1N 6N5, Canada. [2]Center for Research in Photonics, University of Ottawa, 25 Templeton St., Ottawa, ON K1N 6N5, Canada. [3]Department of Chemical and Biological Engineering, University of Ottawa, 161 Louis-Pasteur, Ottawa, ON K1N 6N5, Canada. [4]Centre for Catalysis Research and Innovation, University of Ottawa, 161 Louis-Pasteur, Ottawa, ON K1N 6N5, Canada. [5]School of Electrical Engineering and Computer Science, University of Ottawa, 800 King Edward Ave., Ottawa, ON K1N 6N5, Canada.
*Corresponding author. Email: berini@eecs.uottawa.ca
†Present address: Abbott Point of Care, 185 Corkstown Rd., Nepean, ON K2H 8V4, Canada.

rates to/from the redox species and leads to convection that works to cool the system and enhance mass transport to the electrode (*19–23*). Thermal modeling, including diffusion, convection, and mass transport (*21*), predicts an approximately linear increase in redox currents with heating power ($i \propto P^a$, $a = 0.8$ to 1) rather than exponential (as might be expected from the Arrhenius law), and a current rise time of at least 10 s upon onset of heating. Trends with temperature are not straightforward, so electrochemical cells should be thermally stabilized, the electrode temperature should be monitored, independent thermal control experiments carried out, and optical variables in addition to intensity should be varied to separate the role of temperature from that of energetic carriers.

Much of the work carried out to date in plasmonic catalysis involved colloidal arrangements of Au nanoparticles illuminated at visible wavelengths (e.g., $\lambda_0 = 532$ nm, $h\upsilon = 2.33$ eV) (*4–7*, *13*). This scenario, although convenient, poses challenges. For instance, the temperature in the immediate vicinity of nanoparticles can be difficult to predict and measure because of collective effects (*16*). In addition, carriers excited in Au at wavelengths above the interband threshold ($h\upsilon \sim 2$ eV) have very short lifetimes (because of electron-electron scattering at high carrier energies) (*24*).

High energy carriers ($h\upsilon > 2$ eV) are generally deemed essential to catalyze reactions via SPPs. Contrary to this broadly held view, we use here lower-energy infrared photons ($\lambda_0 \sim 1350$ nm, $h\upsilon \sim 1$ eV) to excite SPPs and energetic carriers in Au. Under this excitation, the carriers have energies at most 1 eV above E_F, and longer lifetimes, or longer attenuation lengths ($L_e \sim 74$ nm, $L_h \sim 55$ nm) (*25*), as the main carrier damping mechanism is electron-phonon scattering. Furthermore, we use a thin Au stripe as an SPP waveguide and WE, which offers several advantages over colloidal nanoparticles: The WE is defined lithographically and is well understood structurally. The temperature of the WE under SPP excitation is determined in situ using calibrated resistance measurements. SPPs propagate over the entire length of the WE with exclusive and complete overlap. Last, the thickness of the WE (t) is less than the excited carrier attenuation lengths in Au (L_e, L_h), enabling multiple internal carrier reflections that enhance their escape probability (26).

RESULTS

Metallic structures were fabricated on a multilayer substrate, as shown in Fig. 1, using standard nanofabrication techniques (*27*, *28*). Figure 1A gives a microscope image of a Au stripe designed to operate simultaneously as an SPP waveguide and WE. The image also shows a nearby Pt stripe used as a counter electrode (CE) and thick contact pads (>200 nm) for electrical probing. The chip is immersed in a petri dish filled with the redox species in electrolyte in which a Ag/AgCl reference electrode is dipped, thereby forming a three-electrode electrochemical cell. Glycerol was added to the electrolyte to adjust its refractive index ($n = 1.3325$, $\lambda_0 = 1312$ nm), as the solution also acts as the upper cladding of the SPP waveguide. The petri dish was mounted on a thermoelectric cooler (TEC) driven by a temperature controller using an electronic thermometer dipped in the electrolyte for feedback control. Unless stated otherwise, the bulk electrolyte temperature was maintained constant to 20°C during all experiments. (cf. Materials and Methods and fig. S1).

Figure 1B illustrates the geometry of the electrodes, including their dimensions. The design of the Pt stripe (CE) is identical to that of the Au stripe (WE). Both are $t = 35$ nm thick ($<L_e$, L_h in Au) and were deposited on 0.3 nm of Ti as an adhesion layer.

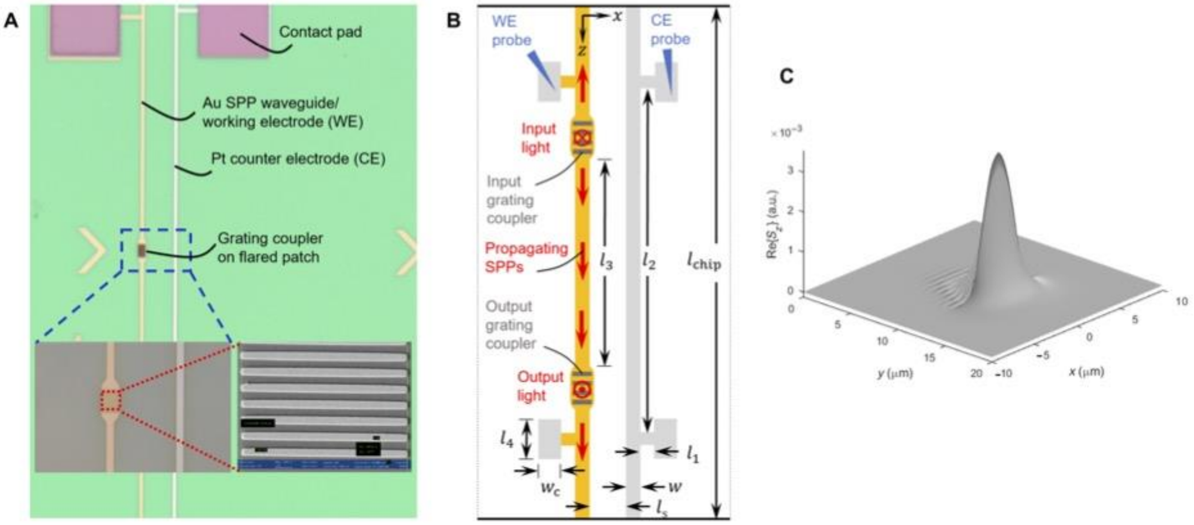

Fig. 1. Plasmonic waveguide and electrodes. (**A**) Microscope image in top view of a chip bearing Au SPP waveguides/WEs, Pt CEs, Au grating couplers, and electrical contact pads on a multilayer substrate (appears green under bright-field optical microscopy). The bottom insets show scanning electron microscope (SEM) images of a grating coupler. (**B**) Geometry of the electrodes in top view: $l_1 = 29$ μm, $l_2 = 2600$ μm, $l_3 = 1850$ μm, $l_4 = 250$ μm, $l_{chip} = 3000$ μm, $w_c = 100$ μm, $w = 5$ μm, and $l_s = 40$ μm. The thickness of both electrodes (along y) is $t = 35$ nm. Experimental scheme: The WE and CE are contacted using external probes to form a three-electrode electrochemical system with an Ag/AgCl reference electrode. Input laser light, normally incident on the input grating coupler, excites SPPs that propagate along the WE. The output grating coupler converts the SPPs to output light emerging normally from the chip, which is captured and measured. (**C**). Computed distribution of Re{S_z}, where S_z is the component of the Poynting vector (proportional to mode intensity) in the direction of propagation (along z). a.u., arbitrary units.

The geometry of the WE is constrained by its dual use as an SPP waveguide. The substrate is a multilayer stack, consisting of 15 periods of alternating layers of SiO_2/Ta_2O_5, as a truncated one-dimensional photonic crystal, on a Si wafer. Bloch long-range SPPs (*27–29*) propagate over the full length of the Au stripe, with a field distribution that surrounds the stripe—this is a key attribute of the structure as SPPs overlap exclusively and completely the WE. Figure 1C shows the distribution of $\mathrm{Re}\{S_z\}$ of this mode, where S_z is the component of the Poynting vector in the direction of propagation (z) and is proportional to the mode intensity. The computation was carried out using the method of lines, as described under Materials and Methods.

The bottom insets in Fig. 1A show scanning electron microscope (SEM) images of a grating coupler, as used for optical input and output coupling to Bloch long-range SPPs using perpendicular optical fibers (*27–29*). The experimental scheme is illustrated in Fig. 1B (cf. Materials and Methods and fig. S1). Advantageously, the arrangement in transmission enables optimization in situ of both optical alignments.

Once optical alignments were established, the laser wavelength was swept over the range of 1300 to 1370 nm, while the output optical power was monitored (fig. S2). The output power was maximum over the 1330- to 1370-nm range, which agrees well with the design wavelength of the grating couplers and waveguide (*28*, *29*). Three operating wavelengths were used for the experiments: 1330, 1350, and 1370 nm.

All experiments were carried out with 0.5 mM $K_3[Fe(CN)_6]$ + 100 mM KNO_3 electrolyte, using a triangular potential waveform at a scan rate of 100 mV/s. Applying such a potential to the system leads to the chemically reversible reaction of potassium ferricyanide $\{K_3[Fe(CN)_6]\}$ to potassium ferrocyanide $\{K_4[Fe(CN)_6]\}$ as a redox couple in a one-electron transfer process

$$K_4[Fe(CN)_6] \leftrightarrow K_3[Fe(CN)_6] + e^-$$

Cyclic voltammetry (CV) was carried out on a Au WE, without optical illumination, providing a reference CV curve. CV was then carried out under the same conditions but with SPPs propagating along the Au WE as a function of incident optical power (intensity) and wavelength. The output optical power was monitored during all experiments. The measured CV curves, shown in Fig. 2A for

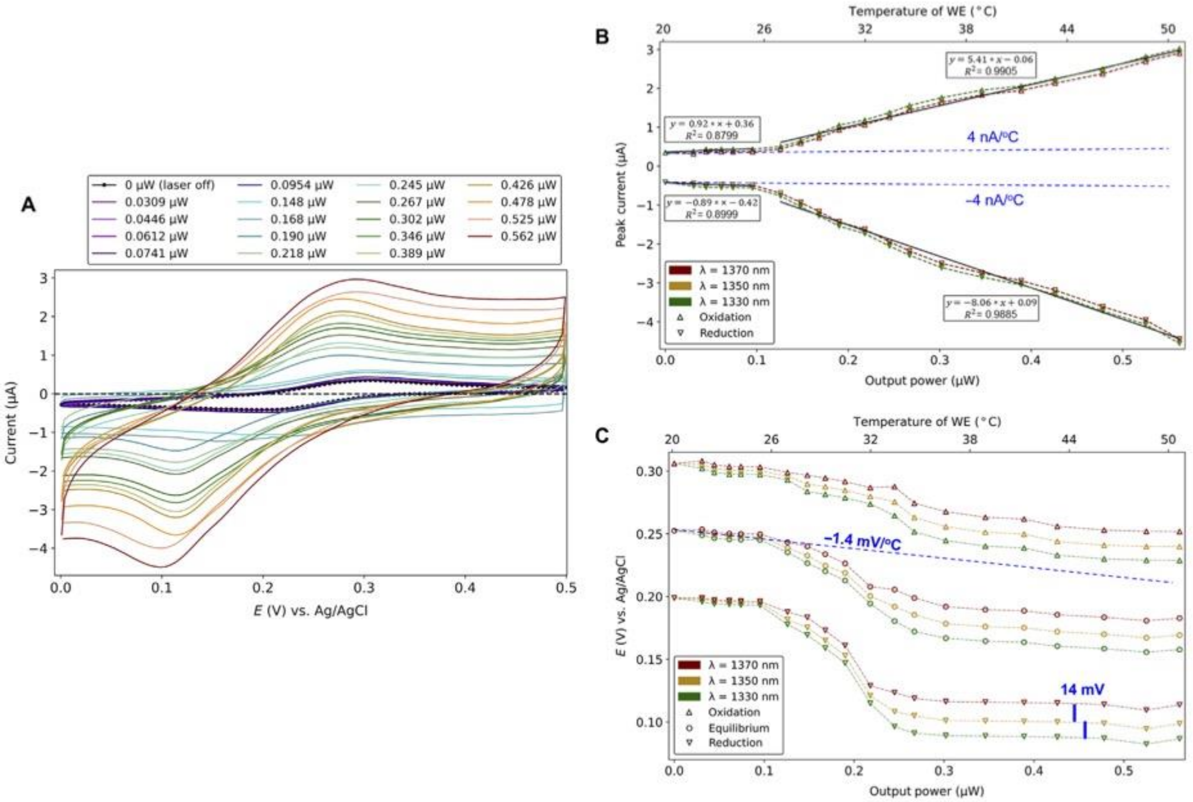

Fig. 2. CV under optical illumination. (**A**) CV curves obtained on a Au WE, in 0.5 mM $K_3[Fe(CN)_6]$ + 100 mM KNO_3 electrolyte, at a scan rate of 100 mV/s, for increasing output optical power (legend) at $\lambda_0 = 1350$ nm. The incident optical power ranged from 0 to 6.3 mW. The reference CV curve (laser off) is plotted in black dots. (**B**) Redox current peaks, and (**C**) potentials versus output optical power, from CV curves measured at $\lambda_0 = 1330$, 1350, and 1370 nm. Linear models of the peak redox currents at $\lambda_0 = 1350$ nm are plotted as the solid black lines in (B) (slopes have units of amperes per watt). The solid vertical blue bars in (C) measure 14 mV, corresponding to the approximate photon energy separating the three optical wavelengths (~14 meV). Linear thermal trends, measured independently, are added as the blue dashed lines to (B) and (C).

λ_0 = 1350 nm, change markedly as the optical power increases. The CV curves for λ_0 = 1330 and 1370 nm show similar changes (fig. S3).

The current increases significantly with optical power compared to the reference case (no illumination). Figure 2B plots the peak oxidation and reduction currents versus the output optical power for the three wavelengths of interest, revealing an increase of ~10× in both over the power range investigated. The reduction current increases more than the oxidation current. A clear threshold is observed in Fig. 2B at an output power of ~0.1 μW, about which different linear trends are evident. Linear models of peak current versus output optical power, fitted for each segment at λ_0 = 1350 nm, are plotted as the solid black lines and given in the corresponding legends.

The potentials corresponding to the peak redox currents also change significantly with optical power, as shown in Fig. 2C. The reduction potential decreases by ~2×, the oxidation potential by ~1.3×, and the equilibrium potential (mean of the redox potentials) by ~1.7× relative to the Ag/AgCl reference electrode. Again, a clear threshold is observed at an output power of ~0.1 μW. Beyond threshold, the redox potentials decrease commensurately with increasing photon energy: $\Delta(h\upsilon)$ = 13.8 meV separates λ_0 = 1330 from 1350 nm, and $\Delta(h\upsilon)$ = 13.4 meV separates λ_0 = 1350 from 1370 nm; vertical blue bars of 14 mV on Fig. 2C illustrate this point.

The resistance of the WE was measured in situ as a function of optical power and compared to calibrated resistances to determine its temperature (fig. S4). The temperature of the WE, added to Fig. 2 (B and C) as the top horizontal scale, spans about 30°C.

Various control experiments were carried out in situ under identical experimental conditions, as described in the text that follows. Control experiments without the redox species produced featureless and noisy CV curves whether the illumination was on or off (fig. S5).

Control experiments with the laser on while misaligning the input optical fiber (in various ways) were carried out. The CV curves would always return to the reference case (no illumination) as soon as coupling to the input grating was lost, confirming that the excitation of SPPs on the WE was essential to the changes observed in Fig. 2.

Temperature control experiments without illumination were carried out using the TEC placed under the petri dish to cool then heat the entire cell (electrodes and electrolyte) in a uniform and controlled manner. CV curves obtained at different temperatures, ranging from 10° to 40°C, show changes in peak redox currents of about 30%, following linear trends with temperature of fitted slopes ±4 nA/°C, consistent with thermally induced mass-transport effects (fig. S6) (*21*). The reduction and oxidation potentials change by 10 to 20%. The temperature dependence of the equilibrium potential was fit to a linear model yielding a slope of −1.4 mV/°C, in good agreement with thermally induced shifts reported in the literature for the ferricyanide/ferrocyanide system (*19*, *30*–*32*). Linear thermal trends based on these measurements were added to Fig. 2 (B and C) as the dashed blue lines.

Further temperature control experiments without illumination were carried out by directly heating the WE resistively through current injection while maintaining the bulk electrolyte temperature to 20°C (cf. Materials and Methods and fig. S7). By resistively heating the WE, a thermal gradient is produced in the electrolyte, resembling closely the heat gradient produced by absorption of the propagating SPPs. CV curves obtained while directly heating the WE to temperatures ranging from 20° to 50°C (fig. S8) are very similar to those obtained by heating the entire cell in a uniform manner (fig. S6), including the linear thermal trends for the peak redox currents and the equilibrium potential (legends). Thus, small thermal gradients in our system, generated resistively or optically, do not have a significant impact on the results.

Thermally induced mass transport effects were further ruled out by taking chronoamperometry measurements, while the laser was internally modulated on/off at a frequency of 600 Hz (period of 1.67 ms). The inset in Fig. 3A shows the time response of the modulated laser power measured using a photoreceiver. The modulation frequency of 600 Hz is low enough to enable our potentiostat to reliably acquire several current samples (8) within a modulation period (1.67 ms), yet high enough to preclude thermally induced mass transport, which occurs on time scales of the order of seconds (*21*).

The chronoamperometric response is shown in Fig. 3A. A forward step potential of 450 mV (versus Ag/AgCl) was applied from a null potential to induce oxidation of the redox species at the Au WE, while the latter supports on/off modulated propagating SPPs. The incident laser power was modulated from 0 (off-state) to 6.3 mW (on-state), corresponding to the incident power extrema investigated

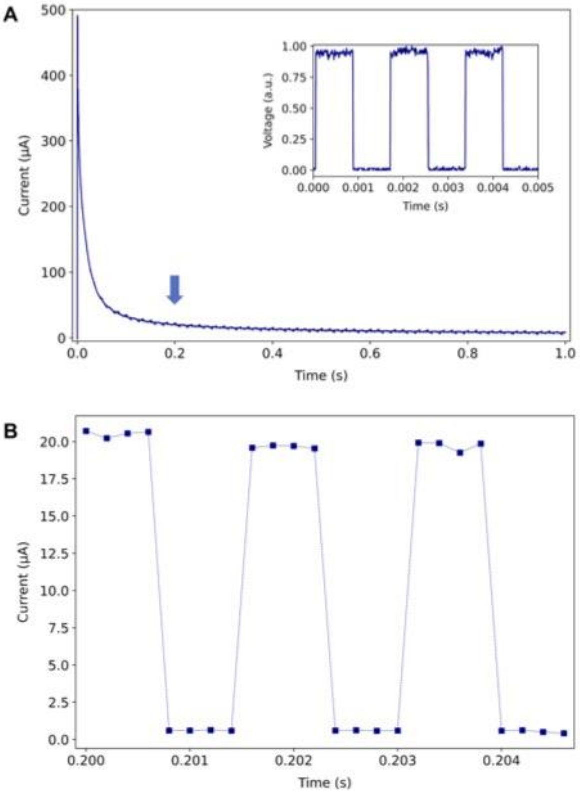

Fig. 3. Chronoamperometry under optical modulation. (**A**) Chronoamperometric response on a Au WE to a 450-mV potential step (versus Ag/AgCl), in .5 mM $K_3[Fe(CN)_6]$ + 100 mM KNO_3 electrolyte, for on/off laser modulation. The inset shows the on/off laser modulation response measured using a photo receiver (modulation frequency of 600 Hz, period of 1.67 ms). (**B**) Zoom-in of the chronoamperometric response in the Cottrell region at the location of the blue arrow sketched in (A), resolved as eight current samples per period.

in Fig. 2. The current response of Fig. 3A was plotted versus $t^{-1/2}$ for the purpose of identifying the region where it decays following the Cottrell equation, indicating diffusion-limited conditions. Figure 3B plots a zoom-in of the chronoamperometric response in the Cottrell region, at the location of the blue arrow sketched in Fig. 3A, revealing a periodic response tracking in time of the laser modulation shown in the inset of Fig. 3A. The current during the laser off-state is unmeasurable (below the noise floor of our instrument), but the current during the on-state has a high signal-to-noise ratio. Recalling that thermally induced mass transport occurs over time scales of seconds rules out this process as being responsible for the increase in current.

Electrochemical impedance spectroscopy (EIS) (*33*) measurements were also performed with SPPs propagating along the Au WE, as a function of incident optical power, at $\lambda_0 = 1350$ nm. EIS was carried out over the frequency range from 100 kHz to 1 Hz, with an

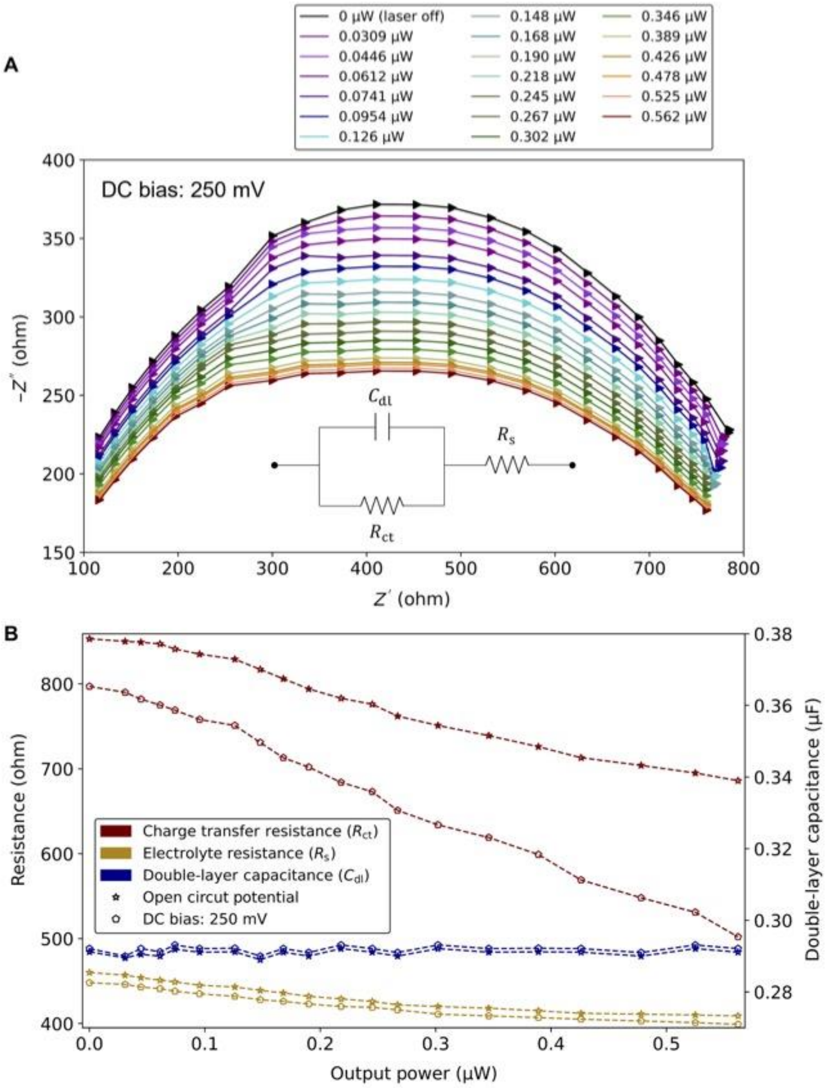

Fig. 4. EIS under optical illumination. (**A**) Electrochemical impedance frequency responses, measured on a Au WE, in 0.5 mM $K_3[Fe(CN)_6]$ + 100 mM KNO_3 electrolyte, for increasing output optical power (legend) at $\lambda_0 = 1350$ nm. The reference impedance response (laser off) is plotted in black. The AC potential amplitude was set to 5 mV root mean square, and the DC bias (polarization) was set to 250 mV (both versus Ag/AgCl). The impedance responses are plotted over the frequency range 100 to 3 kHz as Nyquist plots ($Z = Z' + iZ''$). The inset shows the simplified Randle circuit composed of C_{dl} (double layer capacitance), R_{ct} (charge transfer resistance), and R_s (electrolyte resistance). (**B**) Extracted Randle circuit parameters (R_{ct}, C_{dl}, and R_s) versus output optical power under open-circuit conditions (stars) and a DC bias of 250 mV (versus Ag/AgCl) (circles).

AC amplitude of 5 mV root mean square (versus Ag/AgCl), under open-circuit and DC-biased (polarized) conditions (see Materials and Methods). The DC bias was set to 250 mV (versus Ag/AgCl), close to the oxidation peak observed on Fig. 2A. Nyquist plots were produced from the impedance responses, and all plots could be separated into three regions (*33*): a semicircle at high frequencies, an approximately diagonal linear trend at intermediate frequencies, and an approximately vertical linear trend at low frequencies, as can be observed in fig. S9A for the open-circuit case under no illumination.

The semicircles change significantly with optical power compared to the references (no illumination), as observed in Fig. 4A for the biased case and in fig. S9B for the open-circuit case. The impedance response of the simplified Randle equivalent circuit, shown in the inset of Fig. 4A, was fit to each semicircle of Fig. 4A and fig. S9B. The fitting frequency range was 100 to 3 kHz, which covers the range over which the semicircles are plotted. The circuit parameters of the Randle model remained unconstrained during fitting. The R^2 goodness of fit was better than 0.91 over all cases. The extracted circuit parameters of the Randle model are plotted in Fig. 4B versus the output optical power. As observed, the charge transfer resistance, R_{ct}, decreases significantly with increasing optical power for both cases and by almost 2× for the biased case. Conversely, the double layer capacitance, C_{dl}, and the electrolyte resistance, R_s, remain comparatively constant with optical power (the small decrease in R_s may be due to the small increase in WE temperature with increasing optical power; cf. fig. S4C).

DISCUSSION

We interpret the enhancements observed in the redox currents (Figs. 2 and 3) and the drop in charge transfer resistance (Fig. 4) due to energetic carriers created along the Au WE, as SPPs propagate and are absorbed therein. Energetic electrons transfer from the WE to the redox species enhancing the reduction current, and energetic holes transfer to enhance the oxidation current—both are required to explain the results observed in Fig. 2B.

The power threshold behavior observed in Fig. 2B indicates the opening of redox channels associated with energetic carrier transfer, as these channels overcome noise in the system and the equilibrium redox currents become dominant. Beyond threshold, both trends are linear with optical power, as expected for an effect based on energetic carriers. Thermal effects on the redox currents are also linear but follow much weaker trends as noted from the measured thermal trend lines added to Fig. 2B (dashed blue). Although peak currents in CV measurements incorporate electron transfer and mass transport effects, it is clear that SPPs affect primarily electron transfer processes through the creation of energetic carriers.

The creation of energetic carriers causes the oxidation and reduction potentials to decrease significantly relative to Ag/AgCl, as observed in Fig. 2C, well beyond the thermal trend line for the equilibrium potential (dashed blue). The decrease (negative shift) to lower potentials for the oxidation reaction implies that it is easier to drive because of energetic holes, but the decrease (also a negative shift) in the reduction potential implies the opposite for energetic electrons. The difference between the peak redox potentials does not decrease with optical power as might be expected for energetic carriers of both types. This is explained by the fact that our system is electrochemically quasi-reversible (although the redox species is chemically reversible). Quasi-reversibility is evident from Fig. 2B, where the ratio of the peak redox currents is observed to differ from unity under no optical illumination, and beyond threshold as the optical power increases, i.e., the peak currents are not symmetric about zero. Nevertheless, the oxidation and reduction rates are significantly enhanced by energetic holes and electrons, as evidenced by the increased currents (Fig. 2B).

The redox potentials beyond threshold also decrease with increasing photon (SPP) energy, as excited carriers become increasingly energetic: In this region, the redox potentials are controlled optically via the photon (SPP) energy, as emphasized by the vertical blue bars in Fig. 2C.

Figure 5 proposes a phenomenological sketch illustrating the creation and transfer of energetic carriers to the redox species as a

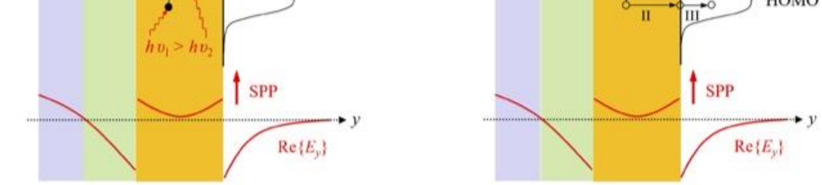

Fig. 5. Phenomenological sketch. Propagating SPPs are absorbed in the WE where they generate energetic electrons (filled circles) and energetic holes (empty circles) (step I: photoexcitation). Some energetic electrons and holes travel to the WE surface (step II: transport), where they are emitted into LUMO or HOMO states (respectively) of the redox species (step III: emission). (**A**) Reduction reaction. (**B**) Oxidation reaction.

three-step process [following internal photoemission (*26*)]. SPPs propagating along the WE are absorbed therein, leading to the photoexcitation of electrons and holes (step I). These excited carriers have excess energy that is primarily kinetic and wave vectors that are initially oriented isotropically. A fraction of the excited carriers reaches the WE surface in contact with the electrolyte (step II), and a fraction of those are emitted into states of adjacent redox molecules—electrons into LUMO (lowest unoccupied molecular orbital) states or holes into HOMO (highest occupied molecular orbital) states, depending on whether the applied potential is reductive (Fig. 5A) or oxidative (Fig. 5B).

The reduction current is enhanced to a greater extent than the oxidation current (Fig. 2). This outcome is aligned with (i) energetic electrons having a longer attenuation length than energetic holes in Au when carriers are excited within ~1 eV about E_F [$L_e \sim 74$ nm, $L_h \sim 55$ nm; (*25*)] and (ii) both types of carriers having similar energy distributions (transitions are indirect intraband near E_F). A larger attenuation length increases the escape probability of electrons from the WE to the redox species, thereby producing a greater enhancement of reduction reactions.

The thickness of the WE ($t = 35$ nm) is smaller than both attenuation lengths (L_e, L_h), which enhances escape probabilities for both types of carriers, because energetic carriers generated throughout the WE can reach the surface in contact with the electrolyte. Furthermore, carriers that travel toward the Au/SiO_2 interface can be reflected therefrom, eventually reaching the surface in contact with the electrolyte, further enhancing escape probabilities [cf. internal photoemission from thin films (*26*)]. This implies that thinner WEs could produce greater enhancements. Last, infrared SPPs (photons) of energy $h\upsilon \sim 1$ eV create electrons and holes in Au that are sufficiently energetic and long-lived to significantly affect electrochemical reactions.

MATERIALS AND METHODS

Preparation of the waveguides and electrodes on chip

Chips incorporating Au stripes with contact pads and grating couplers and Pt stripes with contact pads were fabricated as described in previous work (*27*, *28*) but without upper cladding or lid. Chips without an upper cladding enable direct probing of pads connected to the WE and CE and facilitate alignment of the optical fibers used to couple to the gratings on chip. The upper cladding consisted of the electrolyte solution, prepared as described below. A Au stripe was used simultaneously as an SPP waveguide and WE, whereas a nearby Pt stripe was used as a CE.

The chips were cleaned manually using a swab dipped in acetone to remove protective photoresist (SPR-220) from the surface. Then, a chip was placed into a large glass vial in acetone, and the vial was placed in an ultrasonic bath for 5 min. Next, the chip was promptly rinsed with 3-4 isopropyl alcohol via pipetting and then with deionized water. Pressurized N_2 gas was used to dry the chip. Last, the chip was placed in an ultraviolet (UV)/ozone chamber for 30 min with the UV lamp on, followed by 30 min with the UV lamp light off, as a final cleaning step.

WE and CE were then selected and electrically burned in before use by injecting a current (ramp function) along an electrode structure until its resistance stabilized. Burn-in induces grain reorganization through annealing, which stabilizes the electrodes before use in an electrochemical experiment (*34*). The chip was affixed to the bottom of a petri dish, and electrochemical, optical, or resistance measurements were carried out as required.

Experimental setup

The experimental setup, constructed on a floating optical table, includes a tunable laser (8164A, Agilent) working over the wavelength range from 1270 to 1370 nm. A cleaved bow-tie style polarization-maintaining single-mode optical fiber (PM-SMF) with a 6.6-μm core diameter and a multimode fiber (MMF) with a core diameter of 200 μm were aligned perpendicularly to the input and output grating couplers, respectively. Metallic holders (90°) mounted on multiaxis micropositioners were used to hold the fibers while ensuring that transverse magnetic-polarized light was incident on the input grating. A power meter (PM 100USB, Thorlabs) was used to monitor the power emerging from the MMF coupled to the output grating. Following the scheme illustrated in Fig. 1B, the input PM-SMF was aligned perpendicularly to the input grating coupler such that laser light is incident thereon, exciting Bloch long-range SPPs along the Au stripe in both longitudinal directions. Propagating SPPs are outcoupled by the output grating into light captured by the MMF connected to the power meter. This arrangement in transmission enables optimization of both optical alignments and the operating wavelength.

Two tungsten needles, attached to the arms of two micropositioners, were used to probe pads at the end of a Pt stripe and a Au stripe following the scheme illustrated in Fig. 1B. The needles were coated with poly(methyl methacrylate) except for their tip to ensure no interaction with the electrolyte.

A bipotentiostat (WaveDriver 20, basic bundles, Pine Research Instrumentation) was used for the CV and chronoamperometry measurements. A potentiostat (PARSTAT 2273, Princeton Applied Research) was used for the EIS measurements, and the ZSimpWin software was used to fit the high-frequency impedance responses to the simplified Randle equivalent circuit (Fig. 4A, inset). An Ag/AgCl reference electrode (double junction pH combination, glass body, BNC connector, Sigma-Aldrich) was used in all electrochemical measurements.

The chip was immersed in electrolyte, the reference electrode was dipped nearby, and the needles were used to probe the pads of the WE and CE on chip to connect them to the bipotentiostat in a three-electrode configuration. CV, chronoamperometry, and EIS routines supplied by the manufacturers of our instruments were used to carry out the measurements.

The petri dish housing the chip and electrochemical cell was placed on a TEC. The interface between the petri dish and TEC was filled with silicon paste to ensure high thermal conductivity between these parts. A clean electronic thermometer was dipped in the electrolyte and used with a temperature controller (operating in a closed-loop feedback control algorithm) to control the temperature of the cell via the TEC, over the range from 10° to 40°C. Sufficient time was allowed to lapse whenever the temperature was changed to allow the cell and its contents (electrolyte, chip, and electrodes) to reach thermal equilibrium before any measurements were undertaken.

An electronic source meter (2400, Keithley) along with an extra pair of probe needles and micropositioners was used to measure stripe resistances. An alignment microscope of long working distance was used to align the fibers and probes to the chip. Schematics of our experimental arrangement and setup are given in fig. S1.

Redox species and electrolyte/upper cladding

Potassium ferricyanide {$K_3[Fe(CN)_6]$} and potassium nitrate (KNO_3) were used as supplied (Sigma-Aldrich) as the redox species and supporting electrolyte, respectively. Glycerol (Sigma-Aldrich) was used as supplied and added to the electrolyte (0.2928 g of glycerol per

20 ml of electrolyte) to adjust the refractive index of the solution because it also acts as the upper cladding of the SPP waveguide. The refractive index of the solution was adjusted to $n = 1.3325$ ($\lambda_0 = 1312$ nm), as measured using a prism coupler (Metricon), such that the Bloch long-range SPP could propagate (*27–29*). CV measurements with and without glycerol were identical over the range of potentials of interest (no glycerol oxidation was observed over the potential window of 0 to 0.5 V versus Ag/AgCl used in our study).

Mode computation

The Bloch long-range SPP mode shown in Fig. 1C was computed using the Method of Lines (*35*). The multilayer structure is composed of 15 periods of a SiO_2 on Ta_2O_5 unit cell of thicknesses d_{SiO2}= 495 nm (n_{SiO2}= 1.447) and d_{Ta2O5}= 235 nm (n_{Ta2O5}= 2.069), on a starting layer of SiO_2 of the same thickness, on a Si wafer. This multilayer was designed to achieve wave number matching at free-space wavelengths near $\lambda_0 = 1310$ nm, as described elsewhere (*29*). The relative permittivity of the Au stripe at $\lambda_0 = 1310$ nm was taken as $\varepsilon_r = -86.8 - j8.322$ (*36*), and its dimensions were set to $w = 5$ μm and $t =$ 35 nm. The upper cladding was taken as an optically semi-infinite region of electrolyte with glycerol as described above. Figure 5 gives a partial cross-sectional sketch of the structure.

Experimental arrangement for direct resistive heating of WE

Heating the stripe directly produces a thermal gradient in the electrolyte that resembles closely the thermal gradient produced by absorption of the propagating SPP [cf. thermal computations for comparable structures (*37*)]. The setup of fig. S7 was used to obtain CV curves, while the Au WE electrode was simultaneously heated resistively via the passage of current. A power supply (Model PAB 25-1 tr, KIKUSUI) was connected to a WE by probing the pads at each end and applying a voltage in the range of 2.5 to 8.5 V. An ammeter (Agilent U1242B multimeter) was inserted in series to measure the current *I* flowing out of the power supply. This current is of the order of milliamperes, much larger than the current flowing in/out of the WE to the redox species during CV measurements which is of the order of microamperes. The measured current *I* and the voltage applied by the power supply were used to obtain the resistance of the WE and deduce its temperature by using the temperature coefficient of resistivity of Au (fig. S4B). The voltage range was selected to increase the temperature of the WE from 20° to 50°C, in correspondence with the temperature range in our optical experiments. The temperature of the electrochemical cell was kept to 20°C using the TEC placed under the petri dish, thereby ensuring a stable thermal gradient from the WE into the electrolyte. Sufficient time was allowed to lapse whenever the voltage was changed to allow the system to reach thermal equilibrium before any measurements were recorded. The bipotentiostat was used to simultaneously obtain CV measurements on the WE, in 0.5 mM $K_3[Fe(CN)_6]$ + 100 mM KNO_3 electrolyte, at a scan rate of 100 mV/s. Interference between the instruments in the setup was not detected.

SUPPLEMENTARY MATERIALS

Supplementary material for this article is available at https://science.org/doi/10.1126/sciadv.abm9303

REFERENCES AND NOTES

1. W. L. Barnes, A. Dereux, T. W. Ebbesen, Surface plasmon subwavelength optics. *Nature* **424**, 824–830 (2003).
2. P. Berini, Long-range surface plasmon polaritons. *Adv. Opt. Photon.* **1**, 484–588 (2009).
3. R. Sundararaman, P. Narang, A. S. Jermyn, W. A. Goddard III, H. A. Atwater, Theoretical predictions for hot-carrier generation from surface plasmon decay. *Nat. Commun.* **5**, 5788 (2014).
4. C. Clavero, Plasmon-induced hot-electron generation at nanoparticle/metal-oxide interfaces for photovoltaic and photocatalytic devices. *Nat. Photonics* **8**, 95–103 (2014).
5. M. L. Brongersma, N. J. Halas, P. Nordlander, Plasmon-induced hot carrier science and technology. *Nat. Nanotechnol.* **10**, 25–34 (2015).
6. S. Linic, U. Aslam, C. Boerigter, M. Morabito, Photochemical transformations on plasmonic metal nanoparticles. *Nat. Mater.* **14**, 567–576 (2015).
7. Y. Zhang, S. He, W. Guo, Y. Hu, J. Huang, J. R. Mulcahy, W. D. Wei, Surface-plasmon-driven hot electron photochemistry. *Chem. Rev.* **118**, 2927–2954 (2018).
8. X. Shan, U. Patel, S. Wang, R. Iglesias, N. Tao, Imaging local electrochemical current via surface plasmon resonance. *Science* **327**, 1363–1366 (2010).
9. S. Wang, X. Huang, X. Shan, K. J. Foley, N. Tao, Electrochemical surface plasmon resonance: Basic formalism and experimental validation. *Anal. Chem.* **82**, 935–941 (2010).
10. T. Sannomiya, H. Dermutz, C. Hafner, J. Vörös, A. B. Dahlin, Electrochemistry on a localized surface plasmon resonance sensor. *Langmuir* **26**, 7619–7626 (2010).
11. C. Novo, A. M. Funston, A. K. Gooding, P. Mulvaney, Electrochemical charging of single gold nanorods. *J. Am. Chem. Soc.* **131**, 14664–14666 (2009).
12. A. B. Dahlin, B. Dielacher, P. Rajendran, K. Sugihara, T. Sannomiya, M. Zenobi-Wong, J. Vörös, Electrochemical plasmonic sensors. *Anal. Bioanal. Chem.* **402**, 1773–1784 (2012).
13. Y. Zhang, W. Guo, Y. Zhang, W. D. Wei, Plasmonic photoelectrochemistry: In view of hot carriers. *Adv. Mater.* **33**, 2006654 (2021).
14. L. Zhou, D. F. Swearer, C. Zhang, H. Robatjazi, H. Zhao, L. Henderson, L. Dong, P. Christopher, E. A. Carter, P. Nordlander, N. J. Halas, Quantifying hot carrier and thermal contributions in plasmonic photocatalysis. *Science* **362**, 69–72 (2018).
15. P. K. Jain, Taking the heat off of plasmonic chemistry. *J. Phys. Chem. C* **123**, 24347–24351 (2019).
16. G. Baffou, I. Bordacchini, A. Baldi, R. Quidant, Simple experimental procedures to distinguish photothermal from hot-carrier processes in plasmonics. *Light Sci. Appl.* **9**, 108 (2020).
17. E. Cortés, L. V. Besteiro, A. Alabastri, A. Baldi, G. Tagliabue, A. Demetriadou, P. Narang, Challenges in plasmonic catalysis. *ACS Nano* **14**, 16202–16219 (2020).
18. Y. Dubi, I. W. Un, Y. Sivan, Thermal effects – An alternative mechanism for plasmon-assisted photocatalysis. *Chem. Sci.* **11**, 5017–5027 (2020).
19. Y. Yu, J. D. Williams, K. A. Willets, Quantifying photothermal heating at plasmonic nanoparticles by scanning electrochemical microscopy. *Faraday Discuss.* **210**, 29–39 (2018).
20. Y. Yu, V. Sundaresan, K. A. Willets, Hot carriers versus thermal effects: Resolving the enhancement mechanisms for plasmon-mediated photoelectrochemical reactions. *J. Phys. Chem. C* **122**, 5040–5048 (2018).
21. M. Maley, J. W. Hill, P. Saha, J. D. Walmsley, C. M. Hill, The role of heating in the electrochemical response of plasmonic nanostructures under illumination. *J. Phys. Chem. C* **123**, 12390–12399 (2019).
22. C. Zhan, B.-W. Liu, Y.-F. Huang, S. Hu, B. Ren, M. Moskovits, Z.-Q. Tian, Disentangling charge carrier from photothermal effects in plasmonic metal nanostructures. *Nat. Commun.* **10**, 2671 (2019).
23. A. J. Wilson, V. Mohan, P. K. Jain, Mechanistic understanding of plasmon-enhanced electrochemistry. *J. Phys. Chem. C* **123**, 29360–29369 (2019).
24. M. Bauer, A. Marienfeld, M. Aeschlimann, Hot electron lifetimes in metals probed by time-resolved two-photon photoemission. *Prog. Surf. Sci.* **90**, 319–376 (2015).
25. R. N. Stuart, F. Wooten, W. E. Spicer, Mean free path of hot electrons and holes in metals. *Phys. Rev. Lett.* **10**, 7–9 (1963).
26. C. Scales, P. Berini, Thin-film Schottky barrier photodetector models. *IEEE J. Quant. Electr.* **46**, 633–643 (2010).
27. N. R. Fong, M. Menotti, E. Lisicka-Skrzek, H. Northfield, A. Olivieri, N. Tait, M. Liscidini, P. Berini, Bloch long-range surface plasmon polaritons on metal stripe waveguides on a multi-layer substrate. *ACS Photonics* **4**, 593–599 (2017).
28. M. Khodami, Z. Hirbodvash, O. Krupin, W. R. Wong, E. Lisicka-Skrzek, H. Northfield, C. Hahn, P. Berini, Fabrication of Bloch long range surface plasmon waveguides integrating counter electrodes and microfluidic channels for multimodal biosensing. *J. Microelectromech. Syst.* **30**, 686–695 (2021).
29. M. Khodami, P. Berini, Grating couplers for (Bloch) long-range surface plasmons on metal stripe waveguides. *J. Opt. Soc. Am. B* **36**, 1921–1930 (2019).
30. U. K. Sur, F. Marken, N. Rees, B. A. Coles, R. G. Compton, R. Seager, Microwave enhanced electrochemistry: Mass transport effects and steady state voltammetry in the sub-millisecond time domain. *J. Electroanal. Chem.* **573**, 175–182 (2004).
31. J. E. O'Reilly, Oxidation-reduction potential of the ferro-ferricyanide system in buffer solutions. *Biochim. Biophys. Acta* **292**, 509–515 (1973).

32. T. Kim, J. S. Lee, G. Lee, H. Yoon, J. Yoon, T. J. Kang, Y. H. Kim, High thermopower of ferri/ferrocyanide redox couple in organic-water solutions. *Nano Energy* **31**, 160–167 (2017).
33. B.-A. Mei, O. Munteshari, J. Lau, B. Dunn, L. Pilon, Physical interpretations of nyquist plots for EDLC electrodes and devices. *J. Phys. Chem. C* **122**, 194–206 (2018).
34. Z. Hirbodvash, M. S. E. Houache, O. Krupin, M. Khodami, H. Northfield, A. Olivieri, E. A. Baranova, P. Berini, Electrochemical performance of lithographically-defined micro-electrodes for integration and device applications. *Chem* **9**, 277 (2021).
35. P. Berini, K. Wu, Modeling lossy anisotropic dielectric waveguides with the method of lines. *IEEE Trans. Microw. Theory Techn.* **44**, 749–759 (1996).
36. E. D. Palik, Ed., *Handbook of Optical Constants of Solids* (Academic Press, 1985).
37. G. Gagnon, N. Lahoud, G. A. Mattiussi, P. Berini, Thermally activated variable attenuation of long-range surface plasmon-polariton waves. *J. Lightw. Technol.* **24**, 4391–4402 (2006).
38. R. B. Belser, W. H. Hicklin, Temperature coefficients of resistance of metallic films in the temperature range 25° to 600 °C. *J. Appl. Phys.* **30**, 313–322 (1959).

Acknowledgments: We are grateful to L. Sun, Pine Research for assistance with the electrochemical measurements. **Funding:** Financial support provided by the Natural Sciences and Engineering Research Council of Canada is acknowledged under grant 210396. **Author contributions:** Z.H. carried out the optical and electrochemical experiments, contributed to measurement interpretation, and prepared the first draft of the manuscript. O.K. assisted with the measurements and interpretation. H.N. and A.O. fabricated the waveguide structures tested. E.A.B. assisted with the experimental techniques and the interpretation of the measurements. P.B. carried out the mode computations and directed the research. All authors contributed to writing the manuscript. **Competing interests:** The authors declare that they have no competing interests. **Data and materials availability:** All data needed to evaluate the conclusions in the paper are present in the paper and/or the Supplementary Materials.

Submitted 21 October 2021
Accepted 1 April 2022
Published 18 May 2022
10.1126/sciadv.abm9303

Supplementary Materials for

Infrared surface plasmons on a Au waveguide electrode open new redox channels associated with the transfer of energetic carriers

Zohreh Hirbodvash,[1,2] Oleksiy Krupin,[2] Howard Northfield,[2] Anthony Olivieri,[2] Elena A. Baranova,[3,4] and Pierre Berini[1,2,5,*]

[1]Dept. of Physics, University of Ottawa, 150 Louis Pasteur, Ottawa, Ontario, K1N 6N5, Canada
[2]Center for research in Photonics, University of Ottawa, 25 Templeton St., Ottawa, Ontario, K1N 6N5, Canada
[3]Department of Chemical and Biological Engineering, University of Ottawa, 161 Louis-Pasteur, Ottawa, ON K1N 6N5, Canada
[4]Centre for Catalysis Research and Innovation, University of Ottawa, 161 Louis-Pasteur, Ottawa, ON K1N 6N5, Canada
[5]School of Electrical Engineering and Computer Science, University of Ottawa, 800 King Edward Ave., Ottawa, Ontario, K1N 6N5, Canada
*Corresponding Author; berini@eecs.uottawa.ca

This file includes: Figures S1 to S9

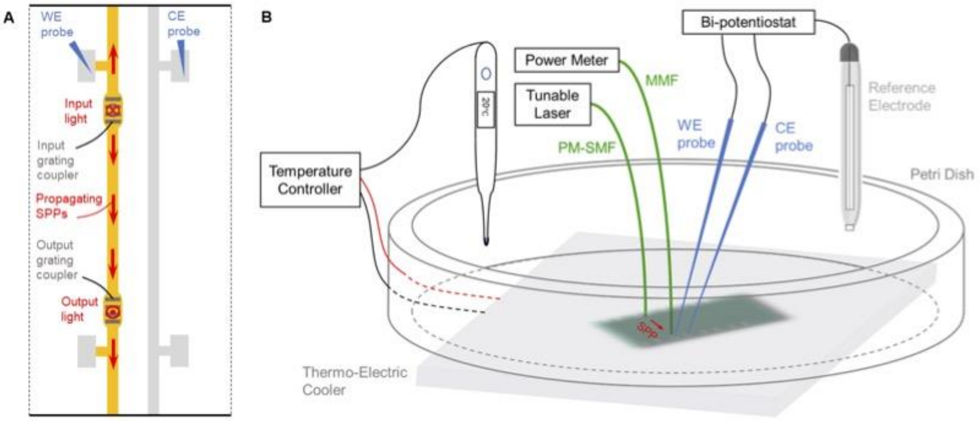

Fig. S1. Experimental set-up. (**A**) Sketch of chip and (**B**) block diagram of experimental set-up. PM-SMF: polarization-maintaining single-mode fibre; MMF: multi-mode fibre; WE: working electrode; CE: counter electrode.

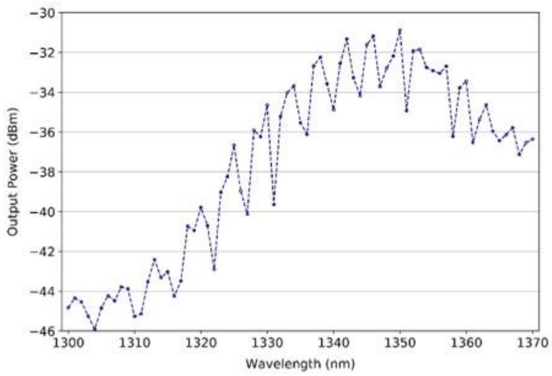

Fig. S2. Wavelength response of grating-coupled waveguide / working electrode.
Wavelength response of grating couplers, separated by a waveguide segment of length l_3 = 1850 µm (Fig. 1B, main text). The incident optical power was set to 8 dBm. The combined grating coupling losses are ~20 dB, and the propagation loss of the Bloch LRSPP along the stripe is ~12 dB/mm (*28*).

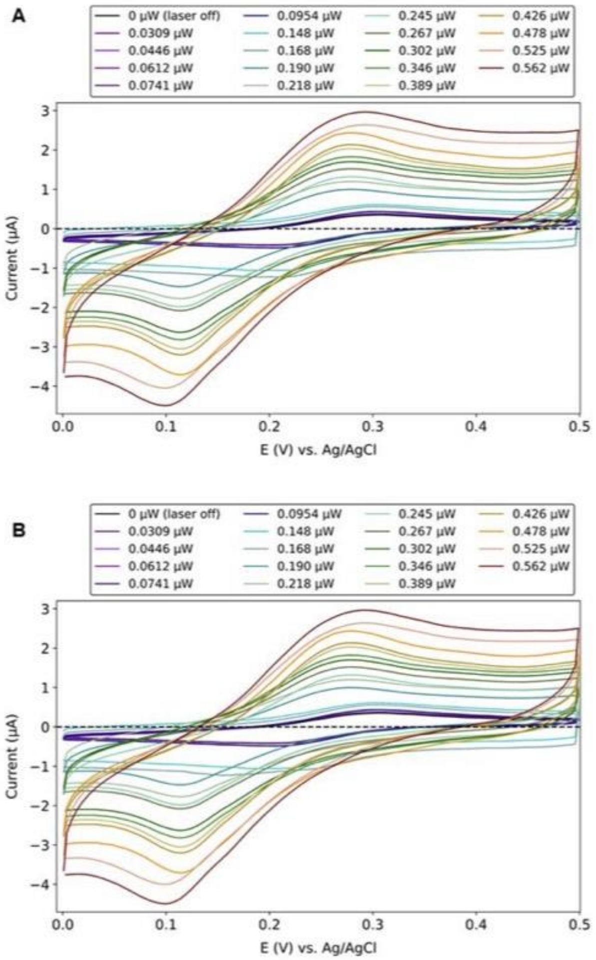

Fig. S3. Cyclic voltammetry under optical illumination. CV curves obtained on a Au WE, in 0.5 mM $K_3[Fe(CN)_6]$ + 100 mM KNO_3 electrolyte, at a scan rate of 100 mV/s, for increasing optical output power (legend) at (**A**) λ_0 = 1330 nm (**B**) λ_0 = 1370 nm. The incident optical power ranged from 0 to 6.3 mW. The reference CV curve (laser off) is plotted in black.

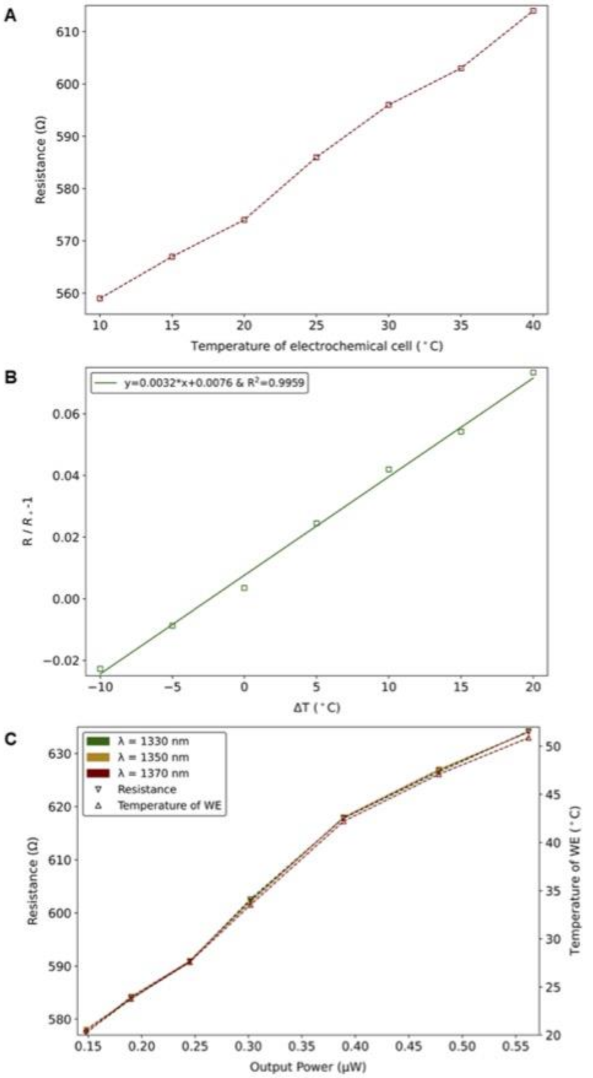

Fig. S4. Resistance of WE as a function of temperature and optical power. (**A**) Resistance of a Au WE measured *in situ vs*. the temperature of the electrochemical cell as controlled using the TEC, with the laser off. (**B**) Results of Part (A) re-plotted using $R = R_0[1+\alpha(T - T_0)]$ such that the temperature coefficient of resistivity (α) appears as the slope; R_0 is the resistance at the reference temperature of $T_0 = 20$ °C, R is the resistance at temperature T, and $\Delta T = T - T_0$. The best fit linear model given in the legend yields $\alpha = 3.2\times10^{-3}$ °C^{-1}, in excellent agreement with the literature for bulk Au (*35*). (**C**) Resistance of Au WE measured *in situ vs.* increasing output optical power ($\lambda_0 = 1330, 1350, 1370$ nm), with the electrochemical cell maintained at 20 °C. The corresponding temperature of the WE, T, is plotted on the right axis, deduced using the relation $R = R_0[1+\alpha(T - T_0)]$ with $T_0 = 20$ °C, and R_0 and α as measured in Part (B).

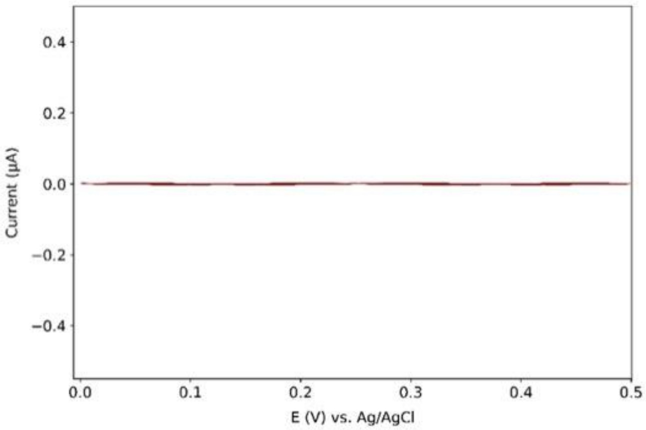

Fig. S5. CV Measurements obtained without redox species. CV curves obtained on a Au WE, in 100 mM KNO_3 electrolyte (electrolyte only), at a scan rate of 100 mV/s.

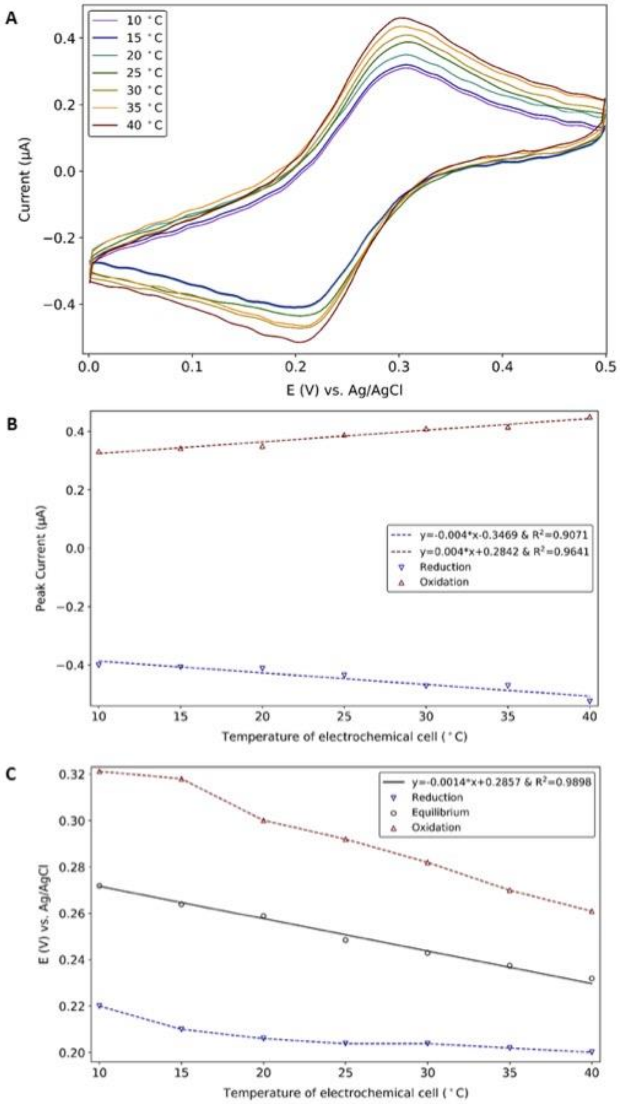

Fig. S6. Cyclic voltammetry at various cell temperatures. (**A**) CV curves obtained on a Au WE, in 0.5 mM $K_3[Fe(CN)_6]$ + 100 mM KNO_3 electrolyte, at a scan rate of 100 mV/s, as the temperature of the electrochemical cell was varied using the TEC from 10 to 40 °C (legend). (**B**) Redox current peaks, and (**C**) potentials *vs*. cell temperature, obtained from the CV curves of Part (A). Linear models fitted to the peak redox currents are plotted as the dashed lines in Part (B) and given in the legend (slopes have units of μA/°C). A linear model fitted to the equilibrium potential (mean of redox potentials) is plotted as the solid black line in Part (C) and given in the legend (slope has units of V/°C). The linear models of Parts B and C are transposed to Figs. 2B and 2C of the main text (respectively) where they are plotted as dashed blue lines.

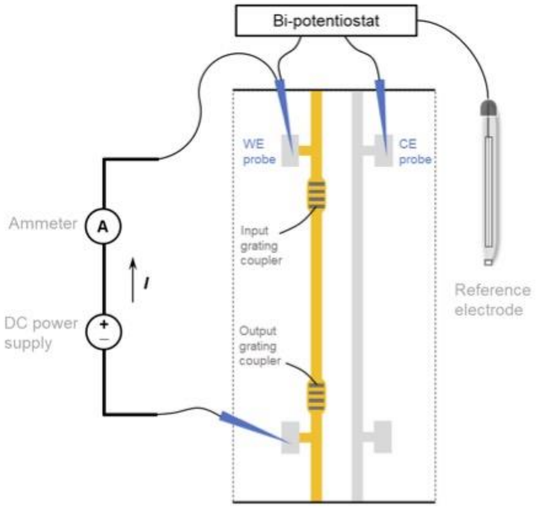

Fig. S7. Experimental arrangement for direct resistive heating of the WE. WE: working electrode; CE: counter electrode. Arrangement immersed in Petri dish on TEC as in Fig. S1B. The current *I* is measured using the ammeter and resistively heats the WE *in situ*.

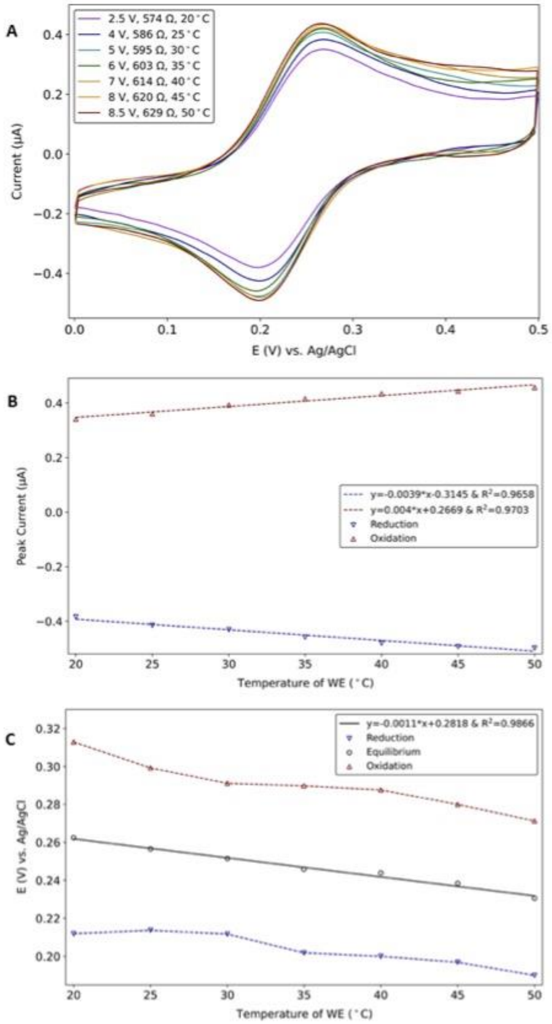

Fig. S8. Cyclic voltammetry at various WE temperatures. (**A**) CV curves obtained on a Au WE, in 0.5 mM $K_3[Fe(CN)_6]$ + 100 mM KNO_3 electrolyte, at a scan rate of 100 mV/s, as the temperature of the WE was varied from 20 to 50 °C (legend) by direct resistive heating produced by simultaneously passing current along the WE using the experimental arrangement of Fig. S7. The temperature of the WE (legend) was deduced from its resistance using the relation $R = R_0[1+\alpha(T - T_0)]$ with α as measured in Fig. S4B. The electrochemical cell was maintained at 20 °C using the TEC. (**B**) Redox current peaks, and (**C**) potentials *vs*. WE temperature, obtained from the CV curves of Part (A). Linear models fitted to the peak redox currents are plotted as the dashed lines in Part (B) and given in the legend (slopes have units of µA/°C). A linear model fitted to the equilibrium potential (mean of redox potentials) is plotted as the solid black line in Part (C) and given in the legend (slope has units of V/°C).

fitted to the equilibrium potential (mean of redox potentials) is plotted as the solid black line in Part (C) and given in the legend (slope has units of V/°C).

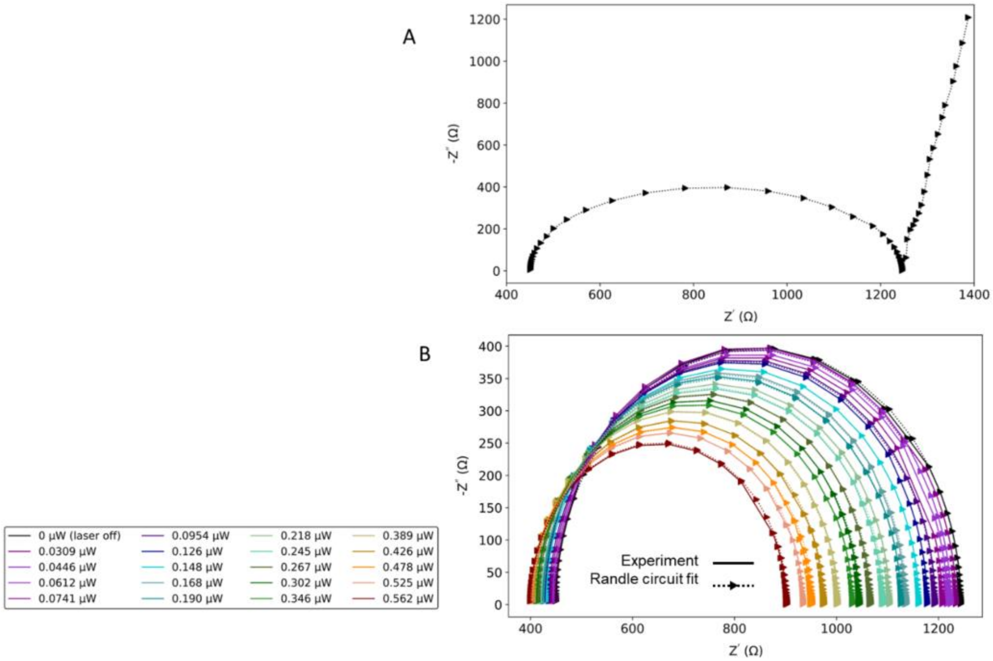

Fig. S9. Open-circuit electrochemical impedance spectroscopy. (**A**) Electrochemical impedance frequency response, measured on a Au WE, in 0.5 mM $K_3[Fe(CN)_6]$ + 100 mM KNO_3 electrolyte, under no illumination (laser off). The AC potential amplitude was set to 5 mV RMS (*vs*. Ag/AgCl). The impedance response is plotted over the frequency range 100 kHz to 1 Hz as a Nyquist plot ($Z = Z' + iZ''$). The plot comprises a semicircle at high frequencies (400 Ω $< Z' <$ 1250 Ω) followed by an approximately diagonal linear trend (1250 $< Z' <$ 1300 Ω). The open circuit DC potential was measured as 252 mV (*vs*. Ag/AgCl) under no illumination, in agreement with the equilibrium potential observed on Fig. 2C. (**B**) High-frequency impedance responses, plotted over the frequency range 100 kHz to 3 Hz, as Nyquist plots, under optical illumination at λ_0 = 1350 nm, for increasing output optical power (legend) (other parameters are the same as in Part A). These plots were fit to the Randle equivalent circuit, and the extracted parameters (R_{ct}, C_{dl} and R_s) plotted *vs.* output optical power in Fig. 4B of the main text (stars).

Corrigendum

We discovered errors in our Nyquist plots reporting our impedance spectroscopy results, affecting Fig. 4A of the main text and Fig. S9 of the Supplementary Materials. The errors occurred upon rendering the final figures for production, when combining data from different sources – measurements from our potentiostat and computer modelling fits. These errors do not affect our fits, discussion, interpretation or conclusions, as the latter were all based on the original data sources.

Fig. 4A of the main text should be replaced with new Fig. 4A given below. We have corrected Fig. S9 and its caption and submit the corrected Supplementary Materials file herewith. We also include the "as-published" manuscript pdf, highlighting two minor corrections to units that should be made in the main text and in the caption to Fig. 4 – these errors escaped us when reviewing the article proofs.

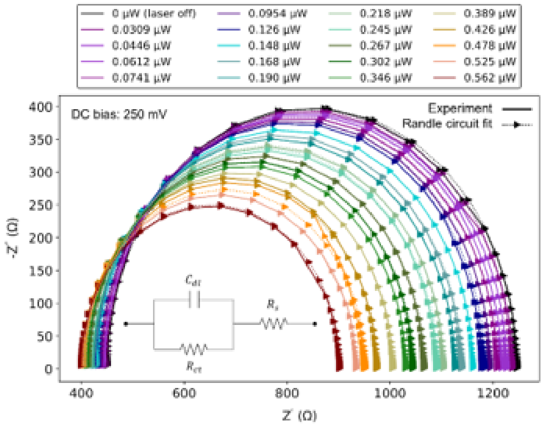

New Fig. 4A

Supplementary materials for Limit of detection

The limit of detection was determined for three electrode cases, (i) a commercial Au electrode, (ii) the Au waveguide electrode supporting SPPs under optical illumination, and (iii) the Au waveguide electrode without optical illumination. The setup is the same as used in the Science Advances paper. Using potassium ferricyanide as the redox species, dissolved in potassium nitrate, at a scan rate of 300 mV/s, cyclic voltammograms were acquired using the commercial Au electrode (outer diameter 6 mm, inner diameter 1.6 mm purchased from London Scientific). CVs were also performed on Au waveguide electrodes with and without optical illumination under the same conditions as commercial Au electrode. The input laser power for the Au waveguide under illumination was 8 dBm (6.039 mW). Fig. 1A plots the CVs of these three cases on one figure. Fig. 1B shows calibration graphs, taken as the peak oxidative current *vs*. the concentration of potassium ferricyanide, based on the CV curves of Fig. 1A, obtained using an on-chip Au working electrode (with and without the plasmonic excitation), and the commercial electrode.

The limit of detection is 0.07 mol/m^3 for the Au waveguide without optical illumination, 0.028 mol/m^3 for the commercial gold electrode, and 0.007 mol/m^3 for the Au waveguide under plasmonic excitation (Fig. 1C). As discussed previously, these results are in agreement with an earlier study which found that the current obtained from the commercial Au electrode was 3.4 times larger than that obtained from the Au waveguide without optical illumination (chapter 4). As a result of LRSPP excitation of a waveguide working electrode, the current was also enhanced by 10 times, which is the ratio of the limit of detection with and without optical excitation of LRSPPs on the working electrode.

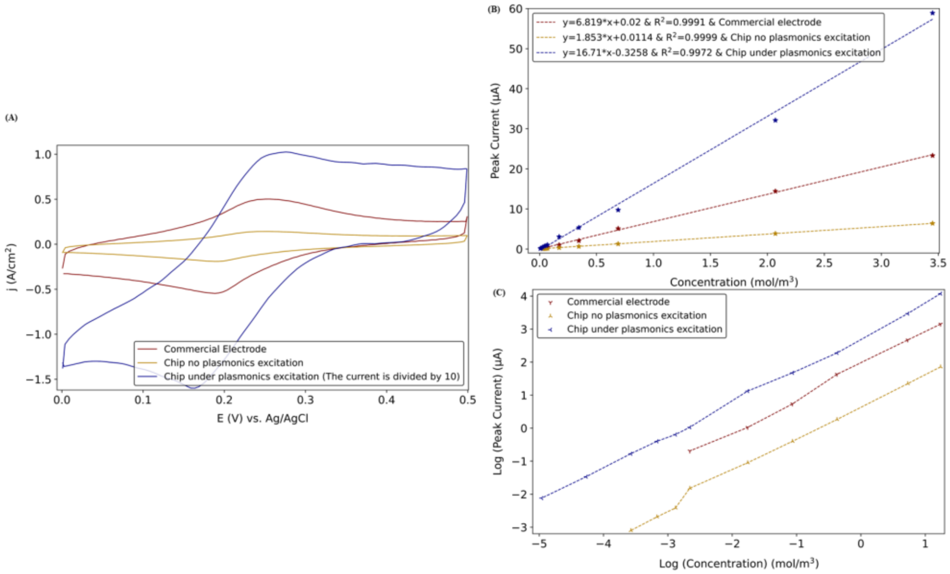

Fig. 1. Cyclic voltammograms on commercial gold electrode, and gold waveguide electrodes with and without LRSPP excitation using 0.1 mM of potassium ferricyanide as the redox species at scan rate of 300 mV/s. (b) Calibration graphs for various concentrations, taken as the peak oxidative current *vs*. the concentration of potassium ferricyanide, based on the CV curves of part (a), obtained using on-chip Au working electrode (with and without LRSPP excitation), and commercial electrode. (c) Log (Peak Current) *vs*. Log(concentration) showing the limit of detection of the different cases.

Chapter 6.

Convolutional Voltammetry Enhanced by Energetic Electrons and Holes on a LRSPP Waveguide Electrode

6.1. Contribution

In this chapter, results are presented that are published in ACS, Analytical Chemistry. Zohreh Hirbodvsh carried out the optical and electrochemical experiments, contributed to theoretical part and measurement interpretation, and prepared the first draft of the manuscript. Dr. Baranova assisted with the experimental techniques and the interpretation of the measurements. Dr. Berini directed the research. All Authors contributed to writing the manuscript.

6.2. Summary

The cyclic voltammetry (CV) and chronoamperometry measurements were performed to investigate convolutional voltammetry by monitoring the SPP output power in real time vs. the applied potential. Experimentally and theoretically, we prove that the output power of the SPP is proportional to the convolution of the electrochemical current. The SPP voltammogram confirms that the changes in signal are primarily caused by changes in the refractive index between the reduced and oxidized forms of the redox species. Additionally, we demonstrate that energetic carriers generated by SPP absorption increase the sensitivity of electrochemical detection.

6.3. Article

The article follows here verbatim.

analytical chemistry

pubs.acs.org/ac Article

Real-Time Convolutional Voltammetry Enhanced by Energetic (Hot) Electrons and Holes on a Surface Plasmon Waveguide Electrode

Zohreh Hirbodvash, Elena A. Baranova, and Pierre Berini*

Cite This: *Anal. Chem.* 2022, 94, 13145−13152 Read Online

ACCESS | Metrics & More | Article Recommendations | Supporting Information

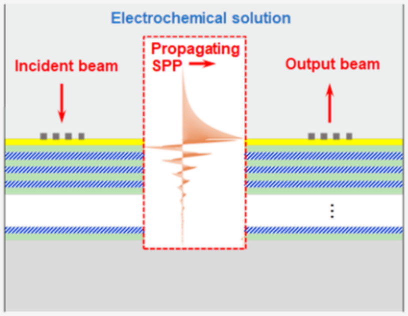

ABSTRACT: Surface plasmon polaritons (SPPs) propagating along a waveguide working electrode are sensitive to changes in the local refractive index, which follow changes in the concentration of reduced and oxidized species near the working electrode. The real-time response of the output optical power from a waveguide working electrode is proportional to the time convolution of the electrochemical current density, precluding the need to compute the latter a posteriori via numerical integration. Convolutional voltammetry yields complementary results to conventional voltammetry and can be used to determine the diffusion constant, bulk concentration, and the number of transferred electrons of electroactive species. The theoretical optical response of a waveguide working electrode is derived and validated experimentally via chronoamperometry and cyclic voltammetry measurements under low power SPP excitation, for various concentrations of potassium ferricyanide in potassium nitrate electrolyte at various scan rates. Increasing the SPP power induces a regime where the SPPs no longer act solely as a probe of electrochemical activity, but also as a pump creating energetic electrons and holes via absorption in the working electrode. In this regime, the transfer of energetic carriers (electrons and holes) to the redox species dominates the electrochemical current density, which becomes significantly enhanced relative to equilibrium conditions (low SPP power). In this regime the output optical power remains proportional to the time convolution of the current density, even with the latter significantly enhanced by the transfer of energetic carriers.

■ INTRODUCTION

Convolutional voltammetry, developed initially by Imbeaux and Saveant,[1] is based on an electrochemical technique, such as voltammetry, chronoamperometry, or chronocoulometry, followed by a mathematical transformation (convolution) of measured signals.[2−5] Convolutional voltammetry is useful because the results are directly related to the concentration of electroactive species at the working electrode surface. Conversely, voltammetric, chronoamperometric, or chronocoulometric measurements are directly related to the flux of a species. Thus, convolutional voltammetry yields complementary results and offers advantages over conventional electrochemical techniques, such as low sensitivity to a drop in current flowing through the electrochemical system[2,6] and independence of the scan rate in cyclic voltammetry.[7] Convolutional voltammetry has been used to determine the diffusion constant, bulk concentration, and the number of transferred electrons of electroactive species. However, convolved signals are not generated directly in a conventional electrochemical experiment, so convolutional techniques are deemed less convenient.[8]

A metal-coated prism enabling surface plasmon resonance (SPR) measurements in the Kretschmann configuration can be placed in an electrochemical cell, and the metal surface used to support surface plasmon polaritons (SPPs) can operate simultaneously as the working electrode (WE), enabling joint electrochemical SPR measurements (EC-SPR).[9−11] The SPR response in such systems directly monitors changes in the optical parameters of the redox species at the metal/electrolyte interface as electrochemical reactions occur. In such configurations, the SPR signal measured in real time during an electrochemical reaction follows the convolution of the electrochemical current.[11] EC-SPR can thus be used to measure convolutional voltammetry directly and quantitatively.[9−11]

EC-SPR voltammetry techniques are similar to techniques involving a microdisk electrode or a rotating disk electrode, in that they are scan-rate-independent.[12] In conventional electrolytes (e.g., salts in molecular solvents), steady-state microdisk electrode or rotating disk electrode voltammetry is effective in determining fundamental parameters, e.g., diffusion coefficients or bulk concentrations of electroactive species,[12] but have

Received: June 20, 2022
Accepted: September 6, 2022
Published: September 15, 2022

https://doi.org/10.1021/acs.analchem.2c02643
Anal. Chem. 2022, 94, 13145−13152

proven difficult to apply in highly viscous media such as ionic liquids at room temperature. Many studies have demonstrated that convolutional voltammetry is robust enough to determine accurate values of diffusivity, bulk concentration, and the stoichiometric number of electrons for electrode reactions in molecular solvents and room temperature ionic liquids.[12]

Electrochemical electrodes formed into plasmonic structures are also being used in studies of plasmon-induced energetic (hot) carrier electrochemistry.[13] Advantageously, by separating oxidation and reduction reactions electrochemically, the role of energetic holes can be distinguished from that of energetic electrons. Energetic carriers are created in a WE via SPP absorption therein,[14] but absorption also raises the temperature of the metal and heat diffuses into the surrounding reaction volume.[15−17] It is not trivial to separate the effects of temperature from the effects of energetic carriers, given that electrochemical reactions and fluid dynamics are temperature dependent, but it is possible to isolate effects through careful experimental design and control experiments.[18−23]

In recent work, infrared SPPs propagating along a Au WE shaped as a stripe waveguide induced significant increases in redox currents (10×) along with significant decreases in redox potentials, attributed to the creation of energetic carriers (electrons and holes) by SPP absorption in the Au stripe.[23] Here, we investigate convolutional voltammetry in this system by monitoring the electrochemical current and the output optical power in real time versus the applied potential, as chronoamperometry and cyclic voltammetry (CV) measurements are performed. Output optical power voltammograms indicate that changes in optical signal are caused mainly by changes in the refractive index near the WE, following changes in concentration of the reduced and oxidized forms of the redox species. We also find that the output optical power is proportional to the convolution of the electrochemical current in the low SPP power regime, and that this relationship persists at high SPP powers where the electrochemical current is dominated by redox reactions involving energetic carriers. We formulate a theoretical model of the system which we validate experimentally.

■ THEORETICAL SECTION

The system of interest exploits Bloch long-range SPPs[24] propagating along a metal stripe waveguide operating simultaneously as a WE, coupled to external optoelectronics using input and output grating couplers,[25] as sketched in Figure 1. SPP transmission is monitored by measuring the output optical power, P_{out}, which is the optical measurand. The current flowing through the WE into the redox species is the electrical measurand. Advantages of this system include a compact arrangement, a WE that is defined lithographically and is well-controlled structurally, SPPs that propagate over the entire length of the WE with complete overlap, and a thin WE which enhances the escape probability of energetic carriers created therein via SPP absorption.[23]

The expression that relates the output optical power (P_{out}) to the incident optical power (P_{inc}) is written as

$$P_{\text{out}}(n_c) = P_{\text{inc}}T_{\text{in}}(n_c)e^{-2\alpha(n_c)l_3}T_{\text{out}}(n_c) = P_{\text{inc}}T_s(n_c) \qquad (1)$$

where T_{in} is the transmittance of the incident beam to SPPs propagating along the WE coupled by the input grating, T_{out} is the transmittance of the SPPs to the output beam coupled by the output grating, α [m^{-1}] is the field attenuation coefficient of the propagating SPPs, and l_3 [m] is the propagation distance of SPPs between the input and output grating couplers (Figure 1a). T_{in}, T_{out}, and α are dependent on the refractive index of the electrochemical solution (n_c). T_s in the second equality lumps these contributions together as the channel transmittance.

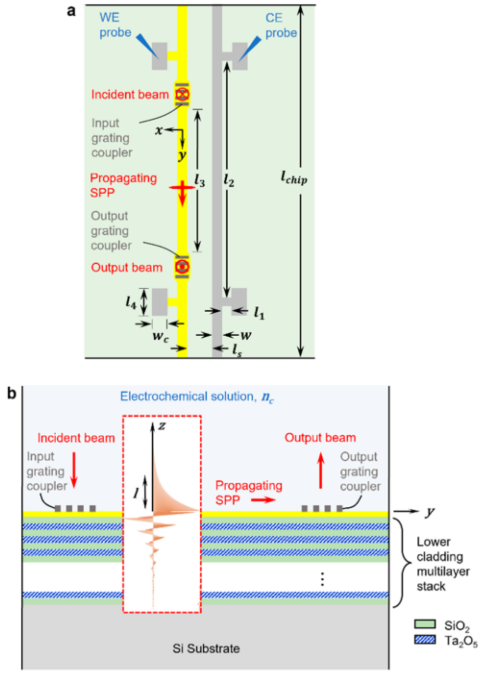

Figure 1. (a) Schematic of the top view of the sensing chip. The thickness of the Au WE (yellow) and Pt CE (gray) is t = 35 nm, and their dimensions are l_1 = 29 μm, l_2 = 2600 μm, l_3 = 1850 μm, l_4 = 250 μm, l_{chip} = 3000 μm, w_c = 100 μm, w = 5 μm, l_s = 40 μm. Experimental scheme: Laser light delivered by a PM-SMF is normally incident as the input beam on the input grating coupler, exciting SPPs that propagate along the WE. The output grating coupler converts the SPPs to the output beam emerging normally from the chip, captured by a MMF, and measured using a power meter. The WE and CE are contacted using external probes to form a three-electrode electrochemical system with a Ag/AgCl reference electrode (not shown). The chip is fixed to the bottom of a Petri dish immersed by the redox species in electrolyte. (b) Sketch of a longitudinal cross-section taken along the center of a WE. The electrochemical solution of refractive index n_c covers the structure. The inset shows the computed distribution of $Re\{E_z\}$ of the Bloch long-range SPP that propagates along the WE, showing the 1/e field penetration depth into the electrochemical solution (l).

The structure operates optically as an attenuation-based sensor,[26,27] transducing changes in n_c to changes in output optical power, where n_c is the refractive index of the electrochemical solution that covers the stripe. Small changes in output optical power (power response), ΔP_{out}, caused by perturbations in the refractive index (Δn_c) can be expressed as

$$\Delta P_{\text{out}} = \frac{\partial P_{\text{out}}}{\partial n_c}\Delta n_c = S_{\text{B,SPP}}\Delta n_c \qquad (2)$$

In the above expression, $S_{\mathrm{B,SPP}}$ [W/RIU] is the bulk sensitivity, which can be determined via calibration or modeling.[28]

We consider a reversible redox reaction occurring along one dimension normal to the WE (z axis) and assume that the redox species does not bind or accumulate on the WE but only changes the refractive index of the electrochemical solution in its vicinity.[11] We ignore the double-layer capacitance and the associated charging and discharging currents.

The electrochemical solution is comprised of the electrolyte and the redox species. Its time-dependent refractive index in the direction normal to the WE (z) is written as

$$\begin{aligned} n_c(z,\, t) &= n_e + \alpha_{\mathrm{O}} C_{\mathrm{O}}(z,\, t) + \alpha_{\mathrm{R}} C_{\mathrm{R}}(z,\, t) \\ &= n_e + \Delta n_c(z,\, t) \end{aligned} \tag{3}$$

where n_e is the refractive index of the electrolyte only (constant), $C_{\mathrm{O}}(z,\, t)$ and $C_{\mathrm{R}}(z,\, t)$ [mol/m^3, M] are the time-dependent concentration distributions of the oxidized and reduced species, $\alpha_{\mathrm{O}} = \partial n_e/\partial C_{\mathrm{O}}$ and $\alpha_{\mathrm{R}} = \partial n_e/\partial C_{\mathrm{R}}$ [m^3/mol, M^{-1}] are the changes in refractive index per unit concentration of oxidized and reduced species (index increments).

The refractive index perturbation is position- and time-dependent, $\Delta n_c(z,t)$, so the time-dependent power response following eq 2 is approximated analytically as the overlap of the normalized decay profile of the SPP intensity over $\Delta n_c(z,t)$:

$$\Delta P_{\mathrm{out}}(t) = S_{\mathrm{B,SPP}}\left(\frac{2}{l}\right) \int_0^{\infty} \Delta n_c(z,\, t) e^{-2z/l}\, \mathrm{d}z \tag{4}$$

The exponential term in eq 4 models the decay of the SPP intensity from the surface of the metal stripe ($z = 0$) into the solution. The SPP intensity is equal to $\mathrm{Re}\{S_y\}/2$, where S_y is the component of the Poynting vector in the direction of SPP propagation (y). The $1/e$ field decay length of the SPPs on a metal stripe waveguide into the bounding medium, l, depends on the confinement provided by the stripe.[29] In the case of our Bloch long-range SPP, the field decay length into the electrochemical solution is $l \approx 2$ μm, as determined from the mode field distribution computed at $\lambda_0 = 1310$ nm[23] and plotted as the inset to Figure 1b. The SPP intensity therefore drops to $1/e$ at $l/2 \approx 1$ μm.

Using eq 3, the power response of eq 4 becomes

$$\Delta P_{\mathrm{out}}(t) = S_{\mathrm{B,SPP}}\left(\frac{2}{l}\right) \int_0^{\infty} [\alpha_{\mathrm{O}} C_{\mathrm{O}}(z,\, t) + \alpha_{\mathrm{R}} C_{\mathrm{R}}(z,\, t)] e^{-2z/l}\, \mathrm{d}z \tag{5}$$

l is a weak function of $C_{\mathrm{O,\,R}}(z,\, t)$, so it is treated as a constant.

The diffusion times over the SPP intensity decay length, $(l/2)^2/(2D_{\mathrm{O,R}})$, where D_{O} and D_{R} [m^2/s] are the diffusion coefficients of the oxidized and reduced species, respectively, are less than a millisecond if the diffusion coefficients are in the range of 10^{-9} to 10^{-11} m^2/s, which is the case for many redox species.[30] If the power measurements (samples) are taken at time intervals that are much longer than the diffusion times, then the instantaneous response implied by eq 4 holds.

The time-dependent concentration distributions of the oxidized and reduced species, $C_{\mathrm{O,\,R}}(z,t)$, can be obtained by solving Fick's second law of diffusion:

$$\frac{\partial C_{\mathrm{O}}(z,\, t)}{\partial t} = D_{\mathrm{O}} \frac{\partial^2 C_{\mathrm{O}}(z,\, t)}{\partial z^2} \quad \text{and} \quad \frac{\partial C_{\mathrm{R}}(z,\, t)}{\partial t} = D_{\mathrm{R}} \frac{\partial^2 C_{\mathrm{R}}(z,\, t)}{\partial z^2} \tag{6}$$

The concentration distribution of the oxidized species, $C_{\mathrm{O}}(z,t)$, satisfying the first of eqs 6, is written as[31]

$$\begin{aligned} \frac{C_{\mathrm{O}}(z,\, t)}{C_{\mathrm{O}}^{\mathrm{b}}} &= 1 - \mathrm{erfc}\left(\frac{z}{\sqrt{4D_{\mathrm{O}}t}}\right) + \exp(\mu z + \mu^2 D_{\mathrm{O}} t) \\ &\quad \times \mathrm{erfc}\left(\frac{z}{\sqrt{4D_{\mathrm{O}}t}} + \mu\sqrt{D_{\mathrm{O}}t}\right) \end{aligned} \tag{7}$$

where μ is defined as

$$\mu = \frac{k^0}{D_{\mathrm{O}}} \exp\left(\frac{|\eta|}{b}\right) \tag{8}$$

with $b = RT/F$ (where R is the gas constant (J/(mol K))), T is the temperature (K), and F is the Faraday constant (C/mol). η is the overpotential (V), $\eta = E - E^0$, where E is the potential of the WE through which the current flows, and E^0 is the equilibrium potential established when no current flows. k^0 is the rate constant at zero potential (m/s). $C_{\mathrm{O}}^{\mathrm{b}} = C_{\mathrm{O}}\ (z,t = 0)$ is the initial concentration distribution of the oxidized species. The concentration distribution of the reduced species $C_{\mathrm{R}}(z,\, t)$ follows a similar form.

As it is evident from Figure S-1 in the Supporting Information, the concentration profiles reach $\sim C_{\mathrm{O,R}}^{\mathrm{b}}$ in a characteristic distance of several hundred micrometers from the electrode surface. Thus, $C_{\mathrm{O}}(z,t)$ and $C_{\mathrm{R}}(z,t)$ do not vary rapidly over $z = l/2 \approx 1$ μm, the characteristic decay length of our SPP intensity, so eq 5 can be simplified to

$$\Delta P_{\mathrm{out}}(t) = S_{\mathrm{B,SPP}}[\alpha_{\mathrm{O}} C_{\mathrm{O}}(0,\, t) + \alpha_{\mathrm{R}} C_{\mathrm{R}}(0,\, t)] \tag{9}$$

where $C_{\mathrm{O}}(0,t)$ and $C_{\mathrm{R}}(0,t)$ are the concentration of the oxidized and reduced species on the WE.

Based on eq 9, a relationship between $C_{\mathrm{O,R}}(0,t)$ and the electrochemical current is needed to connect the optical power response to the electrochemical current response. Fick's second law of diffusion (eqs 6), can be used for this purpose. The current density flowing through the WE in an electrochemical experiment, $j(t)$, is related to the normal derivative (gradient) of $C_{\mathrm{O,R}}(0,t)$ (eq 11):

$$j(t) = nFD_{\mathrm{O}} \left.\frac{\partial C_{\mathrm{O}}(z,\, t)}{\partial z}\right|_{z=0} = -nFD_{\mathrm{R}} \left.\frac{\partial C_{\mathrm{R}}(z,\, t)}{\partial z}\right|_{z=0} \tag{10}$$

where n is the number of electrons transferred per redox reaction. Using Laplace transforms,[11] eqs 6 are solved subject to the boundary conditions of eqs 10, leading to

$$C_{\mathrm{O}}(0,\, t) = C_{\mathrm{O}}^0 - [nF(\pi D_0)^{1/2}]^{-1} \int_0^t j(t')(t - t')^{-1/2}\, \mathrm{d}t' \tag{11}$$

$$C_R(0,\, t) = C_R^0 + [nF(\pi D_R)^{1/2}]^{-1} \int_0^t j(t')(t - t)'^{-1/2}\, \mathrm{d}t' \tag{12}$$

where $C_{\mathrm{O}}^0 = C_{\mathrm{O}}(0,0)$ and $C_{\mathrm{R}}^0 = C_{\mathrm{R}}(0,0)$ are the initial concentrations of redox species at the electrode surface.

The relationship between the power response and the current density can then be obtained by combining eqs 9, 11), and 12:

$$\Delta P_{\mathrm{out}}(t) = S_{\mathrm{B,SPP}}(\alpha_{\mathrm{O}}C_{\mathrm{O}}^{0} + \alpha_{\mathrm{R}}C_{\mathrm{R}}^{0}) + S_{\mathrm{B,SPP}}(\alpha_{\mathrm{R}}D_{\mathrm{R}}^{-1/2} - \alpha_{\mathrm{O}}D_{\mathrm{O}}^{-1/2}) \times (nF\pi^{1/2})^{-1}\int_0^t j(t')(t-t')^{-1/2}\,\mathrm{d}t' \quad (13)$$

The optical measurand is $P_{\mathrm{out}}(t)$, which can be written with the aid of eq 13 as

$$P_{\mathrm{out}}(t) = P_{\mathrm{out}}(0) + S_{\mathrm{B,SPP}}(\alpha_{\mathrm{R}}D_{\mathrm{R}}^{-1/2} - \alpha_{\mathrm{O}}D_{\mathrm{O}}^{-1/2})(nF\pi^{1/2})^{-1} \times \int_0^t j(t')(t-t')^{-1/2}\,\mathrm{d}t' \quad (14)$$

where $P_{\mathrm{out}}(0)$ is the initial output power measured before an electrochemical potential is applied:

$$P_{\mathrm{out}}(0) = P_{\mathrm{out}}(n_{\mathrm{e}}) + S_{\mathrm{B,SPP}}(\alpha_{\mathrm{O}}C_{\mathrm{O}}^{0} + \alpha_{\mathrm{R}}C_{\mathrm{R}}^{0}) \quad (15)$$

$P_{\mathrm{out}}(n_{\mathrm{e}})$ in the above equation is the output power measured for the electrolyte only. The second term in eq 15 originates from eq 13 and represents the change in output power due to the addition of the redox species to the electrolyte, but before application of the electrochemical potential. Therefore, $P_{\mathrm{out}}(0)$ is dependent explicitly on the initial concentrations of the redox species, $C_{\mathrm{O,\,R}}^{0}$. The second term in eq 14) is time-dependent and reveals that the output power evolves in time as the convolution of the electrochemical current density $j(t)$, similarly to the resonance angle in an SPR setup.[11]

In attenuation-based sensors,[26] the bulk sensitivity ($S_{\mathrm{B,SPP}}$) is dependent on the incident optical power (P_{inc}), such that increasing the incident power increases the sensitivity. To show this explicitly, we apply its definition (eq 2) to the second form of eq 1:

$$S_{\mathrm{B,SPP}} = \frac{\partial P_{\mathrm{out}}}{\partial n_{\mathrm{c}}} = P_{\mathrm{inc}}\frac{\partial T_{\mathrm{s}}}{\partial n_{\mathrm{c}}} = P_{\mathrm{inc}}S_{\mathrm{B,T_s}} \quad (16)$$

$S_{\mathrm{B,\,T_s}}$ (RIU^{-1}) is the power-independent bulk sensitivity of the sensing channel, which can be optimized by design. Substituting eq 16 into eq 14, we rewrite the output power as

$$P_{out}(t) = P_{\mathrm{out}}(0) + P_{\mathrm{inc}}S_{\mathrm{B,T_s}}(\alpha_{\mathrm{R}}D_{\mathrm{R}}^{-1/2} - \alpha_{\mathrm{O}}D_{\mathrm{O}}^{-1/2})(nF\pi^{1/2})^{-1} \times \int_0^t j(t')(t-t')^{-1/2}\,\mathrm{d}t' \quad (17)$$

From the above expression, we note that the output power scales linearly with P_{inc}, which is controlled independently from the electrochemical variables. This is a distinguishing feature from angular-interrogated EC-SPR systems.[11]

Isolating for $S_{\mathrm{B,T_s}}$ in the above yields

$$S_{B,T_s} = \frac{(P_{\mathrm{out}}(t) - P_{\mathrm{out}}(0))}{P_{\mathrm{inc}}} \times \frac{1}{(\alpha_{\mathrm{R}}D_{\mathrm{R}}^{-1/2} - \alpha_{\mathrm{O}}D_{\mathrm{O}}^{-1/2})(nF\pi^{1/2})^{-1}\int_0^t j(t')(t-t')^{-1/2}\,\mathrm{d}t'} \quad (18)$$

Thus, $S_{\mathrm{B,T_s}}$ can be determined by inserting the optical and electrical measurands, $P_{\mathrm{out}}(t)$ and $j(t)$, into eq 18. $S_{\mathrm{B,T_s}}$ is optimized by design about an electrolyte refractive index, n_{e}, and is independent of the redox species and its concentration, of the electrochemical technique applied, and of any associated electrochemical variables (e.g., scan rate, step potential).

■ EXPERIMENTAL SECTION

Setup. As sketched in Figure 1a, the sensing chip consists of a Au stripe SPP waveguide operating simultaneously as a WE, bearing input and output optical grating couplers, next to a Pt stripe used as the counter electrode (CE). The structures were fabricated on a Si wafer bearing a multilayer dielectric stack consisting of 15 periods of SiO_2 and Ta_2O_5, as sketched in Figure 1b. The dimensions of the structures, given in the caption to Figure 1a, and the design of the multilayer stack, were selected such that SPPs propagate along the Au stripe as Bloch long-range SPPs at $\lambda_0 \approx 1310$ nm. These modes propagate with fields confined in the 2D plane normal to the direction of propagation (y) and that decay exponentially away from the stripe, penetrating the electrolyte a distance $l \approx 2$ μm, thereby probing the region nearest the stripe. Thick Pt/Cu electrical contact pads were also fabricated to facilitate electrical probing of the stripes. Further details on fabrication and the optical operation of the waveguides can be found in previous reports.[24,25,32]

A chip was fixed to the bottom of a Petri dish and submerged by the redox species in electrolyte. Electrochemical reactions were driven from the WE and CE on chip, using two tungsten needles coated with PMMA (except for their tips), to prevent any electrochemical interference during the measurements. The probing needles were attached to the arms of two positioners and used to probe the contact pads of a Au WE and a Pt CE directly. The Au WE, Pt CE and a Ag/AgCl reference electrode (double junction PH combination, glass body, BNC connector, Sigma-Aldrich Canada, Ltd.) form a three-electrode system, driven by a potentiostat (WaveDriver20, Pine Research Instrumentation, Inc.) to perform cyclic voltammetry (CV) and chronoamperometry measurements.

The experimental scheme made use of a cleaved bow-tie style polarization-maintaining single-mode optical fiber (PM-SMF) with a core diameter of 6.6 μm, aligned perpendicularly to the input grating coupler to launch the incident beam that excites SPPs along the WE. The output grating coupler converts the SPPs to the output beam emerging normally from the chip, which was captured by a large-core (200 μm diameter) multimode fiber (MMF). Both fibers were mounted to 90° metallic holders on multiaxis micropositioners. A tunable laser (Agilent, Model 8164A) was coupled to the input of the PM-SMF, and a power meter (Thorlabs, Model PM 100USB) was used to capture power output from the MMF, enabling the power transmitted by SPPs along the WE to be continuously monitored in situ. The wavelength of operation (λ_0 = 1350 nm) was set in situ by maximizing the power transmitted along a WE while tuning the laser.

Materials - Redox Species and Electrolyte. Potassium ferricyanide ($K_3[Fe(CN)_6]$) and potassium nitrate (KNO_3) were used as supplied (both >99% purity, Sigma−Aldrich), as the redox species and electrolyte, respectively. The electrolyte covers the WE and CE and, as such, also serves as the optical upper cladding through which SPPs on the WE propagate. In order for Bloch long-range SPPs to be supported on the WE,[24] glycerol was added to the electrolyte to adjust its refractive index to n_{e} = 1.3323 (at λ_0= 1312 nm) as measured using a prism coupler (Metricon) - adding a small amount of glycerol has no effect on the electrochemical response of our redox couple, as verified in previous work.[23] Specifically, 0.2928 g of glycerol (99.5% purity, Sigma−Aldrich) was added per 20 mL of electrolyte, the latter consisting of 100 mM KNO_3 in distilled deionized H_2O. Thus, the electrolyte solution used throughout our study consisted of 100 mM KNO_3 + 158.5 mM glycerol, into which the redox species $K_3[Fe(CN)_6]$ was dissolved to concentrations of x mM, where $x = 0.5, 1, 3, 5$ mM.

Potassium ferricyanide and potassium ferrocyanide form a redox couple in a reversible reaction involving a one-electron transfer process, from potassium ferricyanide ($K_3[Fe(CN)_6]$) to potassium ferrocyanide ($K_4[Fe(CN)_6]$):

$$K_4[Fe(CN)_6] \leftrightarrow K_3[Fe(CN)_6] + e \tag{19}$$

The diffusion coefficient of potassium ferricyanide (D_0) in our electrolyte was reported as 4.18×10^{-10} m^2/s.[31] The diffusion coefficient of potassium ferrocyanide (D_R) in our electrolyte was obtained by fitting CV measurements to the Randles−Sevcik equation,[31] yielding 3.56×10^{-10} m^2/s.

The change in refractive index per unit concentration of potassium ferricyanide ($K_3[Fe(CN)_6]$), α_O, is needed to connect the experimental results with theory. The refractive index of our four concentrations of potassium ferricyanide, C_O = 0.5, 1, 3, 5 mM (0.35, 0.69, 2.07, and 3.45 mol/m^3), dissolved in our electrolyte, were measured using a prism coupler (Metricon) at λ_0= 1312 nm and plotted in Figure S-2 in the Supporting Information. Fitting eq 3 with $C_R = 0$ to the data yields $\alpha_O = 0.0003$ m^3/mol as the slope, and $n_e = 1.3323$ as the intercept ($C_O = 0$). We approximate α_R as α_O because potassium ferricyanide and potassium ferrocyanide are similar molecules, surmised to elicit a similar optical polarizability.

■ RESULTS AND DISCUSSION

Chronoamperometric Responses at Low Optical (SPP) Power. Chronoamperometric measurements were obtained using an on-chip WE and CE, following the experimental scheme sketched in Figure 1a and described in the previous subsections. The chronoamperometric responses of four concentrations of potassium ferricyanide (C_O = 0.5, 1, 3, 5 mM) in our electrolyte were measured under low incident optical power. The incident optical power was set to P_{inc} = 0.794 mW (−1 dBm), which is low enough to ensure that the SPPs propagating along the WE do not affect the electrochemical response and serve only as a probe of electrochemical activity thereon. A forward step potential from 0 to 450 mV (vs. Ag/AgCl) was applied to induce oxidation of the redox species on the WE. The measured current density $j(t)$ is plotted in Figure 2a and the corresponding output optical power, measured simultaneously, $P_{out}(t)$, is plotted in Figure 2b. Figure 2a shows a clear dependence of the current responses on the concentration as expected.

Using the α_R, α_O, D_R, and D_O values given in the previous section, with $n = 1$ and P_{inc} = 0.794 mW, S_{B,T_s} can be obtained over the time frame of the chronoamperometric responses by using eq 18 with the measured responses of $j(t)$ and $P_{out}(t)$ (Figures 4a and 4b, presented later in this work). In doing so, the time $t = 0$ was taken as the time immediately before application of the step potential (i.e., $P_{out}(0) = P_{out}(0^-)$), and the time convolution of $j(t)$ was computed by numerical integration. Figure S-3 in the Supporting Information plots S_{B,T_s} over the duration of the experiment for the four concentrations of potassium ferricyanide investigated. S_{B,T_s} is constant over time and over concentration—this is expected because S_{B,T_s} (bulk sensitivity of the sensing channel) is set by design and is independent of the redox species and its concentration, of the electrochemical technique applied, and of any associated electrochemical variables. This result also implicitly validates that output optical power evolves in time as the convolution of the electrochemical current density. The value of S_{B,T_s} averaged over time and over all concentrations is 0.0227 [RIU^{-1}], which yields 18.023 [W/RIU] for $S_{B,SPP}$ at P_{inc} = 0.794 mW.

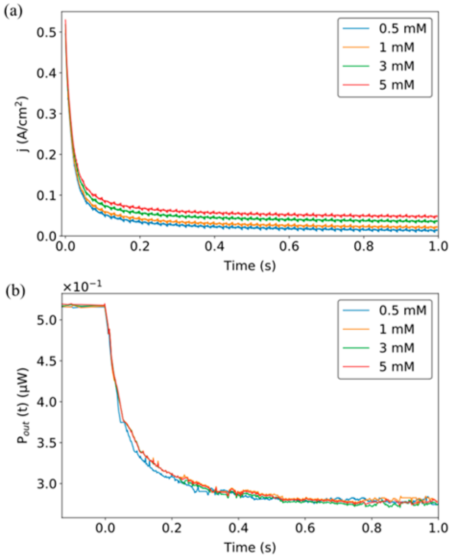

Figure 2. (a) Chronoamperometric responses to a 450 mV (vs. Ag/AgCl) potential step, for different concentrations of potassium ferricyanide $K_3[Fe(CN)_6]$ (legend), in our electrolyte (100 mM KNO_3 + 158.5 mM glycerol), under low-power SPP excitation. (b) Measured output optical power at λ_0 = 1350 nm versus time as the responses in panel (a) were recorded.

Cyclic Voltammetry at Low Optical (SPP) Power. Cyclic voltammetry (CV) measurements were obtained with 0.5 mM of potassium ferricyanide in electrolyte, at a scan rate of 100 mV/s over a potential window of 0 to 500 mV (vs. Ag/AgCl) to drive the reversible reaction of eq 19. Figure 3a shows the triangular voltage waveform applied to obtain the CV measurements. Figure 3b shows the measured current density versus time over one period of the drive voltage. The incident optical power was again set to P_{inc} = 0.794 mW to probe electrochemical activity on the WE. The corresponding output optical power measured simultaneously is plotted in Figure 3c, along with that calculated using eq 17 with the current density measured in Figure 3b, using numerical integration, $n = 1$, and the coefficients α_R, α_o, D_R, D_O, and S_{B,T_s} given in the previous subsections. Very good agreement between the measured and computed power responses is noted from Figure 3c, explicitly confirming that the power response follows the time convolution of the current density.

Equation 17 states that the output optical power is not dependent explicitly on electrochemical variables, such as the scan rate in CV measurements. To verify this, CV measurements were obtained for different scan rates (20, 50, and 100 mV/s) while monitoring the output optical power due to SPPs propagating along the WE (P_{inc} = 0.794 mW).

Figure 4a shows the measured cyclic voltammograms, revealing that the peak current density increases by more than 2-fold when the scan rate increases from 20 mV/s to 100 mV/s. The corresponding output optical powers measured

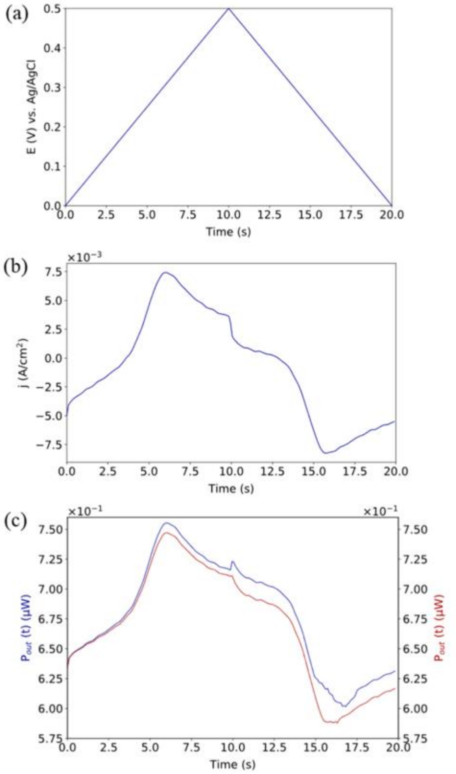

Figure 3. (a) Triangular voltage waveform to obtain CV measurements at a scan speed of 100 mV/s. (b) Current density versus time measured over one voltage period on a Au WE immersed in 0.5 mM $K_3[Fe(CN)_6]$ in our electrolyte (100 mM KNO_3 + 158.5 mM glycerol), under low-power SPP excitation. (c) Measured (blue) and computed (red) output optical power responses at λ_0 = 1350 nm, over the same voltage period as in panel (b).

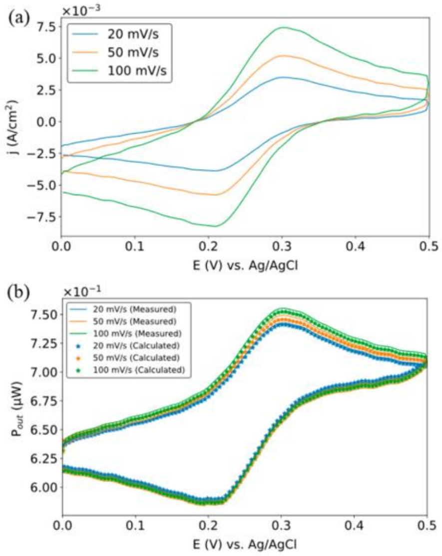

Figure 4. (a) Current density voltammograms on a Au WE immersed in 0.5 mM of $K_3[Fe(CN)_6]$ in our electrolyte (100 mM KNO_3 + 158.5 mM glycerol), at various scan rates (legend), under low-power SPP excitation. (b) Power voltammograms measured simultaneously with the current density voltammograms of panel (a) at λ_0= 1350 nm (solid curves). The corresponding computed voltammograms are also plotted (stars).

simultaneously are plotted as the power voltammograms of Figure 4b, along with those computed using eq 17 with the measured current densities of Figure 4a, revealing good agreement. Essentially no dependence on scan rate is observed in Figure 4b, as the measured power voltammograms collapse essentially to a single curve. The power voltammograms also confirm that the propagating SPPs probe primarily changes in refractive index between the reduced and oxidized forms of the redox species (potassium ferricyanide).

Cyclic Voltammetry at High Optical (SPP) Power. CV measurements were then obtained in 0.5 mM of potassium ferricyanide in our electrolyte, at a scan rate of 100 mV/s, with SPPs propagating along the Au WE excited at increasing incident optical powers, P_{inc}, such that energetic carriers increasingly affect redox currents, while monitoring the output optical power. In this case, the SPPs not only serve to probe electrochemical activity on the WE, but also to open (pump) new redox channels involving energetic carriers.

The measured cyclic voltammograms are plotted in Figure 5a, including a reference curve with the laser off plotted as the black curve. From the data plotted in Figure 5a, the peak oxidation and reduction current densities and the potentials corresponding to the peak currents are identified as a function of incident optical power and plotted in Figure 5b. From Figure 5b, it is noted that the redox current densities increase by up to 10-fold and the oxidation, reduction, and equilibrium potentials decrease by up to 2-fold with increasing SPP excitation, P_{inc}, beyond a threshold at $P_{inc} \approx 1$ mW. These changes are due to energetic carriers created along the WE as SPPs propagate and are absorbed therein. Energetic electrons transfer more readily than electrons at equilibrium from the WE to the redox species thereby enhancing the reduction current, and energetic holes transfer more readily from the WE to enhance the oxidation current. The threshold at $P_{inc} \approx 1$ mW indicates the opening of these redox channels as the current densities associated with energetic carrier transfer overcome noise and the equilibrium redox current densities. (Extensive and in situ thermal control experiments performed in previous work on a similar setup rule out thermal effects as the cause of the current increase.[23])

The corresponding output optical power measured simultaneously is plotted in Figure 5c as power voltammograms. Figure 5c reveals two important features. The first is the power scaling implied by eq 17, which states that the convolved signal (P_{out}) scales to larger powers with increasing P_{inc}, independently of the electrochemical variables—this is observable as voltammograms that rise on the plot with increasing P_{inc}. This feature is useful for improving the signal-to-noise ratio of the measurement. The second is that the power voltammograms open as P_{inc} increases—a feature better observed from the normalized voltammograms of Figure 5d. The opening is particularly noteworthy beyond threshold ($P_{inc} > 1$ mW),

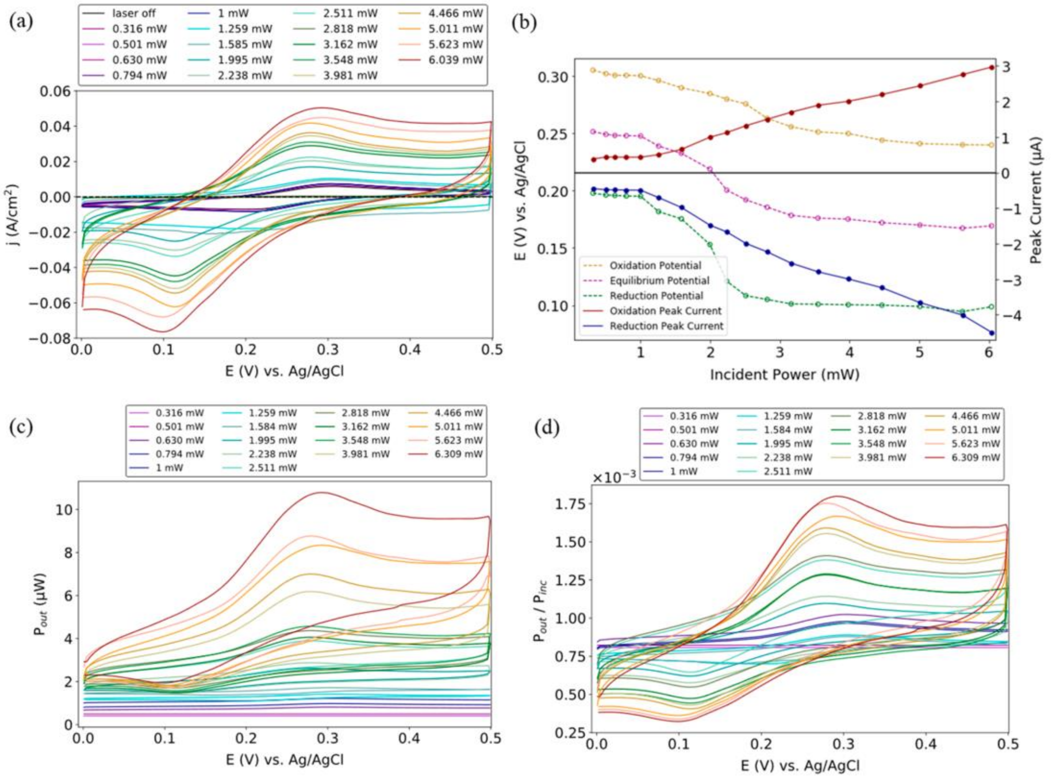

Figure 5. (a) Current density voltammograms obtained on a Au WE immersed 0.5 mM of $K_3[Fe(CN)_6]$ in our electrolyte (100 mM KNO_3 + 158.5 mM glycerol), at a scan rate of 100 mV/s, with the WE supporting propagating SPPs excited at the incident optical powers (P_{inc}) indicated in the legend. (b) Peak oxidation and reduction currents and corresponding potentials (oxidation, reduction, equilibrium) vs incident optical power, summarized from panel (a). (c) Power voltammograms measured simultaneously with the current density voltammograms of panel (a), for the incident optical powers (P_{inc}) indicated in the legend. (d) Power voltammograms of panel (c), normalized to the incident power, P_{inc}.

where energetic carrier transfer significantly affects the current density.

Figure 6 compares three of the normalized voltammograms of Figure 5d measured at three values of P_{inc} above threshold (P_{inc} > 1 mW), with normalized voltammograms computed via eq 17, using the corresponding measured current densities of Figure 5a. Excellent agreement is noted, indicating that P_{out} remains proportional to the time convolution of the current density.

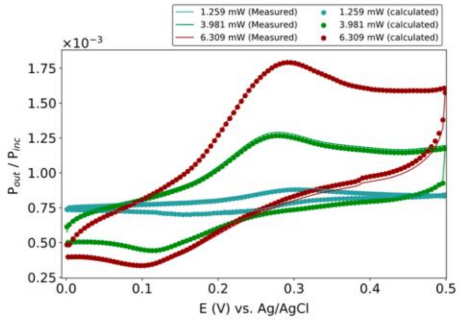

Figure 6. Normalized power voltammograms beyond threshold, from Figure 5, compared to the corresponding computed ones.

High SPP powers open new redox channels associated with energetic carriers, which not only enhance the electrochemical current densities (Figure 5a), but also their convolution as directly measured via the output optical power (Figure 5d). Enhanced convolution implies that the concentration of electroactive species at the WE is also enhanced (eq 9), the result of increased reaction rates which follow enhanced current densities, as energetic carriers transfer more readily to the redox species.

■ CONCLUSIONS

We investigated a Au stripe waveguide along which SPPs propagate, operating simultaneously as an electrochemical electrode. Theory relating the real-time response of the output optical power to the time convolution of the current density was developed and validated experimentally via chronoamperometry measurements obtained at different concentrations of the redox species, and cyclic voltammetry measurements obtained at different scan rates. The bulk optical sensitivity of the waveguide WE, S_{B,T_s}, was determined by simultaneously fitting the measured optical power and current density from chronoamperometric responses to a theoretical relationship linking them.

At low power, the SPPs propagating along the WE probe changes in refractive index between the reduced and oxidized forms of the redox species. Increasing the SPP power drives redox reactions involving energetic carriers (hot electrons and holes) created by SPP absorption in the Au WE, leading to significantly enhanced redox current densities and convolution signals. Enhanced convolution implies that the concentrations of electroactive species at the WE are also enhanced, because of increased reaction rates which follow increased current densities, as energetic carriers transfer more readily to the redox species.

Thus, exciting SPPs along a working electrode is useful not only as a probe of electrochemical activity, but also to drive significant electrochemical enhancement. The output optical power follows in real time the convolution of the electrochemical current density, yielding results that are complementary.

■ ASSOCIATED CONTENT

Supporting Information

The Supporting Information is available free of charge at https://pubs.acs.org/doi/10.1021/acs.analchem.2c02643.

> Computed concentration profiles of potassium ferricyanide as a function of z and the distance from the WE (Figure S-1); refractive index of the electrochemical solution, n_c, vs concentration of potassium ferricyanide (Figure S-2); S_{B,T_s} extracted over the duration of the chronoamperometric responses of Figure 2 (same legend) (Figure S-3) (PDF)

■ AUTHOR INFORMATION

Corresponding Author

Pierre Berini – *Department of Physics, University of Ottawa, Ottawa, Ontario K1N 6N5, Canada; School of Electrical Engineering and Computer Science, University of Ottawa, Ottawa, Ontario K1N 6N5, Canada;* orcid.org/0000-0002-6795-7275; Email: berini@eecs.uottawa.ca

Authors

Zohreh Hirbodvash – *Department of Physics, University of Ottawa, Ottawa, Ontario K1N 6N5, Canada;* orcid.org/0000-0002-2188-2431

Elena A. Baranova – *Department of Chemical and Biological Engineering and Centre for Catalysis Research and Innovation, University of Ottawa, Ottawa, Ontario K1N 6N5, Canada;* orcid.org/0000-0001-5993-2740

Complete contact information is available at: https://pubs.acs.org/10.1021/acs.analchem.2c02643

Notes

The authors declare no competing financial interest.

■ REFERENCES

(1) Imbeaux, J. C.; Saveant, J. M. *J. Electroanal. Chem. Interfacial Electrochem.* **1973**, *44*, 169–187.

(2) Woodard, F. E.; Goodin, R. D.; Kinlen, P. J. *Anal. Chem.* **1984**, *56*, 1920–1923.

(3) Pilo, M. I.; Sanna, G.; Seeber, R. J. *Electroanal. Chem.* **1992**, *323*, 103–115.

(4) Muthukrishnan, A.; Sangaranarayanan, M. V. *Electrochim. Acta* **2010**, *55*, 1664–1669.

(5) Murthy, A.; Manthiram, A. *Electrochim. Acta* **2011**, *56*, 6078–6083.

(6) Samec, Z.; Trojánek, A.; Langmaier, J.; Samcová, E. J. *Electroanal. Chem.* **2000**, *481*, 1–6.

(7) Nadjo, L.; Saveant, J. M.; Tessier, D. J. *Electroanal. Chem.* **1974**, *52*, 403–412.

(8) Bard, A. J; Faulkner, L. R. *Electrochemical Methods: Fundamentals and Applications*, 2nd Edition; Wiley: New York, 2001.

(9) Gordon, J. G.; Ernst, S. *Surf. Sci.* **1980**, *101*, 499–506.

(10) Szunerits, S.; Boukherroub, R. *Electrochem. Commun.* **2006**, *8*, 439–444.

(11) Wang, S.; Huang, X.; Shan, X.; Foley, K. J.; Tao, N. *Anal. Chem.* **2010**, *82*, 935–941.

(12) Bentley, C. L.; Bond, A. M.; Hollenkamp, A. F.; Mahon, P. J.; Zhang, J. *Anal. Chem.* **2014**, *86*, 2073–2081.

(13) Zhang, Y.; Guo, W.; Zhang, Y.; Wei, W. D. *Adv. Mater.* **2021**, *33*, 2006654.

(14) Sundararaman, R.; Narang, P.; Jermyn, A. S.; Goddard, G. A., III; Atwater, H. A. *Nat. Commun.* **2014**, *5*, 5788.

(15) Zhou, L.; Swearer, D. L.; Zhang, C.; Robatjazi, H.; Zhao, H.; Henderson, L.; Dong, L.; Christopher, P.; Carter, E. A.; Nordlander, P.; Halas, N. J. *Science* **2018**, *362*, 69–72.

(16) Baffou, G.; Bordacchini, I.; Baldi, A.; Quidant, R. *Light Sci. Appl.* **2020**, *9*, 108.

(17) Dubi, Y.; Un, I. W.; Sivan, Y. *Chem. Sci.* **2020**, *11*, 5017.

(18) Yu, Y.; Williams, J. D.; Willets, K. A. *Faraday Discuss.* **2018**, *210*, 29–39.

(19) Yu, Y.; Sundaresan, V.; Willets, K. A. J. *Phys. Chem. C* **2018**, *122*, 5040–5048.

(20) Maley, M.; Hill, J. W.; Saha, P.; Walmsley, J. D.; Hill, C. M. J. *Phys. Chem. C* **2019**, *123*, 12390–12399.

(21) Zhan, C.; Liu, B.-W.; Huang, Y.-F; Hu, S.; Ren, B.; Moskovits, M.; Tian, Z.-Q. *Nat. Commun.* **2019**, *10*, 2671.

(22) Wilson, A. J.; Mohan, V.; Jain, P. K. J. *Phys. Chem. C* **2019**, *123*, 29360–29369.

(23) Hirbodvash, Z.; Krupin, O.; Northfield, H.; Olivieri, A.; Baranova, E. A.; Berini, P. *Sci. Adv.* **2022**, *8*, eabm9303.

(24) Fong, N. R.; Menotti, M.; Lisicka-Skrzek, E.; Northfield, H.; Olivieri, A.; Tait, R. N.; Liscidini, M.; Berini, P. *ACS Photonics* **2017**, *4*, 593–599.

(25) Khodami, M.; Berini, P. J. *Opt. Soc. Am. B* **2019**, *36*, 1921–1930.

(26) Wong, W. R.; Krupin, O.; Mahamd Adikan, F. R.; Berini, P. J. *Lightw. Technol.* **2015**, *33*, 3234–3242.

(27) Krupin, O.; Wong, W. R.; Mahamd Adikan, F. R.; Berini, P. *IEEE J. Sel. Top. Quant. Electr.* **2017**, *23*, 103–112.

(28) Berini, P. *New J. Phys.* **2008**, *10*, 105010.

(29) Berini, P. *Adv. Opt. Photon.* **2009**, *1*, 484–588.

(30) Lequin, S.; Chassagne, D.; Karbowiak, T.; Simon, J.-M.; Paulin, C.; Bellat, J.-P. J. *Agri. Food Chem.* **2012**, *60*, 3348–3356.

(31) Hirbodvash, Z.; Houache, M. S. E.; Krupin, O.; Khodami, M.; Northfield, H.; Olivieri, A.; Baranova, E. A.; Berini, P. *Chemosensors* **2021**, *9*, 277.

(32) Khodami, M.; Hirbodvash, Z.; Krupin, O.; Wong, W. R.; Lisicka-Skrzek, E.; Northfield, H.; Hahn, C.; Berini, P. J. *Microelectromech. Syst.* **2021**, *30*, 686–695.

Supporting Information

Real-time convolutional voltammetry enhanced by energetic (hot) electrons and holes on a surface plasmon waveguide electrode

Zohreh Hirbodvash,[1] Elena A. Baranova,[2,3] and Pierre Berini[1,4,*]
[1]Dept. of Physics, University of Ottawa, 150 Louis Pasteur, Ottawa, Ontario, K1N 6N5, Canada
[2]Department of Chemical and Biological Engineering, University of Ottawa, 161 Louis-Pasteur, Ottawa, ON K1N 6N5, Canada
[3]Centre for Catalysis Research and Innovation, University of Ottawa, 161 Louis-Pasteur, Ottawa, ON K1N 6N5, Canada
[4]School of Electrical Engineering and Computer Science, University of Ottawa, 800 King Edward Ave., Ottawa, Ontario, K1N 6N5, Canada
*Corresponding Author; berini@eecs.uottawa.ca

Figure S1 plots the computed concentration profiles for 0.5 mM potassium ferricyanide in 100 mM potassium nitrate electrolyte, corresponding to our experimental system of interest, as a function of *z*, the distance from the WE. Following [31], E was set to 0.3 V in the forward direction, corresponding to the oxidation peak. The equilibrium potential is $E^0 = 0.24$ V (other data can be found in [31]). The concentration profiles, plotted $t = 6$ s after application of the potential, indicate a high concentration of the oxidised form on the WE ($z = 0$), along with a low concentration of the reduced form, as expected after application of the (peak) oxidising potential.

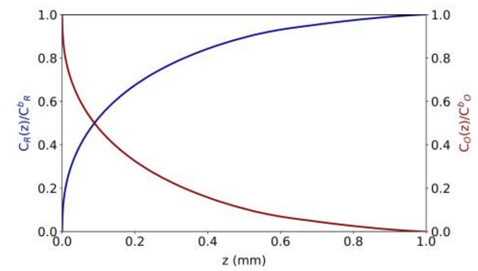

Figure S1. Computed concentration profiles of potassium ferricyanide as a function of *z*, the distance from the WE, $t = 6$ s after application of the (peak) oxidising potential (0.3V *vs*. Ag/AgCl reference electrode).

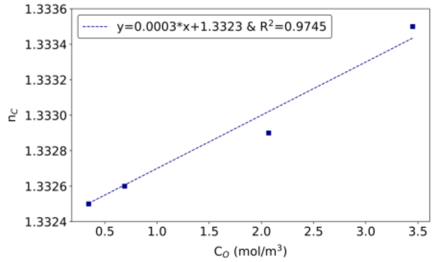

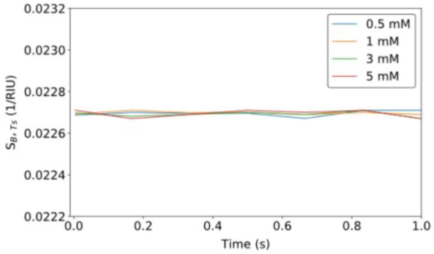

Figure S2. Refractive index of the electrochemical solution, n_c, *vs.* concentration of potassium ferricyanide $K_3[Fe(CN)_6]$, C_O, in our electrolyte (100 mM KNO_3 + 158.5 mM glycerol). Best fit of Eq. (3) given in legend.

Figure S3. S_{B,T_s} extracted over the duration of the chronoamperometric responses of Figure 2 (same legend).

Chapter 7.

Conclusion and Future Work

7.1. Conclusion

Straight Au waveguides bearing grating couplers embedded in Cytop, supporting LRSPPs were investigated and used to determine grating coupling efficiencies using a cleaved bow-tie PM fiber and a lensed PM fiber over a broad operating wavelength range. The bow-tie PM fiber aligned with a lensed PM fiber was found to have input coupling losses of about 20 dB whereas an aligned lensed PM fiber showed input coupling losses of about 9 dB. A numerical calculation was also performed to find coupling loss and grating coupling efficiencies for both types of fibers. There is good agreement between the measured and theoretical coupling losses. The samples were designed to operate at 1310 nm, although the minimum coupling loss was found around 1345 nm. AFM images obtained on an etched grating coupler reveal that the fabricated structures have a slight out-of-plane curvature, possibly induced during fabrication (e-beam exposure), explaining the observed shift and slight increase in coupling losses as corroborated through modeling. Grating couplers simplify optical alignments and remove the need for high-quality end facets. Furthermore, uncoupled light propagates orthogonally to the excited waveguide mode and is thus less likely to cause interference with the output at detection opto-electronics.

Over a limited range of wavelengths and wavenumbers, a truncated 1DPC can replace a lower cladding such as Cytop to support Bloch LRSPPs. We used grating couplers as input/output excitation means where a Gaussian beam emerging from an aligned polarization-maintaining single-mode fibre excites Bloch LRSPPs on a Au waveguide on a truncated 1DPC covered by Cytop. Bloch LRSPP waveguides incorporating grating couplers were integrated with Pt electrodes to form an electrochemical sensor. Planar waveguides were integrated into arrays capable of multichannel multimodal biosensing. The device was fabricated using photolithography and overlaid electron-beam lithography and was covered with Cytop as the upper cladding to create etched microfluidic channels and the sensing window over a portion of the waveguide.

Bloch LRSPP waveguides with grating couplers were integrated with Pt electrodes to create an electrochemical sensor. Before conducting electrochemical measurements, microelectrodes must be "burned-in" (current annealed). As the redox species, potassium ferricyanide was in chronoamperometry and cyclic voltammetry (CV) at various scan rates. Fitting our experimental data to the Randles-Sevcik equation yields the diffusion coefficient of potassium ferricyanide. Using chips, CV measurements are compared to commercial macroscopic electrodes. We compare experimentally obtained CV values with theoretical results derived from the Butler-Volmer equation while extracting the rate constant for our redox species at zero potential.

Lastly, electrochemical plasmonic catalysis with surface plasmon waveguides and infrared light was reported. Under plasmonic excitation, the redox current density increases by 10×. Optical power also reduces oxidation, reduction, and equilibrium potentials by as much as

2×. As photon energy increases, redox potentials drop beyond threshold, demonstrating optical control of redox potentials. We use infrared photons with lower energies (λ_0 ~ 1350 nm, $h\upsilon$ ~ 1 eV) to excite SPPs and energetic carriers in Au. Since the main carrier damping mechanism is electron-phonon scattering, these carriers have energies at most one eV above E_F, and attenuation lengths > 55 nm (L_e ~ 74 nm, L_h ~ 55 nm) which enhances carrier escape probability in thin electrodes.

Convolutional voltammetry is performed during CV and chronoamperometry measurements by monitoring the SPP output power versus the applied voltage. By using both experimental and theoretical methods, we demonstrate that the SPP output power is proportional to the electrochemical current convolution. The SPP voltammetry confirms that signal changes are mainly caused by differences in refractive indices between reduced and oxidized forms of redox species. Furthermore, we demonstrate that energetic carriers resulted from SPP absorption significantly improved electrochemical sensitivity.

An Au stripe waveguide propagates SPPs and works simultaneously as an electrochemical WE are investigated. We developed a theory that relates the actual output optical power to the convolution of the current density over time using chronoamperometry measurements at different concentrations of redox species along with cyclic voltammetry measurements at different scanning rates. Using a theoretical relationship linking both the measured optical power and the measured current density of the waveguide WE, the bulk optical sensitivity was determined. The scan rate of optical power voltammograms is independent of CV measurements. SPPs propagating along the WE probe primarily changes in refractive index between the reduced and oxidised forms of redox species. Increasing the

SPP power induces redox reactions involving energetic carriers (electrons, holes) created by SPP absorption in Au WE, resulting in significantly enhanced redox current densities and convolution signals.

7.2. Future work

New possibilities for disease detection are opened by the present work. LRSPP optical biosensors as well as electrochemical sensors can be combined in a multi-modality platform for detecting biochemical and ionic markers of disease states.

One possible direction is developing assays and protocols for the simultaneous optical and electrochemical biodetection of diabetes markers, HbA1c and glucose, respectively. Such a biodetection platform can help manage diabetes by monitoring markers that vary daily (glucose) using electrochemical part and over a period of 3 months (HbA1c) with the optical platform.

It is possible to observe the same plasmonic enhancement in other redox species with the platform used in chapters 5 and 6.

Electrochemical detection limits under the excitation of energetic carriers can be further studied, specifically, by comparing Au waveguide electrodes under optical illumination, with Au waveguide electrodes without illumination, building on the results of Chapters 5 and 6. Specifically, the detection limit for glucose could be investigated using the same redox couple as the reported with and without an optical excitation.

References

[1] M. Jia, S. Li, L. Zang, X. Lu, H. Zhang, "Analysis of Biomolecules Based on the Surface Enhanced Raman Spectroscopy," Nanomaterials **8**, 730 (2018).

[2] N. Bhalla, P. Jolly, N. Formisano, N. P. Estrela, "Introduction to biosensors," Essays in Biochemistry **60**, 1-8 (2016).

[3] M.A. Cooper, "Optical biosensors in drug discovery," Nature reviews Drug Discovery **1** ,515-528 (2002).

[4] R.M. Lequin, "Enzyme Immunoassay (EIA)/Enzyme-Linked Immunosorbent Assay (ELISA)," Clinical chemistry **51**, 2415-2418 (2005).

[5] Z. Sun, J. Lv, X. Liu, Z. Tang, X. Wang, Y. Xu, B.D. Hammock, "Development of a Nanobody-AviTag Fusion Protein and Its Application in a Streptavidin-Biotin- Amplified Enzyme-Linked Immunosorbent Assay for Ochratoxin A in Cereal," Analytical chemistry **90**, 10628-10634 (2018).

[6] T. Endo, A. Okuyama, Y. Matsubara, K. Nishi, M. Kobayashi, S. Yamamura, Y. Morita, Y. Takamura, H. Mizukami, E. Tamiya, "Fluorescence-based assay with enzyme ampli_cation on a micro-ow immunosensor chip for monitoring coplanar polychlorinated biphenyls," Analytica chimica acta **531**, 7-13 (2005).

[7] F. Yuan, M. Chen, B.Y. Leng, B.S. Wang, "An efficient autouorescence method for screening Limonium bicolor mutants for abnormal salt gland density and salt secretion," South African Journal of Botany **88**, 110-117 (2013).

[8] Y. Deng, Z. Feng, F. Yuan, J. Guo, S. Suo, B. Wang, "Identification and functional analysis of the autouorescent substance in Limonium bicolor salt glands," Plant Physiology and Biochemistry **97**, 20-27 (2015).

[9] E. Harris, "A Low-Cost Approach to PCR: Appropriate Transfer of Biomolecular Techniques," Oxford University Press (1998).

[10] L. Chang, J. Li, L. Wang, “Immuno-PCR: An ultrasensitive immunoassay for biomolecular Detection,” Analytica chimica acta **910**, 12-24 (2016).

[11] T.Chard, “Introduction to radioimmunoassay and related techniques. Radioimmunologicheskie metody,” (1981).

[12] R. Liu, Y. Xiong, W. Tang, Y. Guo, X. Yan, M. Si, “Near-infrared surface-enhanced Raman spectroscopy (NIR-SERS) studies on oxyheamoglobin (OxyHb) of liver cancer based on PVA-Ag nanofilm,” Journal of Raman Spectroscopy **44**, 362-369 (2013).

[13] M. Munch, L.P. Nielsen, K.J. Handberg, P.H. JØrgensen, “Detection and subtyping (H5 and H7) of avian type A inuenza virus by reverse transcription-PCR and PCR-ELISA,” Archives of virology **146**, 87-97 (2001).

[14] P. Daly, T. Collier, S. Doyle, “PCR-ELISA detection of Escherichia coli in milk,” Letters in Applied Microbiology **34**, 222-226 (2002).

[15] I.L. Medintz, A.R. Clapp, J.S. Melinger, J.R. Deschamps, H. Mattoussi, “A reagentless biosensing assembly based on quantum dot--donor Forster resonance energy transfer,” Advanced Materials **17**, 2450-2455 (2005).

[16] D. Nedelkov, R.W. Nelson,” Practical considerations in BIA/MS: optimizing the biosensor—mass spectrometry interface,” Journal of Molecular Recognition **13**, 140-145 (2000).

[17] C. Yao, T. Zhu, Y. Qi, Y. Zhao, H. Xia, W. Fu, “Development of a quartz crystal microbalance biosensor with aptamers as bio-recognition element,” **10**, 5859-5871 (2010).

[18] J. Dostálek, J. Čtyroký, J. Homola, E. Brynda, M. Skalský, P. Nekvindová, J. Špirková, J. Škvor, J. Schröfel, “Surface plasmon resonance biosensor based on integrated optical waveguide,” Sensors and actuators B **76**, 8-12 (2001).

[19] A.J. Haes, R.P. Van Duyne," A unified view of propagating and localized surface plasmon resonance biosensors," Analytical and bioanalytical chemistry **379**, 920-930 (2004).

[20] O. Krupin, H. Asiri, C. Wang, R.N. Tait, P. Berini, "Biosensing using straight long-range surface plasmon waveguides, " **21**, 698-709 (2013).

[21] M. Watanabe, K. Kajikawa, "An optical fiber biosensor based on anomalous reflection of gold," Sensors and Actuators B: Chemical **89**, 126-130 (2003).

[22] J. Yoon, M. Shin, T. Lee, J.W. Choi, "Highly sensitive biosensors based on biomolecules and functional nanomaterials depending on the types of nanomaterials: A perspective review," Materials **13**, 299 (2020).

[23] J. Homola, "Surface plasmon resonance sensors for detection of chemical and biological Species," Chemical reviews **108**, 462-493 (2008).

[24] D. Tang, R. Yuan, Y. Chai, Y. Liu, J.J. Dai, X. Zhong, "Novel potentiometric immunosensor for determination of diphtheria antigen based on compound nanoparticles and bilayer two-dimensional sol-gel as matrices," Analytical and Bioanalytical Chemistry **381**, 674-680 (2005).

[25] F. Darain, S.U. Park, Y.B. Shim, "Disposable amperometric immunosensor system for rabbit IgG using a conducting polymer modified screen-printed electrode," Biosensors and Bioelectronics **18**, 773-780 (2003).

[26] N. Miura, H. Higobashi, G. Sakai, A. Takeyasu, T. Uda, N. Yamazoe, " Piezoelectric crystal immunosensor for sensitive detection of methamphetamine (stimulant drug) in human urine," Sensors and Actuators B: Chemical **13**, 188-191 (1993).

[27] B. Zhang, Q. Mao, X. Zhang, T. Jiang, M. Chen, F. Yu, W. Fu, " A novel piezoelectric quartz micro-array immunosensor based on self-assembled monolayer for determination of human chorionic gonadotropin," Biosensors and Bioelectronics **19**, 711–720 (2004).

[28] K. Ramanathan, B. Danielsson, “Principles and applications of thermal biosensors,” Biosensors and Bioelectronics **16**, 417–423 (2001).

[29] S. Kumbhat, K. Sharma, R. Gehlot, A. Solanki, V. Joshi, “Surface plasmon resonance based immunosensor for serological diagnosis of dengue virus infection,” Journal of Pharmaceutical and Biomedical Analysis **52**, 255–259 (2010).

[30] J. Wang, “Towards Genoelectronics: Electrochemical Biosensing of DNA Hybridization,” Chemistry - A European Journal **5**, 1681–1685(1999).

[31] I. H. Cho, D. H. Kim, S. Park, “ Electrochemical biosensors: Perspective on functional nanomaterials for on-site analysis,” Biomaterials research **24**, 1-12 (2020).

[32] C. Zhu, G. Yang, H. Li, D. Du, Y. Lin, “Electrochemical sensors and biosensors based on nanomaterials and nanostructures,” Analytical chemistry **87**, 230-249 (2015).

[33] D. Grieshaber, R. MacKenzie, J. Vörös, E. Reimhult, “Electrochemical Biosensors - Sensor Principles and Architectures,” Sensors **8**, 1400–1458, (2008).

[34] E. Dertien, P.P. Regtien, “Sensors for Mechatronics”, Elsevier, (2018).

[35] C. Yao, Y. Qi, Y. Zhao, Y. Xiang, Q. Chen, W. Fu, “Aptamer-based piezoelectric quartz crystal microbalance biosensor array for the quantification of IgE,” Biosensors and Bioelectronics **24**, 2499–2503 (2009).

[36] B. Danielsson, B. Mattiasson, K. Mosbach, “Enzyme thermistor devices and their analytical applications,” Applied Biochemistry and Bioengineering **3**, 97–143 (1981).

[37] B. Mattiasson, C. Borrebaeck, B. Sanfridson, K. Mosbach, “Thermometric enzyme linked immunosorbent assay: TELISA,” Biochimica et Biophysica Acta (BBA)-Enzymology **483**, 221–227 (1977).

[38] E. Kazura, R. Mernaugh, F. Baudenbacher, "A capillary-perfused, Nanocalorimeter platform for thermometric enzyme-linked immunosorbent assay with femtomole sensitivity," Biosensors **10**, 71(2020).

[39] S.N. Sawant, "Development of biosensors from biopolymer composites," Biopolymer composites in electronics, 353-383 (2017).

[40] F. Long, A. Zhu,; H. Shi, "Recent Advances in Optical Biosensors for environmental monitoring and early warning," Sensors **13**, 13928–13948 (2013).

[41] N. J. Mol, M.JE. Fischer, "Surface plasmon resonance: methods and protocols, ", Springer (2010).

[42] P. Damborský, J. Švitel, J. Katrlík, "Optical biosensors," Essays in biochemistry **60**, 91–100 (2016).

[43]N.R. Fong, M. Menotti, E. Lisicka-Skrzek, H. Northfield, A. Olivieri, N. Tait, M. Liscidini, P. Berini, "Bloch long range surface plasmon polaritons on metal stripe waveguides on a multilayer substrate," ACS Photonics **4**, 593-599 (2017).

[44] S.A. Maier, "Plasmonics: Fundamentals and Applications," Springer, 2007.

[45] P. Berini, "Plasmon polariton waves guided by thin lossy metal films of finite width: Bound modes of symmetric structures," Physical Review B **61**, 10484-10503 (2000).

[46] W.E. Vargas, "Optical and electrical properties of hydrided palladium thin films studied by an inversion approach from transmittance measurements," Thin Solid Films **496**, 189 (2006).

[47] A.D. Rakić, "Optical properties of metallic films for vertical-cavity optoelectronic devices," Applied Optics **37**, 5271 (1998).

[48] P. B. Johnson,R.W. Christy, "Optical Constants of the Noble Metals," Physical Review B **6**, 4370 (1972).

[49] V. Giannini,A.I. Fernández-Domínguez, S.C. Heck, S.A. Maier, “Plasmonic nanoantennas: fundamentals and their use in controlling the radiative properties of nanoemitters,” Chemical reviews **111**, 3888-3912 (2011).

[50] A.D. Boardman, B.V. Paranjape, “The optical surface modes of metal spheres,” Journal of Physics F: Metal Physics **7**, 1935–1945 (1977).

[51] F.P. Schmidt, H. Ditlbacher, U. Hohenester, A. Hohenau, F. Hofer, J.R. Krenn, “Universal dispersion of surface plasmons in flat nanostructures,” Nature Communications **5**, 1–6 (2014).

[52] E. T. Arakawa, M.W. Williams, R. N. Hamm, and R. H. Ritchie, “Effect of Damping on Surface Plasmon Dispersion, ” Physical Review Letters **31**, 1127-1129 (1973).

[53] J. Homola. “Electromagnetic Theory of Surface Plasmons,” Springer Series on Chemical Sensors and Biosensors **4**, 3-44 (2006).

[54] B. Yousif, M.E.A. Abo-Elsoud, H. Marouf, “High-performance enhancement of a GaAs photodetector using a plasmonic grating,” Plasmonics **15**, 1377-1387 (2020).

[55] P.R. West, S. Ishii, G.V. Naik, N.K. Emani, V.M. Shalaev, A. Boltasseva, “Searching for better plasmonic materials, ” Laser & Photonics Reviews **4,** 795–808 (2010).

[56] P. Berini, “ Long-range surface plasmon polaritons,” Advances in optics and photonics **1**, 484 -588 (2009).

[57] P. Berini. “Plasmon-polariton waves guided by thin lossy metal films of finite width: Bound modes of asymmetric structures,” Physical Review B **63**, 125417 (2001).

[58] T. W. Ebbesen, C. Genet, S. I. Bozhevolnyi, “Surface plasmon circuitry,” Physics Today **61**, 44 (2008).

[59] T. Minh, K. Tanaka, M. Tanaka, "Complex propagation constants of surface plasmon polariton rectangular waveguide by method of lines," Optics Express **16**, 9378-9390 (2008).

[60] P. Berini, R. Buckley, "On the convergence and accuracy of numerical mode computations of surface plasmon waveguides," Journal of Computational and Theoretical Nanoscience **6**, 2040-2053 (2009).

[61] G. Veronis, S. Kocaba, D. A. B. Miller,S. Fan, "Modeling of Plasmonic Waveguide Components and Networks," Journal of Computational and Theoretical Nanoscience **6**, 1808-1826 (2009).

[62] A. Boltasseva, T. Nikolajsen, K. Leosson, K. Kjaer, M.S. Larsen, S.I. Bozhevolnyi, "Integrated optical components utilizing long-range surface plasmon polaritons," Journal of lightwave technology **23**, 413–422 (2005).

[63] R. Charbonneau, C. Scales, I. Breukelaar, S. Fafard, N. Lahoud, G. Mattiussi, P. Berini, "Passive integrated optics elements based on long-range surface plasmon polaritons," Journal of lightwave technology **24**, 477–494 (2006).

[64] A. Otto, "Excitation of nonradiative surface plasma waves in silver by the method of frustrated total reflection," Zeitschrift für Physik A Hadrons and nuclei **216**, 398–410 (1968).

[65] A. Otto, "Excitation by light of ω+ and ω- surface plasma waves in thin metal layers," Zeitschrift für Physik A Hadrons and nuclei **219**, 227–233 (1969).

[66] E. Kretschmann, "Die Bestimmung optischer Konstanten von Metallen durch Anregung von Oberfl¨achenplasmaschwingungen," Zeitschrift für Physik A Hadrons and nuclei **241**, 313–324 (1971).

[67] NanoOptics [Online]:
https://www.photonics.ethz.ch/fileadmin/user_upload/Courses/NanoOptics/

[68] M. J. E. Fischer, “Surface plasmon resonance” Springer (2010).

[69] S. Löfås, “Optimizing the Hit-to-Lead Process Using SPR Analysis,” Assay and drug development technologies **2**, 407–416 (2004).

[70] V. M. Agranovich,D. L. Mills, “Electromagnetic Waves at Surfaces and Interfaces, ” North-Holland Publishing Company (1982).

[71] J. Dost´alek, A. Kasry, W. Knoll, “Long range surface plasmons for observation of biomolecular binding events at metallic surfaces,” Plasmonics **2**, 97–106 (2007).

[72] A. Degiron, S.Y. Cho, T. Tyler, N. M.Jokerst, D. R. Smith, “Directional coupling between dielectric and long-range plasmon waveguides,” New Journal of Physics **11**, 015002. (2009).

[73] Asahi Glass Company, “Cytop Technical Brochure,” 2009. [Online]. Available: http://www.agc.com.

[74] Dupont, “Teflon AF Properties.” [Online]. Available: www.dupont.com.

[75] P. Berini, “Bulk and surface sensitivities of surface plasmon waveguides,” New journal of physics **10**, 105010, (2008).

[76] O. Krupin, W.R. Wong, P. Beland, F. R. M.Adikan, P. Berini, “Long-Range Surface Plasmon-Polariton Waveguide Biosensors for Disease Detection,” Journal of lightwave technology **34**, 4673−4681(2016).

[77] C. Chen, P. Berini, “Grating couplers for broadside input and output coupling of long-range surface plasmons,” Optics Express **18**, 8006−8018 (2010).

[78] J. Homola, “Surface Plasmon Resonance Based Sensors, ” Springer (2006).

[79] J. Homola, S. S. Yee, and G. Gauglitz, “Surface plasmon resonance sensors: review, ” Sensors and Actuators B-Chemical **54**, 3-15 (1999).

[80] K.V. Sreekanth, S. W. Zeng, K.T. Yong,T. Yu, “Sensitivity enhanced biosensor using graphene-based one-dimensional photonic crystal,” Sensors and Actuators BChemical **182**, 424-428 (2013).

[81] J. Golden, M.D. Yates, M. Halsted, L. Tender, “Application of electrochemical surface plasmon resonance (ESPR) to the study of electroactive microbial biofilms,” Physical Chemistry Chemical Physics **20**, 25648-25656 (2018).

[82] J.F. Rusling, “Biomolecular films: design, function, and applications,” CRC Press (2003).

[83] N. Elgrishi, K.J. Rountree, B.D. McCarthy, E.S. Rountree, T.T. Eisenhart, J.L. Dempsey, “A practical beginner’s guide to cyclic voltammetry”, Journal of chemical education **95**, 197-206 (2018)

[84] S. Wang, X. Huang, X. Shan, K.J. Foley, N. Tao, “Electrochemical surface plasmon resonance: basic formalism and experimental validation”, Analytical chemistry **82**, 935-941 (2010).

[85] J.G. Gordon, S. Ernest, “Surface plasmons as a probe of the electrochemical interface,” Surface science **101**,499-506 (1980).

[86] X. Huang, S. Wang, X. Shan, X. Chang, and N. Tao, “Flow-through electrochemical surface plasmon resonance: detection of intermediate reaction products,” Journal of Electroanalytical Chemistry **649**, 37-41(2010).

[87] S. Patskovsky, A.M. Dallaire, M. Meunier, “Electrochemical surface plasmon resonance sensing with absorptive redox mediator film,” Sensors and Actuators BChemical **222**, 71-77, (2016).

[88] T. Sannomia, H. Dermutz, C. Hafner, J. Voros, A. B. Dahilin, “Electrochemistry on a localized surface plasmon sensor,” Langmuir **26**, 7619-7626, (2010).

[89] I. Ahmed, L. Shi, H. Pasanen, P. Vivo, P. Maity, M. Hatamvand, Y. Zhan. “There is plenty of room at the top: generation of hot charge carriers and their applications in perovskite and other semiconductor-based optoelectronic devices,” Light: Science & Applications **10**,1-28 (2021)

[90] H. Reddy, V.M. Shalaev, “Plasmonic hot-carriers and their applications: opinion,” Optical Materials Express **11** ,3827-3832 (2021).

[91] G. Tagliabue, A.S. Jermyn, R. Sundararaman, A.J. Welch, J.S. DuChene,R. Pala, A.R. Davoyan, P. Narang, H.A. Atwater,”Quantifying the role of surface plasmon excitation and hot carrier transport in plasmonic devices,” Nature communication **9**, 1-8 (2018).

[92] T.P. Rossi, P. Erhart, M. Kuisma, “Hot-carrier generation in plasmonic nanoparticles: the importance of atomic structure,” ACS nano **14**, 9963-9971 (2020).

[93] Y. Zhang, W .Guo, Y. Zhang, W.D. Wei, “Plasmonic Photoelectrochemistry: In View of Hot Carriers,” Advance Materials **33**, 2006654 (2021).

[94] L. Zhou, D. L. Swearer, C. Zhang, H. Robatjazi, H. Zhao, L. Henderson, L.Dong, P.Christopher, E. A. Carter, P. Nordlander, N. J. Halas, “Quantifying hot carrier and thermal contributions in plasmonic photocatalysis,” Science **362**, 69-72 (2018).

[95] P.K. Jain, “Taking the Heat Off of Plasmonic Chemistry,” J. Physical Chemistry C **123**, 24347−24351.

[96] G. Baffou, I. Bordacchini, A. Baldi, “Quidant, R. Simple experimental procedures to distinguish photothermal from hot-carrier processes in plasmonics,” Light: Science & Applications **9**, 1-16 (2020).

[97] E. Cortés, L.V.Besteiro, A. Alabastri, A. Baldi, G. Tagliabue, A. Demetriadou, P. Narang, “Challenges in Plasmonic Catalysis,” ACS Nano **14**, 16202-16219 (2020).

[98] Y. Dubi, I.W. Un, Y. Sivan, “Thermal effects – an alternative mechanism for plasmon-assisted photocatalysis,” Chemical Science **11**, 5017--5027 (2020).

[99] M. Maley, J. W.Hill, P.Saha, J. D.Walmsley, C.M. Hill, “The role of heating in the electrochemical response of plasmonic nanostructures under illumination,” The Journal of Physical Chemistry C **123**, 12390-12399 (2019).

[100] M. Bauer, A. Marienfeld, M. Aeschlimann, “Hot electron lifetimes in metals probed by time-resolved two-photon photoemission,” Progress in Surface Science **90**, 319-376 (2015).